Technical University of Munich
Department of Physics

Master's thesis

Development and Characterization of novel readout electronics for LEGEND

Entwicklung und Charakterisierung neuer Ausleseelektronik für LEGEND

Florian Henkes

26th January 2022

Max Planck Institute for Physics

Erstgutachter (Themensteller): Prof. Dr. S. Mertens
Zweitgutachter: Prof. S. Schönert

Declaration of Authorship

I hereby declare that the thesis submitted is my own unaided work. All direct or indirect sources used are acknowledged as references. I am aware that the thesis in digital form can be examined for the use of unauthorized aid and in order to determine whether the thesis as a whole or parts incorporated in it may be deemed as plagiarism. For the comparison of my work with existing sources I agree that it shall be entered in a database where it shall also remain after examination, to enable comparison with future theses submitted. Further rights of reproduction and usage, however, are not granted here.
This paper was not previously presented to another examination board and has not been published.

Munich, 26th January 2022...
Signature

Acknowledgements

First of all, I would like to thank Prof. Susanne Mertens for the excellent supervisory and the unique opportunity to work in your group. I am very thankful for the excellent support during the thesis. You always had time for all kind of occurring problems and could give me a lot of guidance with helpful suggestions.
Not less important, I would like to thank Michael Willers and Frank Edzards very much. It was one of the best experiences during my study to work with you. Your ideas and support have been highly stimulating and it was a pleasure to have this great kind of support. In particular, a big thanks goes out to Mike who spent more than four weeks in total with me at the Gran Sasso laboratory giving me the chance to get insights into every detail of LEGEND commissioning without forgetting about the great Italian food. You helped me a lot with your great experience in readout electronics to really understand the details. Furthermore, I want to thank Frank for all the help with coding and analysis, the very nice tutorials and answering every question I had whether you had time or not.
I want to thank the whole KATRIN/TRISTAN group for the warm welcome and the great and stimulating environment though the social activities during Covid times had to be reduced.
I also want to thank Rebecca Carney, Alexey Drobizhev and Alan Poon for giving me the opportunity to analyze the ASIC chip in Munich and for a lot of nice meetings with interesting discussions about the chip.
Finally, I must express my profound gratitude to family, particular my parents Susanne and Stefan and my brother Leon for providing me with unfailing support and continuous encouragement throughout my years of study and through the process of writing this thesis. I also want to thank my lovely girlfriend Annette for the enormous support during difficult times and for having an open ear for all my troubles. Thank you very much!
Last but not least, a big thanks goes out to my friends Jan, Lara, Nico, Florian, Chris and Sabrina for the support. Thanks!

Contents

List of Abbreviations

Abstract

The Large Enriched Germanium Experiment for $0\nu\beta\beta$ Decay (LEGEND) is a tonne-scale experimental program to search for neutrinoless double beta ($0\nu\beta\beta$) decay in the isotope ^{76}Ge with high-purity germanium (HPGe) detectors operated in liquid argon (LAr). The experiment aims to reach signal discovery potential at half lifes greater than $T^{0\nu}_{1/2} > 10^{28}$ yr which corresponds to effective neutrino masses of < 20 meV and would fully cover the inverted ordering of neutrinos. The experiment employs a two-staged approach with LEGEND-200 being the first phase located at the Laboratori Nazionali del Gran Sasso (LNGS) with up to 200 kg of ^{76}Ge and LEGEND-1000, the second phase with up to 1000 kg and targeted total exposure of 10 t yr.
One of the major challenges for low-background experiments with HPGe detectors is sensitive and reliable readout electronics which encompasses a compromise between low electronic noise for best energy resolution and low background contribution.
Regarding LEGEND-200, the signal readout electronics has been investigated in two research stays at the LNGS during summer and autumn of 2021. The measurements performed in this thesis demonstrate the functionality of key components such as the CSA and present optimizations of the signal readout chain with respect to signal integrity and pulse shape as well as electronic noise present in the setup. In addition, the first detectors operated in LEGEND-200 have been commissioned and their data analyzed with particular focus on the electronic performance.
For LEGEND-1000, the readout electronic baseline design aims for a newly developed CSA based on CMOS technology. In this thesis, the performance of a new ASIC chip developed by Lawrence Berkeley National Laboratory (LBNL) is investigated. The chip integrates the two stages of current LEGEND CSA designs into a single low-mass chip to achieve excellent noise performance. The ASIC improves a number of open issues from previous ASIC implementations such as reduced number of supply lines, compatibility with higher detector capacities and differential signal ouput. A main result of this thesis is a detailed understanding of the waveform output which shows improper behavior in the decay tail leading to non-linearities in the output performance. A detailed analysis of these output waveforms demonstrates that the decay tail is not suitable for the applications of standard analysis routines used in LEGEND and that changes

in the ASIC design are likely required. To this end, a possible extension of the current chip design is suggested and examined in a proof-of-concept study via simulations where the results show that a second stage in the circuit can potentially remove the non-linearities resulting in clean and reliable output waveforms.

Chapter 1

Introduction

One of the fundamental open questions of modern physics is understanding the baryon asymmetry in the early universe, the origin of our matter-dominated universe, which we live in today. A tiny imbalance favored matter over anti-matter at some point in time close to the big bang enabling the possibility of clustering and star formation. A necessary criterion for baryon asymmetry is lepton number violation in a rare process. The neutrinoless double beta ($0\nu\beta\beta$) decay is one of these proposed processes, and its discovery would violate the lepton number by two units. Neutrinos are the only particle in the Standard Model (SM) of particle physics which could be their own antiparticle, a so-called Majorana particle which is a property connected to the origin of its mass. Neutrinos have been at the forefront of discovery in particle physics for a long time, and the study of their properties was a primary driver for the conception of the weak interaction and modern quantum field theories. Since the discovery of the neutrino in 1956, our understanding of neutrinos has constantly increased, resulting in the more recent observations of neutrino oscillations which state that the neutrinos have mass [1–5].
The $0\nu\beta\beta$ decay is the only way to search for a lepton number violation process in the laboratory and therefore to determine if the neutrino is a Majorana particle or not, together with information on the absolute mass scale of the neutrino. In general, every element which can perform a double beta ($2\nu\beta\beta$) decay could also perform a $0\nu\beta\beta$ decay in which two neutrons in a nucleus convert into two protons and two electrons without the emission of neutrinos. Moreover, the process can shed light on the mass ordering of neutrinos, namely the normal or inverted ordering. In principle, the $0\nu\beta\beta$ decay can happen in several isotopes, including ^{76}Ge for which it is possible to build large high-purity germanium (HPGe) detector arrays. In recent years, two major experiments could set new limits on the half-life $T^{0\nu}_{1/2}$ for $0\nu\beta\beta$ decay in ^{76}Ge which is the parameter of interest:
The GERmanium Detector Array (GERDA) experiment was a ^{76}Ge based $0\nu\beta\beta$ low-background experiment using HPGe detectors located at the LNGS where

the Gran Sasso massif of 3500 m water equivalent (m.w.e.) reduced hadronic particles of cosmic ray showers and the muon flux at the experiment site by about six orders of magnitude to $\Phi_\mu \approx 1.25\,\text{muons}\,\text{m}^{-2}\,\text{h}^{-1}$ [6–9]. The bare HPGe detectors were operated in LAr in a $64\,\text{m}^3$ large cryostat surrounded by a water vessel containing photo-multiplier tubes (PMT) as muon veto. The scintillation light arising from the LAr was measured by a veto system to reject background events [9]. The final result after Phase II claimed a lower limit on the half-life of $T^{0\nu}_{1/2} > 1.8 \times 10^{26}\,\text{yr}$ (90% CL) and a upper limit on the effective neutrino mass of $\langle m_{\beta\beta}\rangle < 79 - 180\,\text{meV}$ for a total exposure of 127.2 t yr at a background index of $\text{BI} = 5.2^{+1.6}_{-1.3}\text{cts}\,\text{keV}^{-1}\,\text{kg}^{-1}\,\text{yr}^{-1}$ being the best background index achieved so far among all $0\nu\beta\beta$ decay experiments [10].
The Majorana Demonstrator (MJD) experiment was a US-based experiment located at Sanford Underground Research Facility (SURF) in Lead, South Dakota. It hosted the HPGe detectors in a vacuum cryostat surrounded by a multi-layer shielding structure to reduce backgrounds. The latest result claimed a lower limit on the half-life of $T^{0\nu}_{1/2} > 2.7 \times 10^{25}\,\text{yr}$ (90% CL) and a upper limit on the effective neutrino mass of $\langle m_{\beta\beta}\rangle < 200 - 433\,\text{meV}$ for a total exposure of 21.3 t yr at a background index of $\text{BI} = (4.7 \pm 0.8) \times 10^{-3}\,\text{cts}\,\text{keV}^{-1}\,\text{kg}^{-1}\,\text{yr}^{-1}$ [11]. The MJD experiment could achieve a final energy resolution of $(2.53 \pm 0.08)\,\text{keV}$ FWHM being the best energy resolution among all $0\nu\beta\beta$ decay experiments [11].
The Large Enriched Germanium Experiment for $0\nu\beta\beta$ Decay (LEGEND) combines the best out of MJD and GERDA in a new tonne-scale experiment targeting a half-life greater than $T^{0\nu}_{1/2} > 10^{28}\,\text{yr}$ which would scan the hole inverted ordering of the neutrinos. LEGEND consists of two phases: LEGEND-200 is currently built at the LNGS laboratory using HPGe detectors with total mass up to 200 kg while LEGEND-1000 will use up to 1000 kg of ^{76}Ge to target a total exposure of 10 t yr. This thesis contains several contributions to the characterization and testing of readout electronics in LEGEND-200 based on two research stays at LNGS during July and October 2021, as well as to the development of novel readout electronics based on ASIC technology performed at Technical University of Munich (TUM) and LBNL.
Apart from this introduction, it is structured into four parts:

1. Chapter 2 gives a general overview about neutrino physics in Section 2.1 followed by a detailed discussion of the properties of $0\nu\beta\beta$ decay in Section 2.2. Afterwards, Section 2.3 explains the details of semiconductor detector physics before Section 2.4 summarizes the detailed properties and functionalities of LEGEND itself.

2. Chapter 3 elaborates the characterization measurements for LEGEND-200 performed during two research stays at LNGS in summer and autumn

2021. After a general introduction to signal readout electronics in Section 3.1, the properties of electronic noise in such circuits is discussed in Section 3.2. Following, the signal readout architecture in LEGEND-200 is presented and main components are explained in Section 3.3. Section 3.4 then describes the detailed results of the integration tests and the commissioning of the electronics at LNGS.

3. Chapter 4 presents the development and characterization of a novel ASIC based CSA recently developed by LBNL. Section 4.1 gives an introduction to the signal readout electronics for LEGEND-1000 and their goals. Following, Section 4.2 presents the main results of the characterization measurements of the chip. Since the unique properties of the output signals of the chip can cause problems in the LEGEND analysis routines, Section 4.3 presents a possible solution for an extension of the layout by a second stage circuit on chip by a proof-of-concept study to encompass signal integrity.

4. Chapter 5 closes the thesis with a conclusion and a outlook to the obtained results.

In addition, a bibliography of all cited references ordered after their time of appearance is shown in the Appendix 5 together with additional figures in Appendix B.

Chapter 2

Preface

The following chapter will give an overview of the current understanding of neutrino physics together with the specialties of $0\nu\beta\beta$ decay followed by the detailed presentation of LEGEND.

2.1 Neutrinos in the Standard Model (SM) of particle physics

At present knowledge, we know about four fundamental forces in the universe: the electromagnetic, the weak and the strong force, and the gravitation. While gravitation is described by the General Theory of Relativity (GT), the others are described by the Standard Model (SM) of particle physics. It consists of a relativistic quantum field theory in which interactions take place by local gauge symmetries and is realized by the three gauge symmetry groups $U(1)_Y \times SU(2)_L \times SU(3)_C$. Here, matter consists of spin-$\frac{1}{2}$ particles, so-called fermions, and spin-1 particles, so-called (gauge) bosons which are the force mediators. A detailed listing of the SM can be found in Figure 2.1. Looking at fermions, one can distinguish between strongly interacting quarks and leptons that cannot take part in the strong interaction. To this day, there are six known quarks and six known leptons, which can be divided into three generations as shown in Figure 2.1. The SM like every quantum field theory, is typically described by a Lagrangian density $\mathcal{L}(\psi, \partial\psi)$ which connects to the equations of motion for fields ψ:

$$-\partial_\mu \left(\frac{\partial \mathcal{L}}{\partial(\partial_\mu \psi)} \right) + \frac{\partial \mathcal{L}}{\partial \psi} = 0 \tag{2.1}$$

Since the SM does not determine coupling constants, mixing angle, and particle masses, the SM contains 19 free parameters to be determined experimentally: six quark masses, three lepton masses, three gauge coupling constants, the Higgs boson mass and self-coupling strength, the four parameters of the CKM

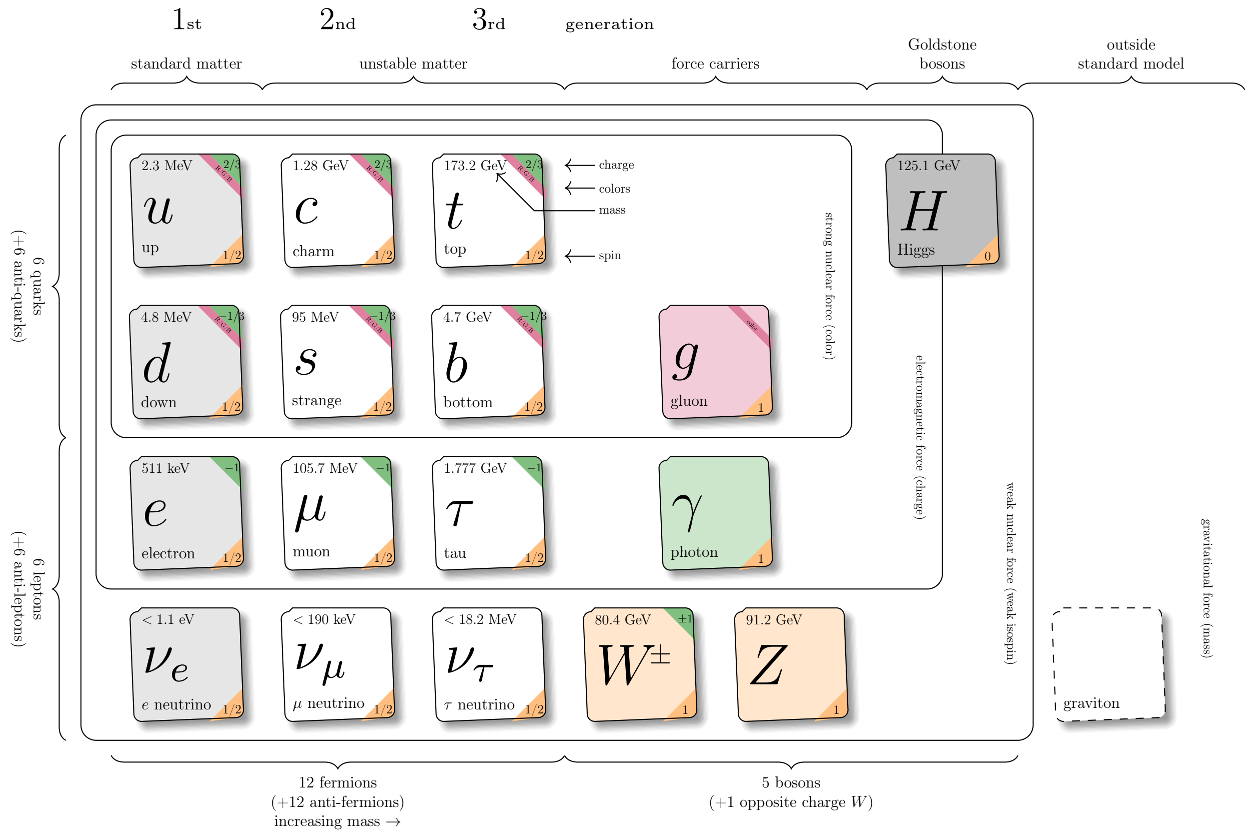

Figure 2.1: Particle zoo of the Standard Model (SM) of particle physics. The masses are taken from [12]. Since photons (γ) and gluons are massless in the SM and only upper limits exists for their masses, they are not included in the figure. The current limits on the three neutrinos masses are shown despite they are massless in the SM.

matrix and one CP-violating parameter for the strong interaction.

In the following, the discussion will focus on neutrinos and the weak interaction of neutrinos. In the SM, neutrinos are massless, neutral leptons and can only participate in the weak interaction, which is mediated by two massive gauge bosons: $W^{\pm}$ and Z^0. In 1930, the existence of the neutrino was first postulated by Wolfgang Pauli for observations in the β^--decay: A neutron decays weakly into proton, electron and electron anti-neutrino ($n \to p + e^- + \overline{\nu}_e$). Though the initially assumed two-body decay of the neutron into a proton and an electron only would result in a monochromatic spectrum, a continuous spectrum was observed. Pauli could explain this by introducing a new particle, the neutrino, which was finally experimentally discovered in 1956 by C. L. Cowan Jr. and F. Reines.

The weak interaction is maximally parity-violating (c.f. Wu et al. [13]). Parity is a symmetry transformation that equals a point reflection of the spatial coordinate $\boldsymbol{x}$: $(t, \boldsymbol{x}) \leftrightarrow (t, -\boldsymbol{x})$. If parity would be conserved, any process and its mirrored version would occur with the same probability. Therefore, only left-handed particles and right-handed anti-particles couple to $W^{\pm}$. A left-handed particle is a particle where the direction of the spin is opposite to the direction of motion (and vice versa for right-handed particles). This concept called *helicity* is not Lorentz-invariant (for massive particles), since it is always possible to find a reference frame faster than the particle where the particle seems to move in the opposite direction, but the spin is untouched and following *helicity* is changed. This enforces that each massive left-handed particle contains a right-handed component which scales with the ratio of the particle's mass over its energy.

In the SM, each generation contains one neutrino associated with one charged lepton, namely: the electron neutrino ν_e, the muon neutrino ν_μ and the tau neutrino ν_τ. A quantum number called *weak isospin* T is related to the weak interaction which divides the leptons into left-handed doublets with $T = \frac{1}{2}$ and right-handed singlets with $T = 0$:

$$\begin{pmatrix} \nu_e \\ e^- \end{pmatrix}_L \quad \begin{pmatrix} \nu_\mu \\ \mu^- \end{pmatrix}_L \quad \begin{pmatrix} \nu_\tau \\ \tau^- \end{pmatrix}_L \quad \begin{matrix} \text{with } T_3 = +\frac{1}{2} \\ \text{with } T_3 = -\frac{1}{2} \end{matrix}$$

$$\left(e^-\right)_R \quad \left(\mu^-\right)_R \quad \left(\tau^-\right)_R \quad \text{with } T_3 = 0$$

In this context, left-handed describes a *chirality* state, a Lorentz invariant concept which is the same as the *helicity* in the massless case.
The SM Lagrangian density for a neutrino $\mathcal{L}_\nu(\psi, \partial\psi)$ can be written as follows:

$$\mathcal{L}_\nu = \sum_{\alpha=e,\mu,\tau} \left[\overline{\nu}_{\alpha,L} i\partial\!\!\!/ \nu_{\alpha,L} + \frac{g}{\sqrt{2}} (W_\mu^+ \overline{\nu}_{\alpha,L} \gamma^\mu \ell_{\alpha,L} + \text{h.c.}) + \frac{g}{2\cos\theta_\omega} Z_\mu \overline{\nu}_{\alpha,L} \gamma^\mu \nu_{\alpha,L} \right] \tag{2.2}$$

The first term in Equation 2.2 can be interpreted as the kinetic term. The second term is responsible for the weak charge current and the third term for the neutral current. This two interaction processes can be described by the two exemplary Feynman diagrams in Figure 2.2. The Figure 2.2a referring to the charged current can be interpreted as follows: ℓ annihilates a charged

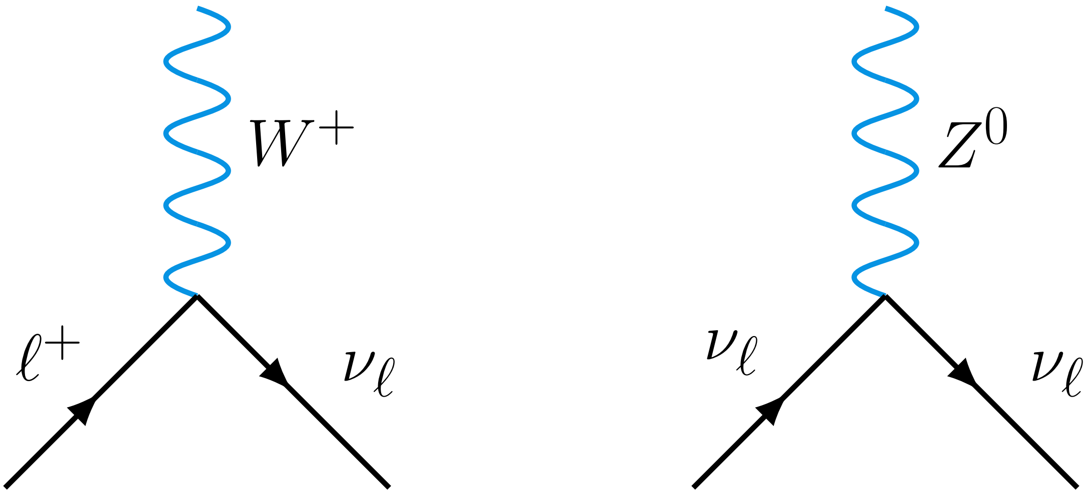

a) Weak charge current **b)** Weak neutral current

Figure 2.2: Feynman diagrams of the neutrino interaction vertices for the charged and neutral current.

lepton $\alpha (= e, \mu, \tau)$ or creates an anti-lepton while $\overline{\nu}$ creates a neutrino or annihilates an anti-neutrino. Therefore, looking back at Equation 2.2, the term $\overline{\nu}_{\alpha,L}\gamma^{\mu}\ell_{\alpha,L}$ couples left-handed leptons to left-handed neutrinos with a coupling strength of $\frac{g}{\sqrt{2}}$ at the vertex. The analogon can be seen in Figure 2.2b where the term $Z_{\mu}\overline{\nu}_{\alpha,L}\gamma^{\mu}\nu_{\alpha,L}$ symbolises a Z^0 boson coupling to a neutrino and a anti-neutrino with a coupling strength of $\frac{g}{2\cos\theta_{\omega}}$ with θ_{ω} the Weinberg angle. If massive neutrinos exist, a mass term has to be included in the Lagrangian. However, because neutrinos in the SM only appear with negative helicity, neutrino mass generation via Yukawa coupling is not allowed. For other leptons, mass generation is performed by the spontaneous symmetry breaking of the left-handed doublet with the right-handed singlet. Since there are no right-handed neutrinos in the SM, there exists no gauge invariant (renormalizable) operator for neutrino mass generation at tree level.

As mentioned, neutrinos are produced in nuclear processes via the weak interaction. In nature, different types of neutrino sources exist: on the one hand, there are the so-called natural neutrinos which are mainly originating from astrophysical sources such as the fusion processes in the sun, supernovae, and gamma-ray bursts or from the so-called cosmic neutrino background, a relic neutrino background from the early universe. Furthermore, radioactive isotopes in the earth produce β-decay neutrinos (geo-neutrinos), and cosmic

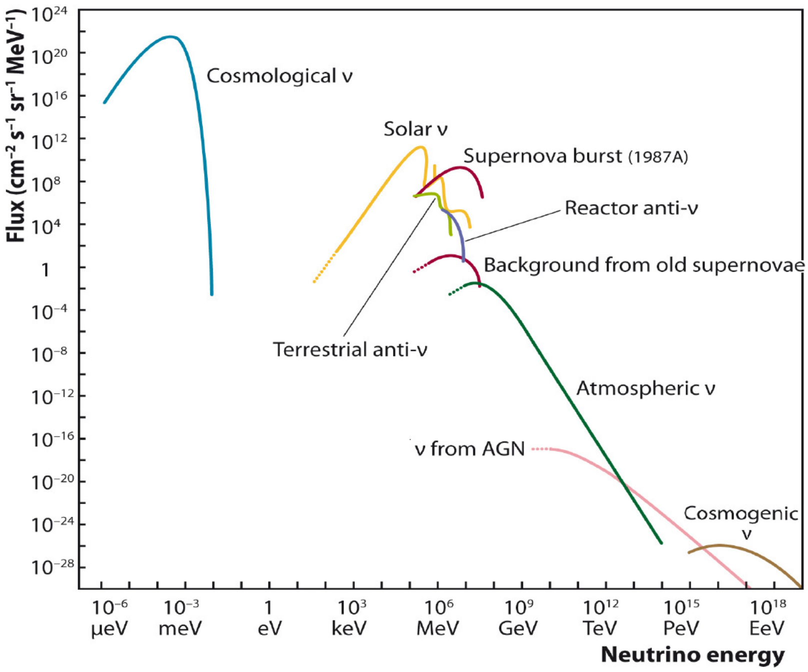

Figure 2.3: Measured and expected fluxes of natural and artificial neutrinos with their corresponding energy range. Figure taken from [14].

ray interaction in the upper atmosphere leads to atmospheric neutrinos. On the other hand, there are artificial neutrinos which are mainly consisting of anti-neutrinos in nuclear fission processes in artificial reactors as well as intense neutrino beams produced from accelerators. An overview of the different types of neutrino sources and their corresponding flux is illustrated in Figure 2.3.

For many years, physicists assumed that neutrinos were massless fundamental particles and fully described by the lagrangian from Equation 2.2. The picture changed fundamentally after the discovery of *neutrino oscillations*. As already mentioned, nuclear fusion processes in the sun produce a large flux of solar neutrinos in a accessible energy range for earth detectors. Hereby, the net reaction of the process is $4p \rightarrow^4 \mathrm{He} + 2e^+ + 2\nu_e$ (so-called *pp*-chain). In a first experiment from R. Davis et al. [15, 16], the neutrinos were detected by the Inverse Beta Decay (IBD) of $^{37}\mathrm{Cl}$ via

$$^{37}\mathrm{Cl} + \nu_e \rightarrow^{37} \mathrm{Ar} + e^- \tag{2.3}$$

and the subsequent counting of $^{37}\mathrm{Ar}$ after extracting via β-decay

$$^{37}\mathrm{Ar} \rightarrow^{37} \mathrm{Cl} + e^- + \overline{\nu}_e \ . \tag{2.4}$$

However, the results showed that the measured flux was only a third of the expectation from the Standard Solar Model (SSM)[1] [17, 18]. This flux deficit became known as the Solar Neutrino Problem (SNP) and was independently confirmed by the experiments `GALLEX` (1991 -1996) [19], `GNO` (1998-2002) [20], `SAGE` (1990 - 2006) [21, 22] and `Borexino` (2007 - 2021) [23–25].

A possible solution to the Solar Neutrino Problem (SNP) was already suggested for the Homestake experiment by Pontecorvo in 1953 [26], the so-called neutrino oscillations in analogy to the transitions in the $\mathrm{K}^0/\overline{\mathrm{K}}^0$ system in the quarks sector. The oscillations state that the ν_e coming from the sun on their way to the earth are converted into the two other neutrino species ν_μ and ν_τ which can explain the flux deficit because the detectors were only sensitive to electron neutrinos.[2]
Finally, the SNP was solved by the Sudbury Neutrino Observatory (SNO) which was sensitive to all three neutrino flavors via charged and neutral current as well as elastic scattering. Thus, the total neutrino flux could be measured as well as the ν_e flux which showed excellently agreement with the SNP and strong evidence for neutrino oscillation since ν_μ and ν_τ cannot be produced in the sun so that the missing ν_e have to be converted into ν_μ/ν_τ, which the data clearly showed.
In addition, neutrino oscillation could also be shown for atmospheric neutrinos. While cosmic rays (mainly protons) are colliding with nuclei in the upper atmosphere, they produce hadronic showers containing charged pions $\pi^\pm$, and Kaon $\mathrm{K}^\pm$. In subsequent processes, atmospheric neutrinos are produced via

$$\pi^{+/-} \text{ or } \mathrm{K}^{+/-} \rightarrow \mu^{+/-} + \nu_\mu/\overline{\nu}_\mu \tag{2.5}$$
$$\mu^{+/-} \rightarrow e^{+/-} + \nu_e/\overline{\nu}_e + \overline{\nu}_\mu/\nu_\mu \tag{2.6}$$

From this simple equation, one can expect a ratio of $N_{\nu_\mu} : N_{\nu_e} = 2 : 1$. Super-Kamiokande, a Japanese underground experiment using a water-Cerenkov detector with 50 kt ultra-pure water in a large underground tank combined with 11200 PMT to detect Cerenkov light, measured the ratio to $(N_{\nu_\mu} : N_{\nu_e})_{\text{observed}} = (1.26 \pm 0.12) : 1$. Despite the lack of ν_μ with respect to ν_e, the single electron neutrino flux was in aggreement with excpectations: Superkamiokande measured a deficit in the muon neutrino flux. This could be explained by the flavour transition by neutrino oscillation from $\nu_\mu \rightarrow \nu_\tau$ on their way to the detector which was not sensitive to tau neutrinos. [27]
Neutrino oscillation occur because the neutrino flavor eigenstates $|\nu_l\rangle$ $(l = e, \mu, \tau)$ are not concurrent to the neutrino mass eigenstates $|\nu_i\rangle$ $(i = 1, 2, 3)$, but

[1] The measured flux was mainly from ^{8}B from the *pp*-cycle.
[2] Weak interactions mediated by charged currents are only possible for ν_e

connected by

$$|\nu_\alpha\rangle = \sum_{i=1}^{3} \mathcal{U}^*_{\alpha i} |\nu_i\rangle \tag{2.7}$$

where $\mathcal{U}^*_{ll}$ denotes a complex 3×3 matrix, the so-called Pontecorvo-Maki-Nakagawa-Sakata (PNMS) matrix.[3] The PNMS matrix can be parametrized by three different mixing angles (θ_{12}, θ_{13}, θ_{23}) and by one or three complex CP-violating phases (δ, α, β)[4] [28]:

$$\begin{aligned}\mathcal{U} = &\begin{pmatrix}1 & 0 & 0\\ 0 & \cos\theta_{23} & \sin\theta_{23}\\ 0 & -\sin\theta_{23} & \cos\theta_{23}\end{pmatrix} \cdot \begin{pmatrix} cos\theta_{13} & 0 & \sin\theta_{13}e^{-i\delta}\\ 0 & 1 & 0\\ -\sin\theta_{13}e^{i\delta} & 0 & \cos\theta_{13}\end{pmatrix}\\ &\cdot \begin{pmatrix}\cos\theta_{12} & \sin\theta_{12} & 0\\ -\sin\theta_{12} & \cos\theta_{12} & 0\\ 0 & 0 & 1\end{pmatrix} \cdot \mathrm{diag}(1, e^{i\alpha}, e^{i\beta})\end{aligned} \tag{2.8}$$

Following this, the probability to find $|\nu_\beta\rangle = \sum_{i=1}^{3} \mathcal{U}^*_{\beta i} |\nu_i\rangle$ can be expressed as [29]

$$\begin{aligned}\mathcal{P}(\nu_\alpha \to \nu_\beta) &= \langle \nu_\beta | \, \nu(t)\rangle^2\\ &= \left|\sum_i \mathcal{U}^*_{\beta i}\mathcal{U}_{\alpha i} e^{-E_i t}\right|^2\end{aligned} \tag{2.9}$$

$$= \delta_{\alpha\beta} - 4 \cdot \sum_{j>i} ReJ^{ij}_{\alpha\beta} \sin^2\frac{\Delta_{ij}}{2} + 2 \cdot \sum_{j>i} ImJ^{ij}_{\alpha\beta} \sin\Delta_{ij} \tag{2.10}$$

$$\text{with } |\nu(t)\rangle = \sum_j \mathcal{U}^*_{\alpha j} e^{-iE_j t} |\nu_j\rangle \text{ and } J^{ij}_{\alpha\beta} = \mathcal{U}_{\beta i}\mathcal{U}^*_{\alpha i}\mathcal{U}^*_{\beta j}\mathcal{U}_{\alpha j}$$

where the phase can be approximated as $\frac{1}{2}\Delta_{ij} \approx 1.27\left(\frac{\Delta m^2_{ij}}{\mathrm{eV}^2}\right)\left(\frac{L}{\mathrm{km}}\right)\left(\frac{\mathrm{GeV}}{E}\right)$ with E the neutrino energy, L the distance between source and detector and $\Delta m^2_{ij} = m^2_j - m^2_i$ the mass-squared difference of mass eigenstates i and j.

Because Equation 2.9 leads to the fact that the three neutrino mass eigenstates must be non-degenerate to allow neutrino oscillation, at least two out of the

[3] It can be seen as analogue to the Cabibbo-Kobayashi-Maskawa (CKM) matrix in the quark sector.

[4] Here, the existence of only three neutrino mass eigenstates as well as unitarity of the PNMS matrix is assumed.

three neutrinos have to be massive. This is a clear hint of physics Beyond Standard Model (BSM) with up to 9 (7) new parameters to be determined by experiments for Majorana (Dirac) neutrinos: 3 mixing angles, 3 neutrino masses and 3 (1) complex CP-violating phase.[5] Because under experimental conditions $\Delta m^2_{21} \ll |\Delta m^2_{31}| \simeq \Delta m^2_{32}$ holds, Equation 2.9 can be simplified to an oscillation of only two neutrino flavors:

$$\mathcal{P}(\nu_\alpha \to \nu_\beta) = \sin^2(2\theta) \sin^2 \left(1.27 \left(\frac{\Delta m^2_{ij}}{\mathrm{eV}^2} \right) \left(\frac{L}{\mathrm{km}} \right) \right) \tag{2.11}$$

Because atmospheric neutrinos predominantly oscillate by the transformation of muon neutrinos into tau neutrinos, the mixing angle θ_{atm} is associated with θ_{23} so that $\Delta m^2_{atm} = \Delta m^2_{23}$[6] Using the similar approximation for solar neutrinos, the mixing angle $\theta_\odot$ is associated with θ_{12} so that $\Delta m^2_\odot = \Delta m^2_{12}$. Since neutrinos interact with matter, but only electron neutrinos via charged current, the coherent forward scattering changes the oscillation in matter with respect to the vacuum, an effect which can lead to a total conversion of ν_e into ν_μ/ν_τ in the sun, the so-called Mikheyev-Smirnov-Wolfenstein (MSW) effect. Because the MSW effect depends on the sign of Δm^2_{12}, solar neutrino data for $\Delta m^2_\odot$ determines the sign to be positive. Because current neutrino experiments are not sensitive to Δm^2_{31}, the open sign of Δm^2_{31} leaves two possibilities[7]:

1. **NO** (c.f. Figure 2.4 left plot):
   - m_1 is the mass of the lightest mass eigenstate.
   - $m_1 < m_2 < m_3$, $\Delta m^2_{31} > 0$
   - $m_2 = \sqrt{m_1^2 + \Delta m^2_{21}}$, $m_3 = \sqrt{m_1^2 + \Delta m^2_{31}}$
2. **IO** (c.f. Figure 2.4 right plot):
   - m_3 is the mass of the lightest mass eigenstate.
   - $m_3 < m_1 < m_1$, $\Delta m^2_{31} < 0$
   - $m_1 = \sqrt{m_3^2 + \Delta m^2_{23} - \Delta m^2_{21}}$, $m_2 = \sqrt{m_3^2 + \Delta m^2_{23}}$

As already mentioned, neutrinos are considered massless in the SM and no mass-term occurs in the lagrangian (c.f. Equation 2.2). Because of the neutrino

[5] Only looking at the oscialltions, the two additional CP-violating phases α and β have no influence on the oscillation probability because they cancel out, but can influence in lepton number violating processes (c.f below).

[6] It can be described by a two flavor oscillation plus θ_{13} is small and $\frac{\Delta m^2_{12} L}{E} \ll 1$

[7] According to the latest global fits, the normal mass ordering (NO) regime is slightly favored over the inverted mass ordering (IO) regime. [30, 31]

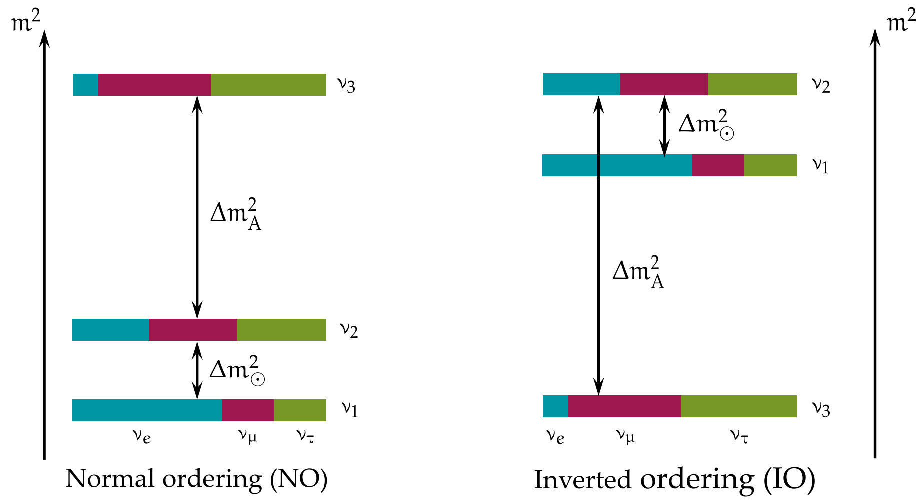

Figure 2.4: The two possible orderings for neutrinos: normal mass ordering (NO) and inverted mass ordering (IO). The neutrino mass eigenstates are a superposition of the flavor eigenstates, and vice versa. Figure from [32]

oscillations, a mass term has to be added to the lagrangian which is generally a *Dirac* mass term

$$\mathcal{L}_D^{\text{mass}} = m_D \overline{\nu}\nu = m_D(\overline{\nu}_L \nu_R + \overline{\nu}_R \nu_L) \tag{2.12}$$

This *Dirac* mass term extends the SM by a new right-handed neutrino ν_R to couple the left-handed fermion field with the right-handed one and allows mass generation via the Higgs mechanism.[8] However, this mechanism does not explain the smallness of neutrino masses and requires special fine-tuning because the scale of the corresponding Yukawa coupling is unnaturally small compared to the ones for other particles. [33]
An alternative is a *Majorana* mass term: Instead of introducing a new particle, it is required that $\nu_R = (\nu_L)^C$ with C the charge conjugation so that the neutrino becomes its one anti-particle, a so-called Majorana particle. This Majorana mass-term can be written as

$$\mathcal{L}_{M,L}^{\text{mass}} = \frac{1}{2} m_{M,L} \left((\overline{\nu}_L)^C \nu_L + \overline{\nu}_L (\nu_L)^C \right) + \text{ h.c.} \tag{2.13}$$

However, a Majorana term in the SM can only exist for truly neutral particles because in terms like $m_{M,L}(\overline{\nu}_L)^C \nu_L$, ν_L annihilates a neutrino with $Y_W = -1$

[8]The new right-handed neutrino has no gauge interactions at all.

whereas $(\overline{\nu}_L)^C$ creates a neutrino with $Y_W = +1$ so that hypercharge is not conserved and the interaction is not gauge invariant under $U_Y(1)$. If again a right-chiral neutrino singlet is introduced, also mass terms such as

$$\mathcal{L}_{M,R}^{\text{mass}} = \frac{1}{2} m_{M,R} \left((\overline{\nu}_R)^C \nu_R + \overline{\nu}_R (\nu_R)^C \right) + \text{ h.c.} \tag{2.14}$$

are allowed without any constraints on $m_{M,R}$ because no interaction with the Higgs field is required.
The two mass terms can combined in the most general form to

$$\mathcal{L}^{\text{mass}} = \frac{1}{2} \begin{pmatrix} \overline{\nu}_L & (\overline{\nu}_R)^C \end{pmatrix} \underbrace{\begin{pmatrix} m_{M,L} & m_D \\ m_D & m_{M,R} \end{pmatrix}}_{\mathcal{M}} \begin{pmatrix} (\nu_L)^C \\ \nu_R \end{pmatrix} + \text{ h.c.} \tag{2.15}$$

which leads under the assumptions of $m_{M,L} = 0$, $m_D \ll m_{M,R}$ to eigenvalues of the matrix $\mathcal{M}$:

$$m_1 = \frac{m_D^2}{m_{M,R}} \tag{2.16}$$

$$m_2 = m_{M,R} \left(1 + \frac{m_D^2}{m_{M,R}^2} \right) \approx m_{M,R} \tag{2.17}$$

This mechanism is called the `Seesaw type I` mechanism[9] and provides with its light m_1 eigenstate and its heavy m_2 eigenstate a natural way of small neutrino mass while the Yukawa coupling stays compatible to the ones of other particles [35–38].

[9]More Seesaw mechanisms for mass generation exist, but are not discussed here. [34]

2.2 Double Beta Decay

Because the only possible access in the laboratory to the properties of neutrinos, whether neutrinos are Majorana particles or not is the $0\nu\beta\beta$ decay, the following section gives an overview about the characteristics of $0\nu\beta\beta$ decay and its connection to neutrinos.
The Weizäcker mass formula describes the mass of nuclei with the same mass number A and different nuclear charge Z [39]:

$$m(A,Z) = \alpha \cdot A - \beta \cdot Z + \gamma \cdot Z^2 + \frac{\delta}{\sqrt{A}} \text{ with } \alpha, \beta, \gamma \text{ const} \tag{2.18}$$

$$\tag{2.19}$$

where δ represents the pairing energy:

$$\delta = \begin{cases} -11.2\,\mathrm{MeV}/c^2 & \text{if } Z \text{ and } \quad N = A - Z \text{ even} \\ 0 & \text{if } A \text{ odd} \\ +11.2\,\mathrm{MeV}/c^2 & \text{if } Z \text{ and } \quad N = A - Z \text{ odd} \end{cases} \tag{2.20}$$

Figure 2.5 shows the isobars with mass number $A = 76$ as example for the Equation 2.18 of the Weizsäcker mass formula. In a typical process, the isotopes can convert into more stable ones by single β^--decay. However, looking at certain isotopes like ^{76}Ge, the single $beta^-$-decay is energetically forbidden if $m(A,Z) < m(A,Z+1)$ so that the only allowed SM mode is the so-called two neutrino double β^- decay ($2\nu\beta\beta$) [10]:

$$(A,Z) \rightarrow (A,Z+2) \qquad +2e^- + 2\overline{\nu}_e \tag{2.21}$$

$$2n \rightarrow 2p \qquad +2e^- + 2\overline{\nu}_e \tag{2.22}$$

Figure 2.6a shows the Feynman diagram of the $2\nu\beta\beta$ decay which was first proposed in 1935 by M. Groeppert Mayer [40]. Among the isotopes in the Periodic Table of the Elements (PTE), there exist 35 candidate isotopes where 10 isotopes have been measured so far with half-lives between $10^{18}\mathrm{yr} < T^{2\nu}_{1/2} < 10^{24}\mathrm{yr}$ [41]. The half-life of $2\nu\beta\beta$ decay can be calculated by [42]:

$$T^{2\nu}_{1/2} = (G^{2\nu} \cdot g_A^4 \cdot |m_e \cdot M^{2\nu}|)^{-1} \tag{2.23}$$

with $G^{2\nu}$ the phase space factor, g_A the axial vector coupling and $M^{2\nu}$ the nuclear matrix element (NME). It should be mentioned here that the axial vector coupling g_A is considered to be an effective constant (quenching) due to

[10] The decay also occurs if the single β^- decay is highly suppressed e.g. by a large angular momentum difference between mother and daughter nuclei.

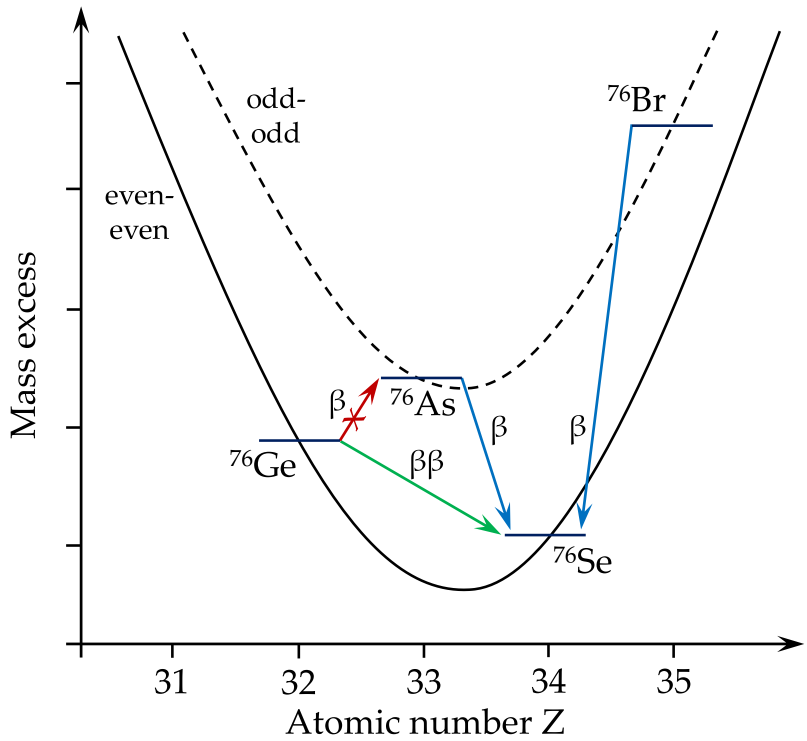

Figure 2.5: Mass parabolas for even-even and odd-odd nuclei using the example of isobars with mass number $A = 76$. Isobars with even mass and atomic number lie on a lower parabola (straight line) compared to those with odd atomic number (dotted line). Typically, transitions between the curves are realized via single beta decay. In some cases, however, the neighboring isobar is energetically higher and single beta decay is forbidden, e.g. $^{76}\text{Ge} \nrightarrow {}^{76}\text{As}$. Then, two-neutrino double beta decay is the only allowed decay mode. Figure from [32].

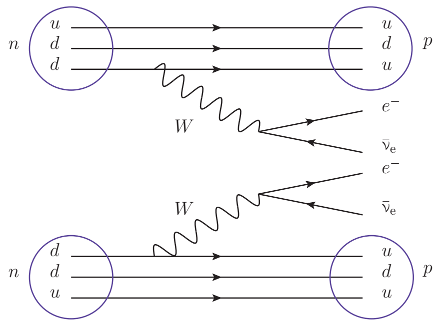

a) Two-neutrino double beta decay ($2\nu\beta\beta$ decay)

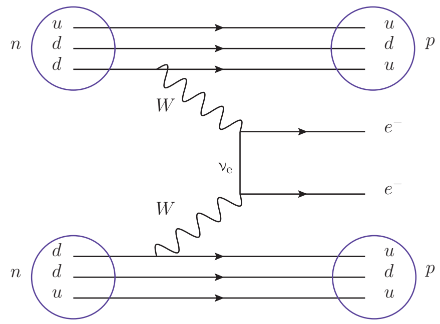

b) Neutrinoless double beta decay ($0\nu\beta\beta$ decay)

Figure 2.6: Feynman diagrams of $2\nu\beta\beta$ decay 2.6a and $0\nu\beta\beta$ decay 2.6b under the assumption of light neutrino exchange.

limitations in the underlying model which was introduced due to systematical differences between modelled and measured half-lifes [43]. However, novel ab-initio calculations seem to model these effects in the NME already for single beta decay calculations [44] and expect to model these also for double beta decay.

Since the energy of the process is shared between the two electrons and the two electron antineutrinos in the final state, the sum of the energy of the two electrons is a continuum from 0 keV to the $Q_{\beta\beta}$-value of the decay like seen for the decay of ^{76}Ge in Figure 2.7. The energy spectrum is empirically modelled in the Primakoff-Rosen approximation for the non-relativistic Coulomb correction by [45, 46]:

$$\frac{\mathrm{d}N}{\mathrm{d}E} \approx E \cdot (Q_{\beta\beta} - E)^5 \cdot (E^4 + 10 \cdot E^3 + 40 \cdot E^2 + 60 \cdot E + 30) \tag{2.24}$$

Since two leptons with $L = +2$ and two antileptons with $L = -2$ are emitted, lepton number is conserved with $\Delta L = 0$.

In contrast, the $0\nu\beta\beta$-decay is a hypothetical predicted new decay mode which is lepton number violating with $\Delta L = +2$ and was already predicted in 1938 by Furry [47]. In the $0\nu\beta\beta$, two neutrons from the parent nucleus are converted into two protons and two electrons in the daughter nucleus without the emission of electron anti-neutrinos:

$$(A, Z) \rightarrow (A, Z + 2) \qquad +2e^- \tag{2.25}$$

$$2n \rightarrow 2p \qquad +2e^- \tag{2.26}$$

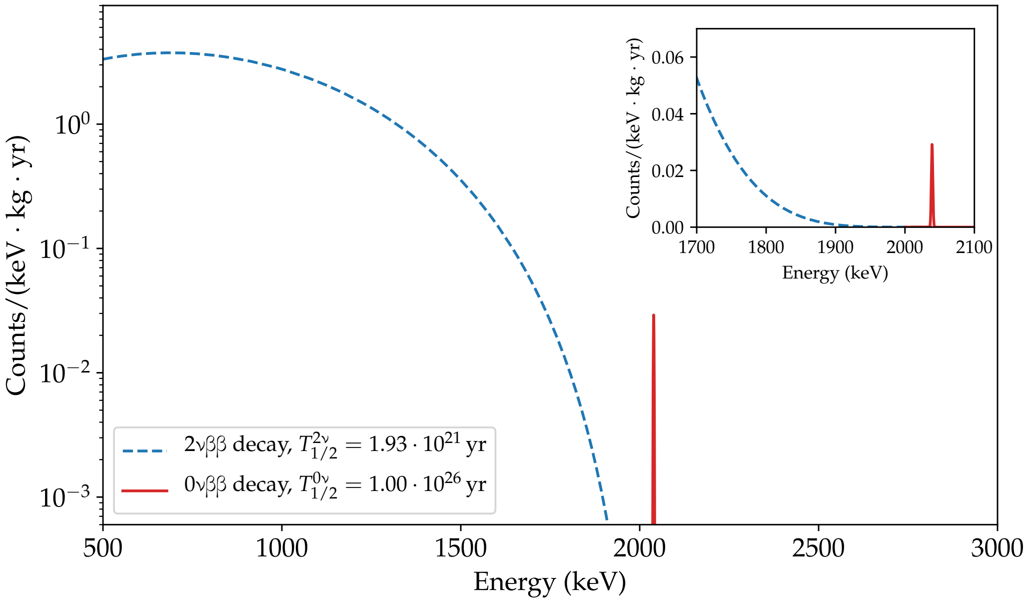

Figure 2.7: Energy histogram of the experimental signature for $2\nu\beta\beta$ and $0\nu\beta\beta$-decay for ^{76}Ge with a $Q_{\beta\beta} \approx 2039\,\mathrm{keV}$: while the $2\nu\beta\beta$ decay has a continuous spectrum, the $0\nu\beta\beta$ has a sharp peak at $Q_{\beta\beta}$-value with width determined by the energy resolution. Figure from [32] based on data by Y. Kermaidic.

It is forbidden in the SM and is, therefore, a BSM process with a decay rate of $T^{0\nu}_{1/2} \propto Q^5$ where Q symbolizes the nuclear transition energy. This lepton number violation could be linked to Baryon number violation via standard model sphaleron processes which are together with the two other Sakharov conditions a necessary criterion for the dynamic production of baryon asymmetry in the early universe, the dominance of baryonic matter over antimatter in the early universe [11] [48, 49]. In the standard interpretation, the decay is mediated by light massive Majorana neutrinos. It is visualized by the Feynman diagram in Figure 2.6b where the virtual neutrino emitted at the first vertex is absorbed as a virtual anti-neutrino at the second vertex. In general, this process could also be mediated by other mechanisms which violate lepton number by two units ($\Delta L = +2$). Hence, a black box, a system with input and output without knowledge of the conversion mechanism, is needed for the description of the neutrinoless double beta decay. If then the process does not contain any virtual Majorana neutrinos in the black box such as for the exchange of

[11] Standard model sphaleron processes are i.e. non-perturbative solutions to the electroweak field equations. The three Sakharov conditions are baryon number violation, C and CP violation as well as interactions out of thermal equilibrium.

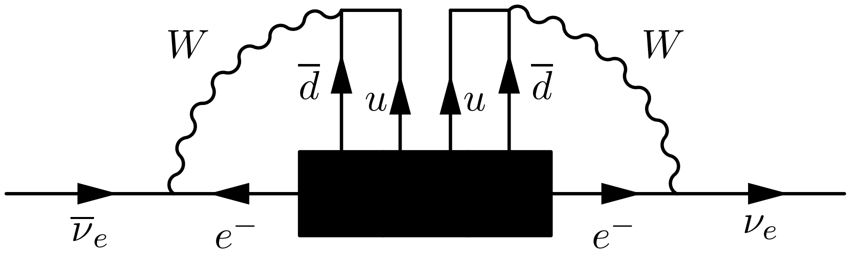

Figure 2.8: Schechter-Valle diagram where a none vanishing four loop Majorana mass term in case of a $0\nu\beta\beta$-decay occurs independent of the underlying mechanism in the black box. Figure taken from [53]

R-parity violating supersymmetric particles, right-handed-currrents or Higgs triplets, the connection between the $0\nu\beta\beta$-decay and the Majorana theory cannot be drawn that simple anymore [50, 51]. The Schechter-Valle theorem states that independent of the underlying process any realization that allows $0\nu\beta\beta$-decay contains non-zero effective Majorana mass term which corresponds to the Majorana nature of the neutrinos [12] [52]. This is shown in Figure 2.8. As already mentioned, the final state of the neutrinoless double beta decay contains only two electrons and the daughter nucleus. Because the mass difference between the daughter nucleus and the two electrons is huge (e.g. $2m_e = 2 \cdot 511\,\mathrm{keV} \ll m_{^{76}\mathrm{Ge}} \approx 70.9\,\mathrm{GeV}$), the nuclear recoil can be neglected so that the two emitted electrons share the total energy $Q_{\beta\beta}$ released in the decay, and the experimental signature is a mono-energetic peak centered at the $Q_{\beta\beta}$ value with the peak width determined by the detector resolution as illustrated in Figure 2.7.

2.2.1 Effective Majorana mass

If the $0\nu\beta\beta$-decay is mediated by the exchange of light neutrinos (c.f. Figure 2.6b), the mass observable is the effective neutrino mass $\langle m_{\beta\beta}\rangle$. According to Fermi's golden rule, the transition rate (or half life) can be derived as the product of the coupling strength between initial and final states for the respective transition operator (i.e. the matrix element $\mathscr{M}_{ij}$) and the related final state density [54]:

$$\frac{1}{T_{1/2}^{2\nu}} = G^{0\nu} \cdot g_A^4 \cdot \left(M^{0\nu} + \frac{g_\nu^{NN} m_\pi^2}{g_A^2} M_{cont}^{0\nu} \right)^2 \cdot \langle m_{\beta\beta}\rangle^2 \tag{2.27}$$

[12]The theorem works under the assumption of a description of the weak interaction by a local gauge theory.

Here, the phase space factor $G^{0\nu}$ depends on $Q^5_{\beta\beta}$ and the atomic number Z and has a value of $G^{0\nu} = 2.363 \times 10^{-15}\,\mathrm{yr}^{-1}$ for ^{76}Ge [42, 55]. For the axial-vector coupling g_A, it is convention to use an unquenched value of $g_A \approx 1.27$ though it is not clear if the quenching in $2\nu\beta\beta$ and $0\nu\beta\beta$ is the same as described above [56]. In contrast, the NME $M^{0\nu}$ can indeed be calculated from nuclear theory, but this calculations have large uncertainties and differ for ^{76}Ge between $2.66 \leq |M^{0\nu}| \leq 6.04$ [13] [57, 58]. $M^{0\nu}_{cont}$ is a recently introduced contact operator with its own hadronic coupling g^{NN}_{ν} normalized by the pion mass m_π [59].
The mass observable in the $0\nu\beta\beta$-decay is the effective Majorana mass which is a coherent sum of the different neutrino mass eigenstates m_i weighted with the PNMS mixing matrix elements $\mathcal{U}_{ij}$:

$$\langle m_{\beta\beta}\rangle = |\sum_i \mathcal{U}^2_{ij} m_i| \tag{2.28}$$

$$= |\cos^2\theta_{12}\cos^2\theta_{13}\, m_1 + e^{2i\alpha}\,\sin^2\theta_{12}\,\cos^2\theta_{13}\, m_2 + e^{2i\beta}\,\sin^2\theta_{13} m_3| \tag{2.29}$$

This rather complicated equation can be interpreted in a geometrical way as a vector sum of the three components as seen in Figure 2.9. Following the approach for the ordering of the three mass eigenstates m_i, one can express the effective Majorana mass $\langle m_{\beta\beta}\rangle$ as a function of the lightest neutrino mass m_{lightest} as illustrated in Figure 2.10 and distinguish three different regions:

- In the **normal mass ordering**, m_1 is the lightest neutrino m_{lightest} and by assuming the same approximations as above, $\langle m_{\beta\beta}\rangle$ can be expressed as $\langle m_{\beta\beta}\rangle \simeq |\cos^2\theta_{12}\, m_1 + e^{2i\alpha}\sin^2\theta_{12}\sqrt{m_1^2 + \Delta m^2_\odot}|$. This leads to a flat area for $m_{\text{lightest}} \lesssim 10^{-3}\,\text{eV}$ whereas because $e^{i\alpha} = \pm 1$ for $\alpha = 0/\pi$, $\langle m_{\beta\beta}\rangle$ may vanish due to the Majorana phase in the range between $10^{-3}\,\text{eV} \lesssim m_{\text{lightest}} \lesssim 10^{-2}\,\text{eV}$ even though all m_i are non-vanishing.

- In the **inverted mass ordering**, m_3 is the lightest neutrino mass m_{lightest} and $\langle m_{\beta\beta}\rangle$ can be approximated by $\langle m_{\beta\beta}\rangle \simeq |\Delta m_{\text{atm}}|\,\cos^2\theta_{13}(\cos^2\theta_{12} + e^{2i\alpha}\sin^2\theta_{12})$. This leads to a flat band over the whole area because it limits $\langle m_{\beta\beta}\rangle$ between $|\Delta m_{\text{atm}}|\,\cos^2\theta_{13} \leq \langle m_{\beta\beta}\rangle \leq |\Delta m_{\text{atm}}|\,\cos^2\theta_{13}\,\cos 2\theta_{12}$. This band can be fully tested by future $0\nu\beta\beta$-decay experiments as shown in the Figure 2.10.

- In the **quasi-degenerate** regime where the lightest neutrino mass m_{lightest} is large compared to the mass splitting ($m_{\text{lightest}} \gg |\Delta m_{\text{atm}}| \gg |\Delta m_\odot|$),

[13] The four main models are the nuclear shell model (NSM), the quasi-particle random phase approximation (QRPA), the interacting boson model (IBM) and the energy-density functional (EDF).

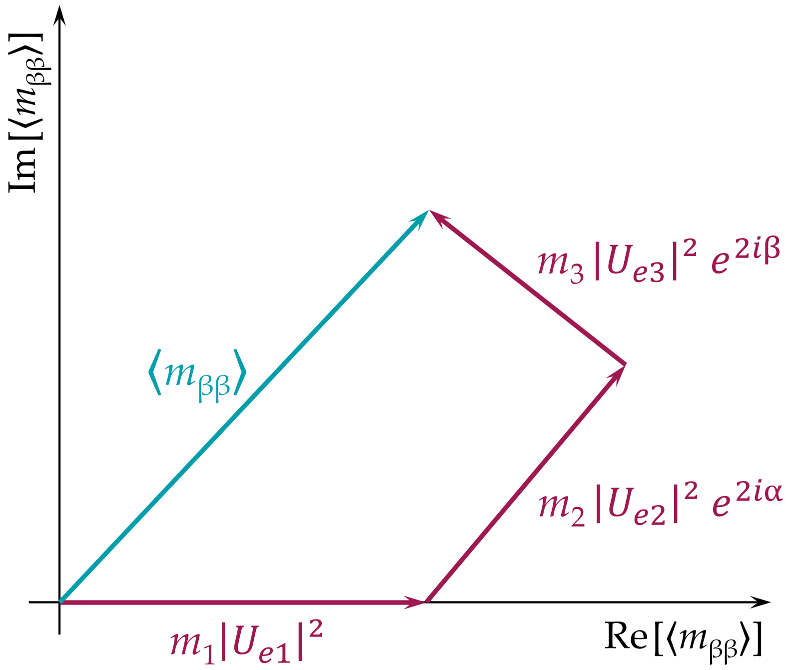

Figure 2.9: The effective Majorana mass $\langle m_{\beta\beta}\rangle$ can be interpreted as vector sum by splitting the three components into real and imaginary parts where the m_1 component has no imaginary component/Majorana phase by choice in the PNMS matrix. Figure from [32].

both scenarios behave similar and $\langle m_{\beta\beta}\rangle$ can be approximated by a common neutrino mass m_0 with $m_0\cos^2\theta_{12} \leq \langle m_{\beta\beta}\rangle \leq m_0$.

2.2.2 Experimental sensitivity

To determine the performance of an experiment searching for neutrinoless double-beta decay, one can define the experimental sensitivity as the ratio of the number of expected signal events N_S and the number of background events N_B. The number of signal events N_S is described by

$$N_S = N_{\beta\beta} \cdot P(t) \cdot \epsilon_{\text{det}} \tag{2.30}$$

with $N_{\beta\beta}$ the initial number of $0\nu\beta\beta$-decaying isotopes, ϵ_{det} the total detection efficiency of the detector and $P(t)$ the probability to decay after measuring

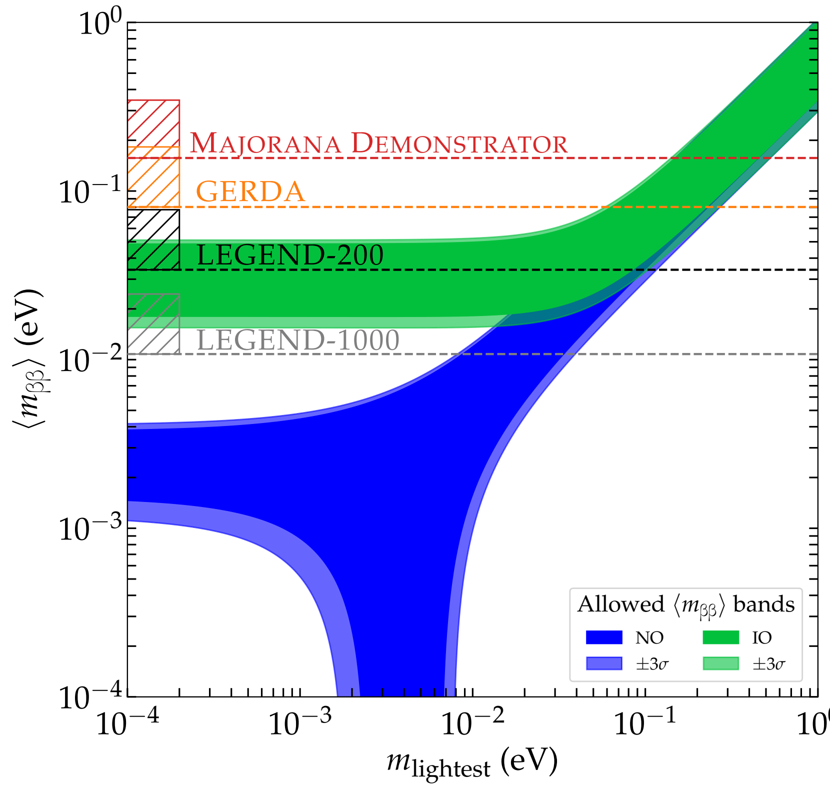

Figure 2.10: Effective Majorana mass $\langle m_{\beta\beta}\rangle$ as a function of the lightest neutrino mass m_{lightest} where the allowed bands correspond to the normal mass ordering (blue) and inverted mass ordering (green) with the band widths corresponding to the best fit values of the neutrino parameters from [60] and the Majorana phases α and β varied from $[0, 2\pi]$. Furhtermore, sensitivity lines for the GERDA, Majorana Denonstrator and LEGEND are shown, too. Figure from [32].

time t being

$$P(t) = \frac{\log(2)}{T_{1/2}^{0\nu}} \int_0^t \exp\left(-t' \frac{\log(2)}{T_{1/2}^{0\nu}}\right) \overset{t \ll T_{1/2}^{0\nu}/\log(2)}{\approx} t \frac{\log(2)}{T_{1/2}^{0\nu}} \tag{2.31}$$

with $T_{1/2}^{0\nu}$ the half-life of the decay. With the total mass M, the atomic mass m_a and the enrichment factor f_{enr} of the initial isotope, the number of expected signal events can be expressed as

$$N_S = \frac{M \cdot f_{\text{enr}}}{m_a} \cdot t \, \frac{\log(2)}{T^{0\nu}_{1/2}} \cdot \epsilon_{\text{det}} \tag{2.32}$$

$$= \frac{\log(2)}{m_a} \cdot \frac{f_{\text{enr}} \cdot \epsilon_{\text{det}}}{T^{0\nu}_{1/2}} \cdot M \cdot t \tag{2.33}$$

with $M \cdot t$ called the exposure [61].
The number of background events is calculated to be

$$N_B = BI \cdot \Delta E \cdot M \cdot t \tag{2.34}$$

with BI the background index in the region of interest (ROI) expressed in cts/(FWHM · t · yr) and ΔE the ROI energy window around the $Q_{\beta\beta}$-value. For a signal discovery sensitivity of 3σ assuming Poissonian statistics, this leads to discovery half-life of

$$T^{0\nu}_{1/2}(3\sigma\,\text{DS}) \propto \begin{cases} f_{\text{enr}} \cdot \epsilon_{\text{det}} \cdot \sqrt{\frac{M \cdot t}{BI \cdot \Delta E}} & \text{with background} \\ f_{\text{enr}} \cdot \epsilon_{\text{det}} \cdot M \cdot t & \text{background} - \text{free} \end{cases} \tag{2.35}$$

for the case with and without background. Figure 2.11 illustrates this for ^{76}Ge where one can see that a low BI togehter with high exposure meaning high mass M measured for a long time t is crucial for any $0\nu\beta\beta$-decay experiment to reach certain sensitivity goals.

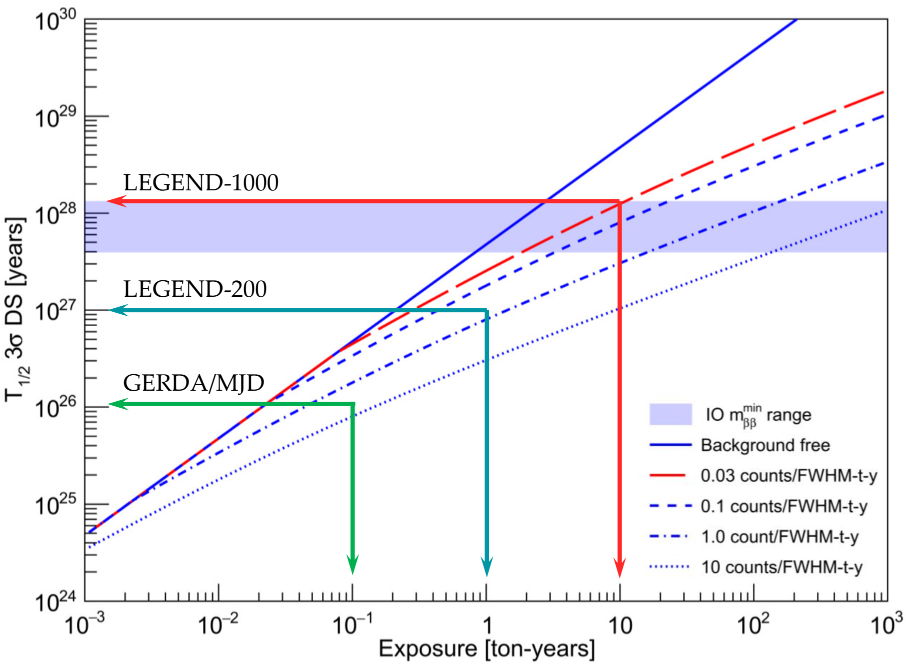

Figure 2.11: Experimental sensitivity in terms of half-life $T_{1/2}^{0\nu}$ as a function of exposure $M \cdot t$ for ^{76}Ge. While the blue band shows the allowed region for the IO, the solid blue line symbolizes the background-regime and the other dashed line the presence of backgrounds. Figure from [62, 63]

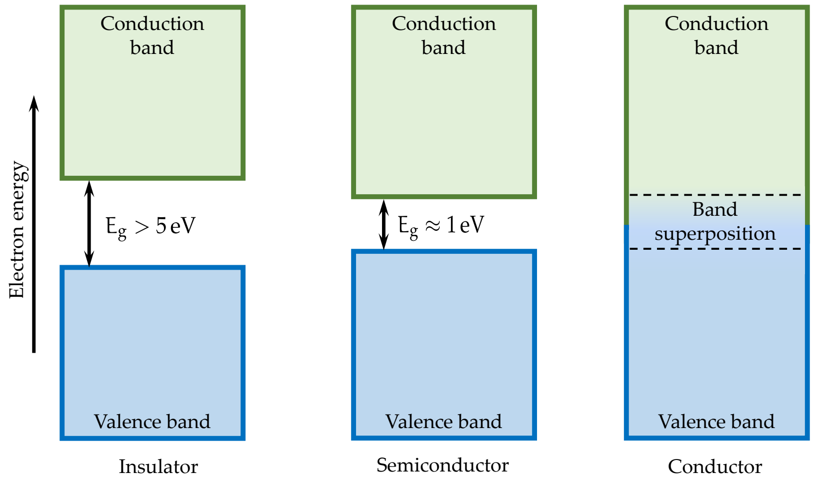

Figure 2.12: Band structure in solids for the cases of an insulator, a semiconductor, and a conductor. In conductors, valence and conduction band are overlapping while the energy gap between the two bands is about $E_g \approx 1\,\mathrm{eV}$ in semiconductors and $E_g > 5\,\mathrm{eV}$ for insulators.

2.3 Semiconductor Detectors

2.3.1 Detector basics

To describe detector physics, it is crucial to understand the physics of the underlying material and their properties, in the case of LEGEND especially germanium. Germanium is a solid crystal as well as a direct semiconductor and is widely used for the spectroscopic detection of ionizing radiation. Starting from the physical fundamentals, a solid can be described by its underlying energy bands of the electrons in their shells which normally consist of two individual bands: the conduction band and the valence band (c.f. Figure 2.12) Because electrons in the conduction are free to move, they contribute to the electrical conductivity of the material. As illustrated in Figure 2.12, the two bands in conductors are overlapping so that electrons can move easily between the two bands, for example, by thermal excitation, while in insulators, the bands are separated by a large energy gap $E_g > 5\,\mathrm{eV}$ so that the valence band is fully occupied and the conduction band is empty. In contrast, the bandgap in semiconductors is small (e.g. $E_g > 0.66\,\mathrm{eV}$ for Germanium) so that a valence electron can overcome the gap if it gains sufficient thermal energy while leaving an associated hole in the valence band, which represents a net positive charge. The new conduction electron and the hole always occur as a so-called *electron-hole pair*.

This bandgap in semiconductors can be used for radiation detection where a particle can enter the material under excitation of valence electrons into the conduction band. This leads to the creation of a certain number of electron-hole pairs, which are directly proportional to the absorbed energy and can be represented by

$$n = \frac{E_{abs}}{\epsilon(T)} \tag{2.36}$$

with ϵ, the average energy needed to create an electron-hole pair which is temperature-dependent and can be calculated for germanium by [64].

$$\epsilon(T) = 2.2 \cdot E_g(T) + 1.99 \cdot E_g^{3/2}(T) \cdot \exp\left(4.75 \frac{E_g(T)}{T}\right) \tag{2.37}$$

Hereby, the energy dependent band gap can be described by Varshni's empirical formula which corresponds for germanium to [65, 66]

$$E_g(T) = E_g(0\,\mathrm{K}) - \frac{4.774 \times 10^{-4}\,\mathrm{eV\,K^{-2}} \cdot T^2}{T + 235\,\mathrm{K}} \tag{2.38}$$

If in the presence of an external electric field the so produced electrons and holes can be collected at the anode and the cathode, the deposited energy can be measured. Following this, it is necessary to have a high number of electron-hole pairs created which can be achieved by a low $\epsilon(T)$ which would require a higher temperature as illustrated by the parametrization of $\epsilon(T)$ from Equation 2.37 in Figure 2.13a. On the other hand, a higher temperature also decreases the band gap as illustrated by the parametrization of $E_g(T)$ from Equation 2.38 in Figure 2.13b. The probability of an electron to overcome the band gap by thermal excitation is described by a Boltzmann distribution [67]

$$P(T) \propto T^{3/2} \exp\left(-\frac{E_g}{2kT}\right) \tag{2.39}$$

which increases strongly with higher temperatures as shown in Figure 2.13c. The current induced by these electrons overcoming the band gap is called leakage current and is a source of noise while too high leakage currents prevent the detectors from being functional. Therefore, a compromise has to be found which is typically at liquid nitrogen (LN$_2$) temperatures ($T = 77\,\mathrm{K}$) with $\epsilon(77\,\mathrm{K}) = 2.96\,\mathrm{eV}$ and $E_g(77\,\mathrm{K}) = 0.73\,\mathrm{eV}$ or at LAr temperatures ($T = 87\,\mathrm{K}$) with $\epsilon(87\,\mathrm{K}) = 2.91\,\mathrm{eV}$ and $E_g(87\,\mathrm{K}) = 0.73\,\mathrm{eV}$.
Because ideal crystals without any impurities cannot be produced, small residual crystal impurities are always included during manufacturing and affect the

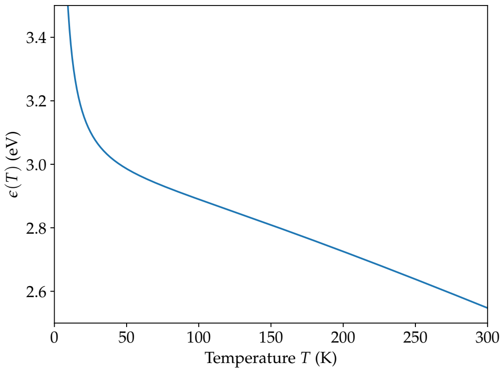

a) Parametrization of temperature dependent $\epsilon(T)$ for germanium

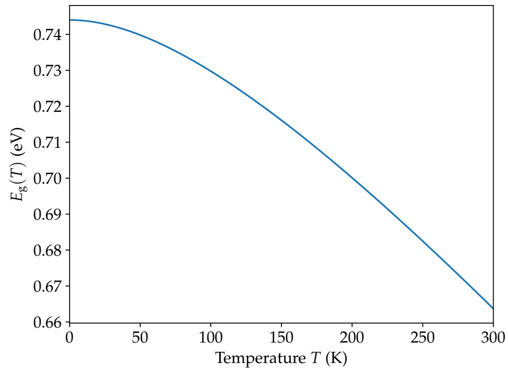

b) Parametrization of temperature dependent band gap $E_g(T)$ for germanium

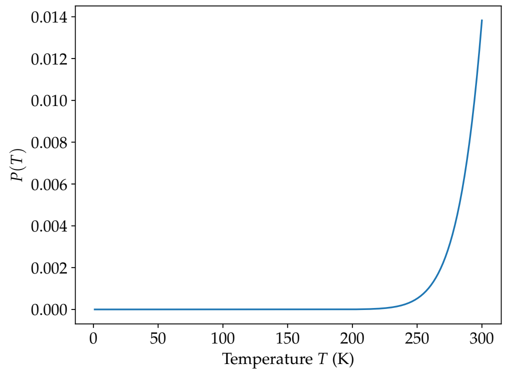

c) Temperature dependent transition probability from valence to conduction band for germanium

Figure 2.13: Parametrizations of $\epsilon(T)$, band gap energy $E_g(T)$ and transition probability $P(T)$ for germanium versus temperature. Figures from [32].

band gap and band levels. If an *acceptor* impurity is included in the crystal, e.g. any group III element like boron in a crystal of group IV like germanium, the crystal is called p-type (presence of positive acceptor impurities) because e.g. an *acceptor* atom with three valence electrons is inserted into a four four-valent crystal so that an additional hole is available as shown in Figure 2.14a. On the other hand, if a *donor* impurity is included in the crystal, e.g. any group V element like arsenic in a crystal of group IV like germanium, the crystal is called n-type (presence of negative donor impurities) because e.g. an *donor* atom with five valence electrons is inserted into a four four-valent crystal so that one additional electron is available as shown in Figure 2.14b. Often times, both types of impurities are present in a crystal. Furhtermore, intentional doping

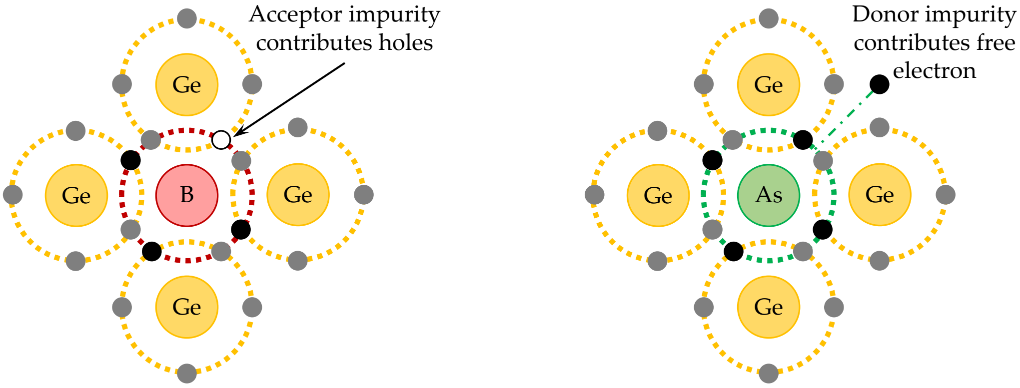

a) Acceptor impurity **b)** Donor impurity

Figure 2.14: Acceptor and donor impurities in the case of germanium as group IV element with boron as acceptor impurity of group III which creates an additional hole (p-type) 2.14a and with arsenium as donor impurity of group V with which creates an additional electron (n-type). Figures from [32].

can be used to compensate imbalances in the impurities as well as making electrical contact with semiconductor devices like readout systems [67].
By combining this two types of materials as illustrated in 2.15, free holes and free electrons can diffuse into the opposite material and recombine in the junction between these materials called p-n-junction. This so-called *depletion zone* where no free charge carriers are left can be used as *active volume* of a semiconductor detector. If an electron-hole pair is produced in this *active volume*, the electron and hole can be separated by an external electric field and read out by an amplification system. The semiconductor detector then acts as a $\mathrm{n}^+ - \mathrm{p} - \mathrm{p}^+$ diode. Furthermore, the width of the depleted zone can be enlarged by applying a positive bias voltage V_{bias} to the n-type material which increases the potential difference at the p-n-junction which is described by the relation

$$d \propto \left(\frac{V_{bias}}{e \cdot N_{impurity}} \right)^{1/2} \tag{2.40}$$

where $N_{impurity}$ is the net impurity concentration. When this so-called *reverse bias voltage* is applied to the detector, the detector is called fully depleted if no free charge carrier are left in the depletion zone. This voltage is called *depletion voltage* where the detector acts electrically as a capactitor with capacitance C_D as soon as the *depletion voltage* is reached.

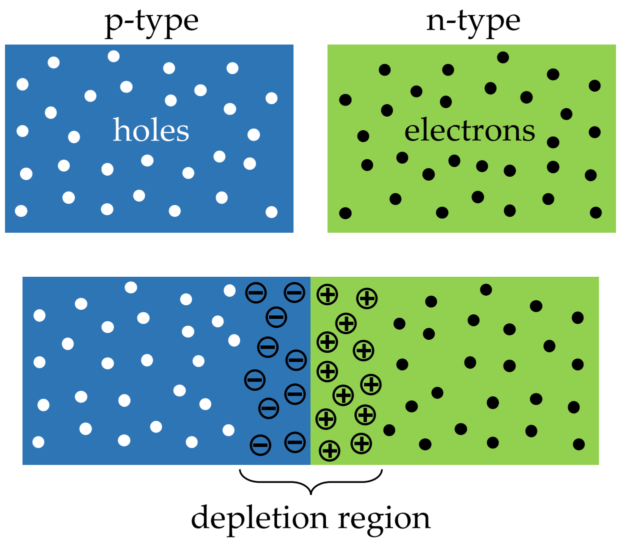

Figure 2.15: Combination of a p-type and n-type detector material where the free electrons and free holes diffuse into the opposite material and recombine while leaving the so-called depletion zone without any free charge carriers.

2.3.2 High-purity germanium detectors

In the typical way of detector production which is also used for LEGEND, germanium detectors are made of a single crystal of p-type material. The p^+ contact or signal readout contact is formed by boron implantation with a thickness of around 100 nm to build up a p-type junction. The n^+ contact to form the $\mathrm{n}^+ - \mathrm{p} - \mathrm{p}^+$ diode is formed by drifting lithium onto the surface of the detector with a thickness of around $1 - 2$ mm. To achieve then an *active region* of $\mathcal{O}(\mathrm{cm})$, the impurity concentration has to be of $\mathcal{O}(10^{10}\,\mathrm{atoms\,cm^{-3}})$ with a *reverse bias voltage* of $\mathcal{O}(\mathrm{kV})$. Germanium detectors with such low impurity concentrations are called HPGe detectors.

2.3.2.1 Signal formation and weighting potential

With a positive high voltage (HV) applied to the n^+ contact, the detector bulk can be fully depleted. If a particle now enters the detector bulk, electron-hole pairs are created along the trajectory, and the signal formation process starts: since the electrons and holes are moving towards their electrodes, they induce mirror charges up to the point where all generated electron-hole pairs are collected at their certain electrode. The time it takes for the charges to be fully collected is called drift time τ_{drift}. The observable net charge $Q(t)$ and current $I(t)$ induced at the electrodes can be calculated by the Shockley-Ramon theorem to [68, 69]

$$Q(t) = -Q \cdot [\Phi(\vec{r}_h(t)) - \Phi(\vec{r}_e(t))] \tag{2.41}$$

$$I(t) = Q \cdot [\vec{E}(\vec{r}_h(t)) \cdot \vec{v}_h(t) - \vec{E}(\vec{r}_e(t)) \cdot \vec{v}_e(t)] \tag{2.42}$$

where Q is the total charge of the incoming particle, $\Phi(\vec{r})$ the weighting potential and $\vec{E}(\vec{r})$ the weighting field at position $\vec{r}$ and $\vec{r}_{h(e)}(t)$ and $\vec{v}_{h(e)}(t)$ the position and velocity of the hole (electron) cloud at time t, respectively. The weighting potential $\Phi(\vec{r})$ can be computed by solving the Laplace equation

$$\Delta\Phi(\vec{r}) = 0 \tag{2.43}$$

for the particular detector geometry under the boundary conditions that the voltage at the p^+ contact is unity $\Phi(\vec{r}_{\mathrm{p}^+}) = 1$ and zero at the n^+ contact $\Phi(\vec{r}_{\mathrm{n}^+}) = 0$ which is only numerically solvable often times. The weighting field can then be obtained by the gradient of the weighting potential [67]

$$\vec{E}(\vec{r}) = \nabla\Phi(\vec{r}) \tag{2.44}$$

The so produced signals are typically very small and need to be amplified with a CSA: the induced current at the p^+ contact is converted into a voltage signal and amplified. The detailed functionalities of CSAs is explained in the Section 3.1.

2.3.2.2 Detector geometries

In the LEGEND experiments, three types of detector geometries are used which are explained in this section. These detector types are shown in Figure 2.16 together with their simulated weighting potential and the drift paths of some events in the bulk.

- **BEGe detectors** have a low detector capacitance of $C_D \approx 3-5\,\mathrm{pF}$ at full depletion. As illustrated in Figure 2.16a, the detectors have a large cylindrical shape and a short length. The p^+ contact has a larger radius of up to 7 mm and is separated from the n^+ contact which covers the whole bottom and mantle surface by an insultating, passivated groove with a typical depth of 2 mm and an outer diameter of 21 mm. BEGe detectors are less sensitive to surface backgrounds and have enhanced Pulse Shape Discrimination (PSD) capabilities which enables efficient background rejection [70, 71].

- **PPC detectors** are higher then BEGe detectors while showing the same cylindrical shape as illustrated in Figure 2.16b. The p^+ contact is made by a small dimple in the center of the top surface with a radius of $3-4$ mm and a depth of $1-2$ mm which leads to a lower capacitance of $C_D \approx 1-2$ pF at full depletion compared to traditional semi-coaxial detectors which are no longer used in modern $0\nu\beta\beta$ experiments due to their poor PSD capabilities. In addition, PPC detectors have lower energy threshold of < 1 keV which makes them usable in all kind of radiation applications including low-energy nuclear reciols such as in dark matter [72, 73] and coherent elastic neutrino-nucleus scattering [74, 75].

- **ICPC detectors** are the largest of all three detector types with a typical cylindrical shape with diameter up to 100 mm and typical length of $80-90$ mm and have been proposed recently [76]. The p^+ contact is located at the top surface separated from the n^+ contact by an insulating groove or passivation layer. In contrast to the other types, it features a concentric borehole which avoids undepleted regions together with optimized electric fields in the inside. Since the signal discovery sensitivity can be easily increased by increasing the isotope mass, ICPC detectors with their much higher masses of $\mathcal{O}(1\,\text{kg})$ are favoured as baseline design for the future ton-scale experiments like LEGEND-1000 because they fulfill the same advantages as BEGe and PPC detectors in terms of low capacitance, low threshold and good background rejection performance while having $30-40\%$ lower surface to volume ratio which makes them less susceptible to surface backgrounds. Nevertheless, the extended size increases drift times to values around $\tau_{drift} \approx 2\,\mu$s where collective effects like diffusion and self-repulsion of the charge cloud have to be taken into account [77].

2.3.3 Interaction of particles with matter

A key factor in the understanding of radiation detectors is the interaction of particles with matter. In the following section, these fundamentals are explained ordered according to the type of the incoming particle.

2.3.3.1 Charged particles

Heavy charged particles with masses $\gtrsim 1$ GeV interact via electromagnetic force in inelastic collisions with the shell electrons of the atoms while they are traverse through matter, leaving ions behind [67]. The Bethe-Bloch formula describes the average energy loss $\mathrm{d}E$ per unit path length $\mathrm{d}x$ for a single charged particle of charge ze with velocity $v = \beta c$ through a material with number density N

and atomic number Z [67]:

$$-\left\langle \frac{\mathrm{d}E}{\mathrm{d}x} \right\rangle = \frac{4\pi e^4 z^2}{m_e v^2} NZ \left[\log\left(\frac{2m_e v^2}{I} \right) - \log(1-\beta^2) - \beta^2 \right] \tag{2.45}$$

with m_e the electron mass, and I the average excitation and ionization potential of the absorber material. Absorber materials with higher electron density NZ have a higher stopping power. Because alpha particles have a $z = 2$ and Equation 2.45 shows a z^2 dependence, they have a short mean free path which can be approximated by the continous slowing down approximation (CSDA) which assumes that the energy loss rate at every point of the track is equal to the total stopping power which is possible since alpha particle interactions mainly take place at a single site [67]. Figure 2.17a illustrates the CSDA for alpha particles in germanium and LAr and shows that alpha particles with energies $\mathcal{O}(1\,\mathrm{MeV})$ traverse only up to $\mathcal{O}(10\,\mu\mathrm{m})$ and are therefore already stopped at the p^+ and n^+ contacts at the mantle surface of the detectors.

Because the Bethe formula in Equation 2.45 assumes that the mass of the incoming particle is much higher than for the shell electrons, these assumptions cannot be held for electrons and positrons anymore. The energy loss due to excitation and ionization is more complex: low energy electrons lose their energy mainly via ionization where above a certain critical energy E_C the loss is dominated by Bremsstrahlung which is the radiation of a photon in the electrostatic field of a nucleus. The critical energy can be approximated by [78]

$$E_C \approx \frac{800\,\mathrm{MeV}}{Z} \;\rightarrow\; E_C^{\mathrm{Ge}} \approx 25\,\mathrm{MeV} \tag{2.46}$$

with Z the nucleus charge. Following Equation 2.46 and the CSDA for electrons shown in Figure 2.17b, the energy loss is driven by ionization up to $\mathcal{O}(\mathrm{MeV})$ and the average path length in germanium and LAr is up to $\mathcal{O}(\mathrm{mm})$.
Positrons behave almost the same as electrons and only differ if their are almost at rest at $E_{e^+} \lesssim 10\,\mathrm{keV}$ where they can annihilate with another electron from the absorber material under the production of two photons with $E_\gamma = 511\,\mathrm{keV}$ each.

2.3.3.2 Gamma radiation

Gamma radiation as highly penetrating radiation is strongly dependent on the energy and the atomic number of the absorber material. The attenuation law of gamma rays in terms of mass attenuation is described by the Beer-Lambert law, which is a formula for the radiation intensity $I(x)$ [67]:

$$I(x) = I_0 \cdot \exp\left(-\lambda\frac{\mu}{\rho}\right) \text{ with } \lambda = \rho x \tag{2.47}$$

$$\begin{aligned} \frac{\mu}{\rho} &\propto \sum_i \sigma_i \\ &= \sigma_{PA} + \sigma_{IS} + \sigma_{PP} \end{aligned} \tag{2.48}$$

Here, I_0 is the initial intensity, μ the linear attenuation coefficient and ρ the mass density of the absorber material. Figure 2.18 shows the total attenuation coefficient with all three relevant effects included. It is clearly visible that Compton scattering is the dominant process at the $Q_{\beta\beta}$ value while the other two are about two orders of magnitude less dominant. The total mass attenuation coefficient $\frac{\mu}{\rho}$ can be described by a sum of the cross sections σ_i of these three main interaction processes:

1. **Photoelectric absorbtion (PA)**: Photoelectric absorbtion is most dominant at low energies up to about $\lesssim 150\,\text{keV}$ for ^{76}Ge where the incident photon is fully absorbed by one of the shell electrons and is subsequently emitted, leaving an excited absorber atom behind, which is then de-excited by the emission of characteristic X-ray photons or Auger electrons. If the electron is fully absorbed, a characteristic peak called full energy peak (FEP) can be recognized in the energy spectrum [67].

2. **Incoherent scattering (IS) (Compton scattering)**: Compton scattering is most dominant at energies in the range from 150 keV to 8 MeV for ^{76}Ge where the photon scatters off a bound or free electron with an angle $0 \leq \theta \leq \pi$ to its original direction. The energy of the scattered photon is reduced to

$$E'_\gamma = \frac{E_\gamma}{1 + \frac{E_\gamma}{m_e c^2}(1 - \cos\theta)} \tag{2.49}$$

   where the difference in energy is carried away from the electron recoil which is shown in Figure 2.19. Since the electron share the total energy, Compton scattering is visible as the so-called Compton continuum in the energy spectrum with the Compton edge being a visible shoulder at the maximum energy

$$\max(E_e) = E_e(\theta = \pi) = \frac{2E_\gamma^2}{2E_\gamma + m_e c^2} \tag{2.50}$$

3. **Pair production (PP) and pair annihilation**: Pair production is most dominant at energies $\gtrsim 8\,\mathrm{MeV}$ for ^{76}Ge where the incident photon reacts with a nucleus in the absorber material so that it is converted into an electron-positron pair (pair prodcution) while the pair shares the energy

$$E_{\text{pair}} = E_\gamma - 2m_e c^2 \text{ with } E_\gamma \geq 2 \cdot 511\,\mathrm{keV} \tag{2.51}$$

   Following this, the positron is slowed down in the absorber material and subsequently annihilates with another electron (pair annihilation) under the emittance of two photons with 511 keV back to back which is illustrated in Figure 2.20. These two photons trigger a special event topology in a germanium detector:

   - If the process happens outside the detector, one of the two photons may enter the active volume leading to a characteristic 511 keV peak in the energy spectrum.
   - If the process happens inside the detector, three possibilites exists:
     a) If the two photons are absorbed inside the active volume, a gamma peak at the full initial energy E_γ of the incident photon can be recognized in the energy spectrum called full energy peak (FEP).
     b) If one of the two photons can escape the active volume, a gamma peak at $E_\gamma - 511\,\mathrm{keV}$ is visible in the energy spectrum called single escape peak (SEP)
     c) If both photons can escape the active volume, a gamma peak at $E_\gamma - 2 \cdot 511\,\mathrm{keV}$ is visible in the energy spectrum called double escape peak (DEP)

   The explained spectral features are illustrated in Figure 2.21 for a ^{228}Th calibration measurement with a germanium detector. [14]

[14] In principle, there is also the possibility that only a fraction of the energy of the annihilation photons is deposited in the detector.

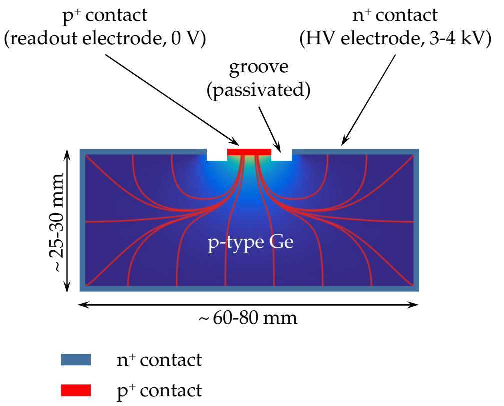

a) Broad energy germanium (BEGe) detector

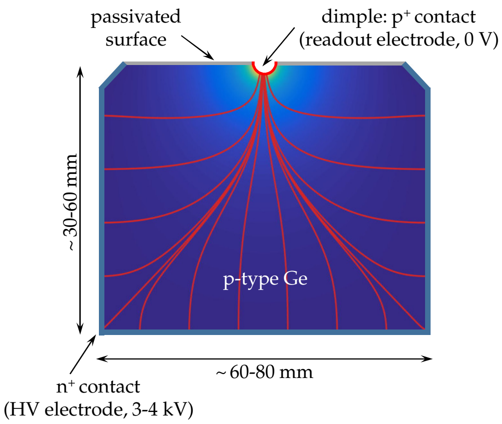

b) P-type point contact (PPC) detector

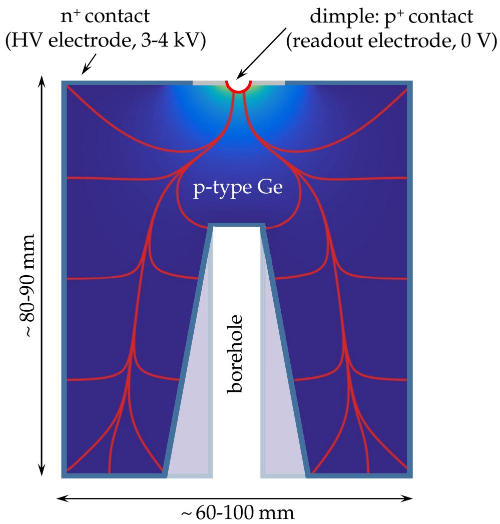

c) Inverted coaxial point contact (ICPC) detector

Figure 2.16: Overview of the detector types used in LEGEND: BEGe (a), PPC (b) and ICPC detector (c). The figure shows the electrode arrangements and indicates typical dimensions. Moreover, the weighting potential inside the detector (blue and yellow areas correspond to low and high values, respectively), and the drift paths (red thin lines) are illustrated. Figure from [32].

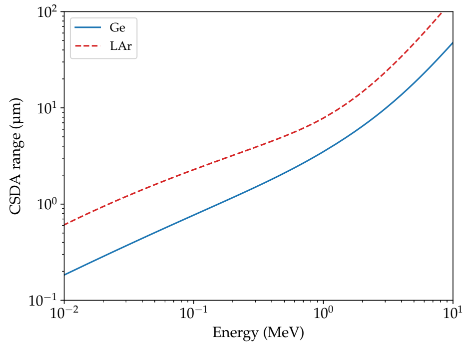

a) CSDA range of alpha particles in germanium and LAr

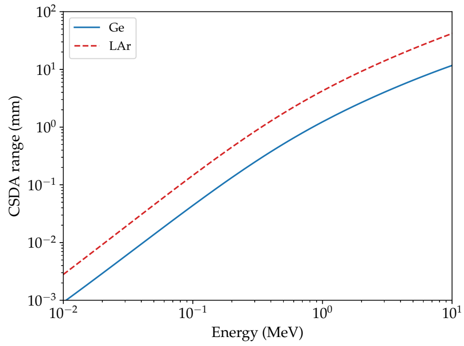

b) CSDA range of electrons in germanium and LAr

Figure 2.17: continous slowing down approximation (CSDA) for alphas 2.17a and electrons 2.17b in germanium and liquid argon

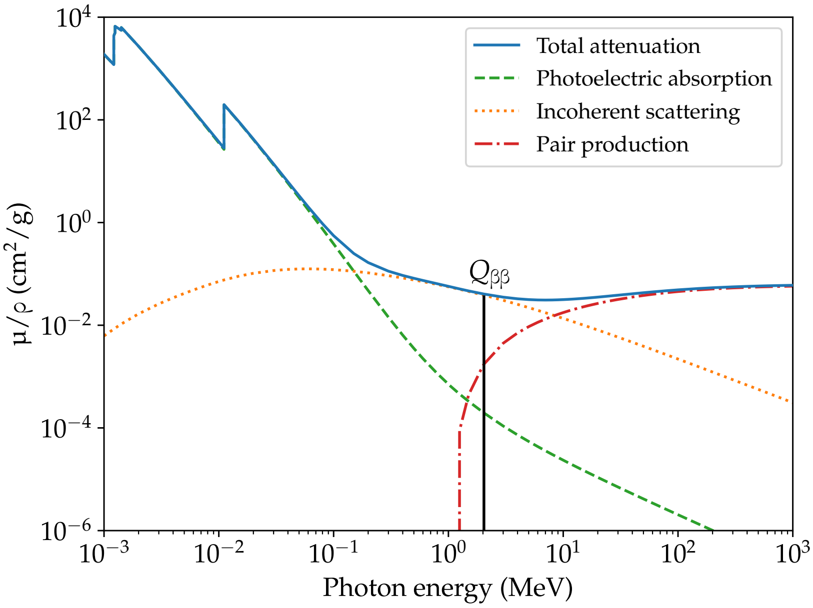

Figure 2.18: Attenuation coefficient μ/ρ in ^{76}Ge as a function of the photon energy E_γ where the three main processes, photoelectric absorbtion (PA), incoherent scattering (IS) and pair production (PP) are shown in their corresponding energy range. Figure from [32].

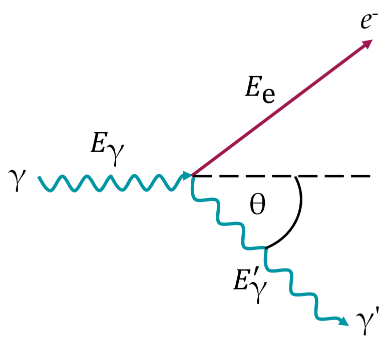

Figure 2.19: Illustration of Compton scattering where an incoming photon γ scatters off an bound or free electron e^- and is subsequently deflected through an angle θ with reduced energy E_γ. Figure from [32].

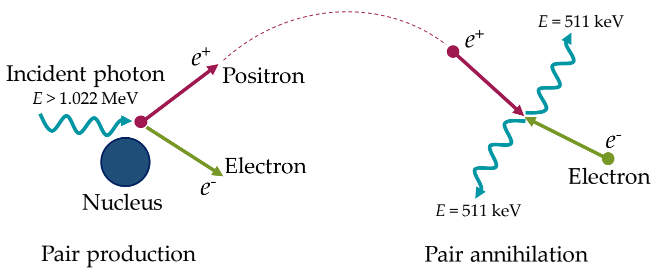

Figure 2.20: Pair production and pair annihilation where an incident photon interacts with the nucleus under production of an electron-positron. The positron is then slowed down and finally annihilates with another electron under the production of two 511 keV photons back to back. Figure from [32].

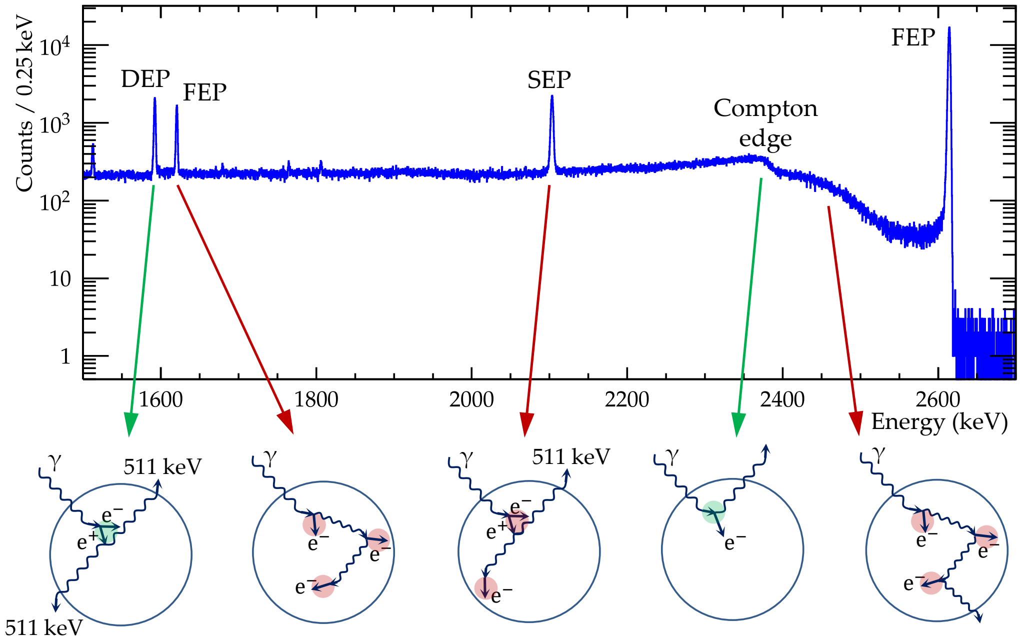

Figure 2.21: Energy spectrum of a ^{228}Th calibration measurement: The full energy peak (FEP) are events where the whole energy of the incident photon is absorbed in the active volume, the single escape peak (SEP) where one of the annihilation photons can escape the active volume and the double escape peak (DEP) where both annihilation photons can escape the active volume. The compton edge is characterized by the the maximum deflection angle of the incident photon under Compton scattering where events after the Compton edge can happen due to multiple Compton scattering. Figure from [32].

2.4 The Large Enriched Germanium Experiment for $0\nu\beta\beta$ Decay

This Chapter explains the detailed plans for the LEGEND experiment in its two phases, namely LEGEND-200 and LEGEND-1000, as well as their contributing backgrounds and sensitivity. The LEGEND experiment and its collaboration aim to a ton-scale search for $0\nu\beta\beta$ decay in ^{76}Ge in a phased approach with a discovery potential beyond 10^{28} yr which would cover the whole inverted mass ordering (IO) in the neutrino sector [63]. It is based on the excellent performance of the two predecessor experiments, namely the European-based GERDA experiment and the US-based MJD experiment: the GERDA experiment developed the LAr-veto system for background reduction reaching a so far unachieved background index while MJD had perfect clean materials and electronics very close to the detector, which resulted in the best energy resolution of any HPGe detector based $0\nu\beta\beta$ experiment so far.

2.4.1 LEGEND-200

In the first phase of the Large Enriched Germanium Experiment for $0\nu\beta\beta$ Decay experiment called LEGEND-200, up to 200 kg of HPGe detectors will be operated for a period of about five years in the existing GERDA infracstructure at LNGS resulting in a target exposure of $M \cdot t = 1\,\mathrm{t\,yr}$. As direct follow up experiment of GERDA, LEGEND-200 also deploys the detectors in LAr which acts both as cooling medium as well as an active shielding. The LAr veto system which was developed in GERDA phase II uses the scintilattion light in LAr with higher optical purity to increase the attenuation length to $> 60\,\mathrm{cm}$ at 128 nm. Since the detectors are surrounded by novel wavelength-shifting reflector (WLSR) to shift the wavelength of the scintillation to reflect visible light which can then be readout, one can set veto cuts on μ events as well as on γ events which can escape the active volume of detectors. This setup is illustrated in Figure 2.22. Following the approach from Majorana Demonstrator, an enhanced signal readout electronics solution is in use, which further reduces electronic noise and therefore enhances energy resolution and PSD performance. Parts of this work show status and further improvements of this setup in the LEGEND-200 setup at LNGS.
In addition, novel low-mass detector base plates made of active transparent polyethylene naphthalate (PEN) (c.f. Figure 2.23) are used for detector holding structure since they are also scintillating and can therefore improve light collection efficiency of the LAr veto system [79]. The cleanroom was modified together with a novel lock system as well as a new detector mounting system and

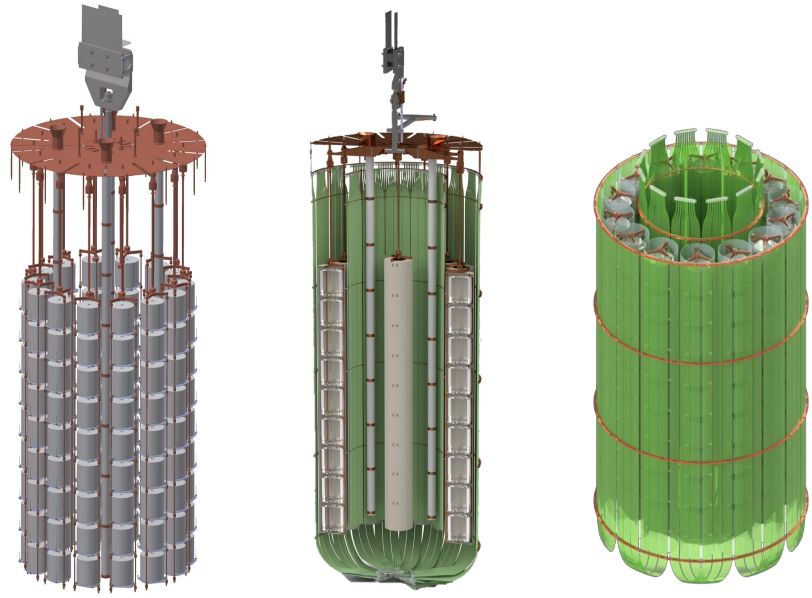

Figure 2.22: Artistic views of the LEGEND-200 setup. The figures show details of the detector array configuration (circular arrangement of strings, and of the LAr veto system (light-guiding fibers). Figures provided by M. Busch and M. Willers.

a novel data aquisition (DAQ) system was installed. At the moment, LEGEND-200 has started with the first measurements with 4 detectors in November 2021, for which results are presented in Chapter 3. However, construction and manufacturing of electronic components, detectors, etc. are still ongoing. Since the cryostat is filled with purified LAr and parts of the readout system and the DAQ are ready to start taking measurements; several test campaigns are currently ongoing to verify the functionality of all components together in the actual setup at LNGS.

2.4.2 LEGEND-1000

The final stage of the LEGEND experiment, called LEGEND-1000 will operate up to 1000 kg of HPGe detectors for 10 yr to reach a target exposure of $M \cdot t = 10\,\mathrm{t\,yr}$ [63]. The baseline designs contains the operation of ~ 400 ICPC detectors with masses of $\sim 2-3$ kg each. The current strategy plans to operate the detectors in four or five independent batches with loads of around 250 kg or 200 kg each in separate LAr cryostats so that single batches can already start data taking will others are being assembled. An artistic view of the experiment is

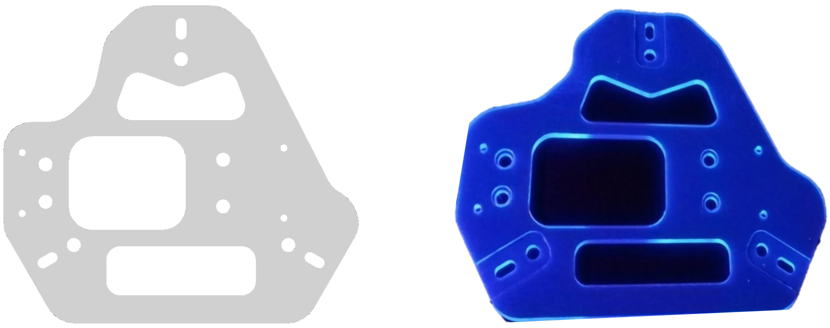

Figure 2.23: Low-mass polyethylene naphthalate (PEN) plates as drawing (left) and photograph where the scintillating properties are clearly shown in the blue region. Figures provided by L. Manzanillas.

illustrated in Figure 2.24. The baseline designs plan the tubes to be made from ultra-pure electroformed copper filled with so-called underground liquid argon (UG LAr) which has lower contents of the radioactive isotopes ^{42}Ar and ^{39}Ar due to its extraction from gas wells while the outer cryostat is filled with normal LAr. The exclusive use of ICPC detectors further suppress surface alpha events. As experiment sites, SNOLAB as well as LNGS are taken into consideration where SNOLAB has by far the lowest muon flux in the laboratory and therefore background index [63]. Since the LNGS as experiment site has several advantages in terms of construction, new event topology discrimination techniques together with delayed coincidence cuts are under development to

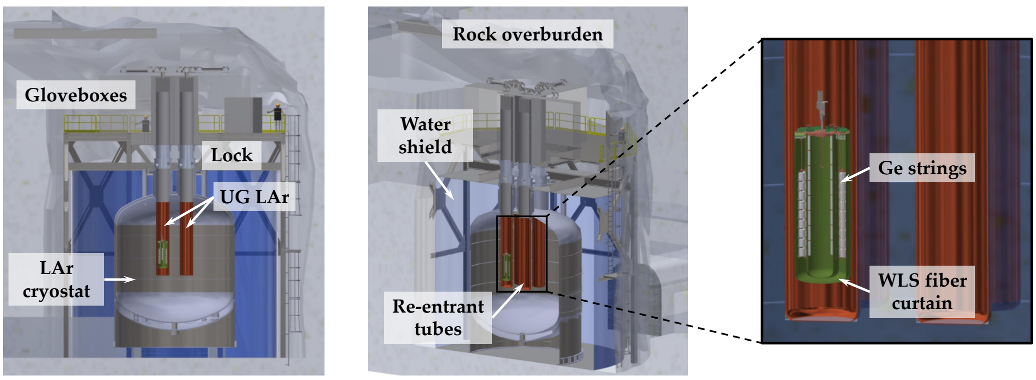

Figure 2.24: Artistic view of the LEGEND-1000 setup with the detector strings installled in several re-entrant tubes made from ultra-pure electroformed copper. Each tube is filled with underground liquid argon while the cryostat itself is filled with normal LAr. Figures provided by M. Busch.

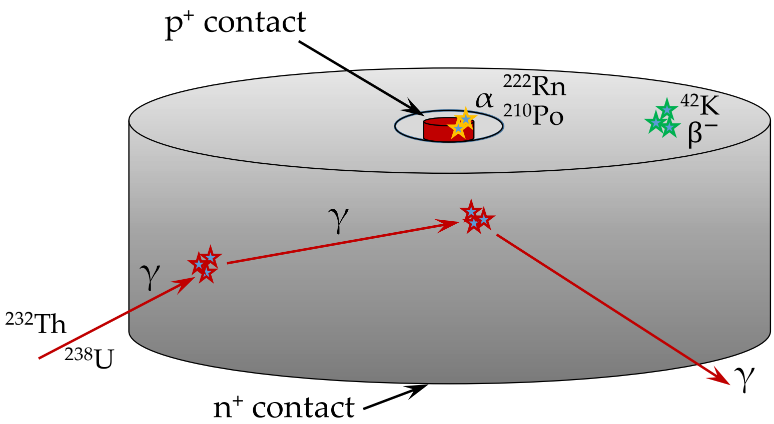

Figure 2.25: Typical radioactive backgrounds inside a ^{76}Ge HPGe detector. While gamma events typically take place at multiple locations due to the Compton scattering, alpha and beta events can only penetrate the surface.

suppress $^{77(m)}$Ge as the main in-situ cosmogenic background contributor [80]. Another important step towards LEGEND-1000 is the development of new readout electronics based on the use of custom-designed application-specific integrated circuit (ASIC) technology to integrate the entire charge sensitive amplifier (CSA) into a single chip. This would allow to get access to an excellent spectral and noise performance and probably further reduce backgrounds coming from the readout electronics by the reduction of sheer mass near to the detectors [81]. One of the main objectives of this work was to demonstrate the status of such newly developed ASIC based readout electronics. More details of the signal readout electronics of LEGEND-1000 will be discussed in Chapter 4.

2.4.3 Overview and backgrounds in $0\nu\beta\beta$ decay searches with ^{76}Ge

Figure 2.25 illustrates typical background events appearing inside a detector. Radioactive decays and their decay chains are one of the main background sources since small amounts of the isotopes can be contained inside detector near material and nearby components. ^{238}U and ^{232}Th can have gamma backgrounds with $E_\gamma > 2\,\mathrm{MeV}$ where at the $Q_{\beta\beta}$-value ^{208}Tl and ^{214}Bi lead to contributions with energy deposits in the signal ROI. Surface alpha events can arise from surface contaminations with ^{222}Rn and ^{210}Po. On the other hand, surface beta events from the long-lived isotopes ^{42}Ar and ^{42}K in the n$^+$ contact cause problems in the $Q_{\beta\beta}$ ROI. In addition, cosmogenic activation trough muons

Table 2.1: Overall background index (BI) for LEGEND-200 and LEGEND-1000 based on Monte Carlo simulations and verified by material screening. While LEGEND-200 wants to improve by a factor of two compared to GERDA, LEGEND-1000 wants to even improve by a factor of 10 [63].

	LEGEND-200	LEGEND-1000	Units
BI <	2×10^{-4}	1×10^{-5}	$\mathrm{cts\,keV^{-1}\,kg^{-1}\,yr^{-1}}$
BI <	0.6	0.03	$\mathrm{cts\,FWHM^{-1}\,t^{-1}\,yr^{-1}}$

creates ^{68}Ge and ^{60}Co which also produce beta and gamma backgrounds in the ROI and can furthermore produce low- and high-energy neutrons by hitting the rocks which causes de-excitation and capture reactions.
The anticipated backgrounds for the two LEGEND stages are illustrated in Figure 2.26. The overall background index (BI) for both experiments is shown in Table 2.1. With experiment running times of five years for LEGEND-200 and ten years for LEGEND-1000, this BI would allow to achieve the target decay half-life of $T^{0\nu}_{1/2} > 10^{27}$ yr for LEGEND-200 and $T^{0\nu}_{1/2} > 10^{28}$ yr for LEGEND-1000 as illustrated in Figure 2.27. To deal with these various backgrounds, background rejection strategies are applied in LEGEND which are illustrated in 2.28. Here, muon events can be rejected by the dedicated muon veto based on Cherenkov light in water which can be read out by photo-multiplier tubes. In addition, the LAr veto system also detects scintilation light from muon events which is read out by optical fibers. The detector holders are made out of PEN which scintilates as active material light which can also be read out with the LAr veto system. Furthermore, detector anti-coincidence cuts can reject MSE in several detectors. In addition, the so-called Pulse Shape Discrimination (PSD) is used to reject Compton scattered MSE inside one detector as well as surface events coming from the radioactive impurities as described above. Figure 2.29a and 2.29b show typical waveforms of the charge and current signal of a SSE and MSE event. While the total energy E of both events is the same, the charge current shows topological differences which can be used to discriminate between the events and reject MSE events since the signal of $0\nu\beta\beta$ decay is a SSE event with energy deposition within a $\sim 1\,\mathrm{mm}^3$ volume.
In the analysis, this can be fulfilled by the ratio A/E of the maximum amplitude of the current A and the amplitude of the charge pulse E (energy). In a typical calibration run, ^{228}Th is often used as calibration source which has a FEP at 2614.5 keV, a SEP at 2103.5 keV and a DEP at 1592.5 keV. In the analysis, the A/E is then tuned such that 90% of the SSEs (signal like events) in this DEP survive while the SEP and FEP can be used to determine the surrival efficiencies in the Compton continuum. This leads to a surrival band of SSEs

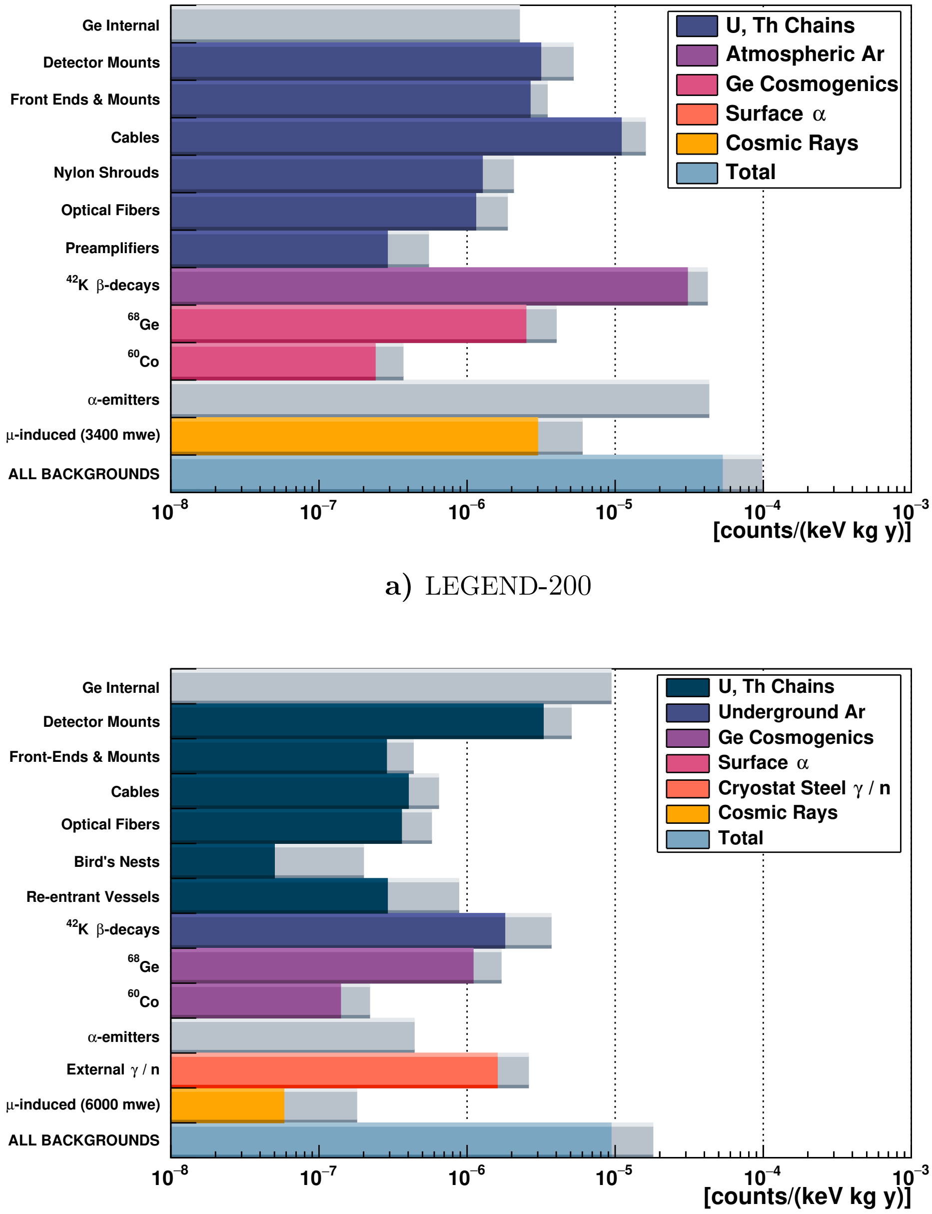

a) LEGEND-200

b) LEGEND-1000

Figure 2.26: Anticipated backgrounds in LEGEND-200 in 2.26a and LEGEND-1000 in 2.26b. Colored bars provide the estimated background contributions, while grey bars indicate 1σ uncertainties due to uncertainties in the screening measurements and Monte Carlo simulations. For the contributions of U, Th internal to germanium detectors, and for the alpha emitters on detector surfaces, only upper limits are estimated. Plot courtesy of the LEGEND collaboration.

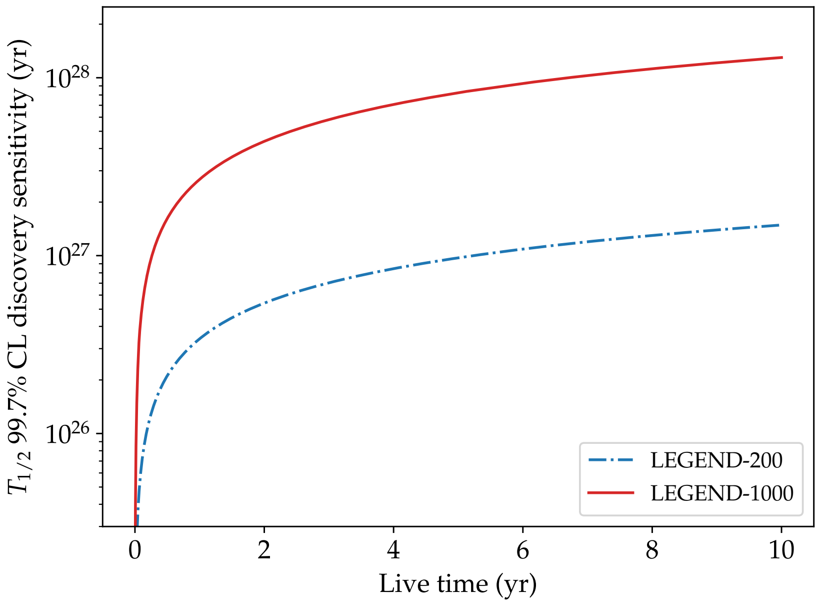

Figure 2.27: Evolution of the signal discovery sensitivity as a function of the experiment running time where the sensitivity is calculated assuming by simple counting analysis and using the inversion of Poissonian probabilites [62]. Figure from [32].

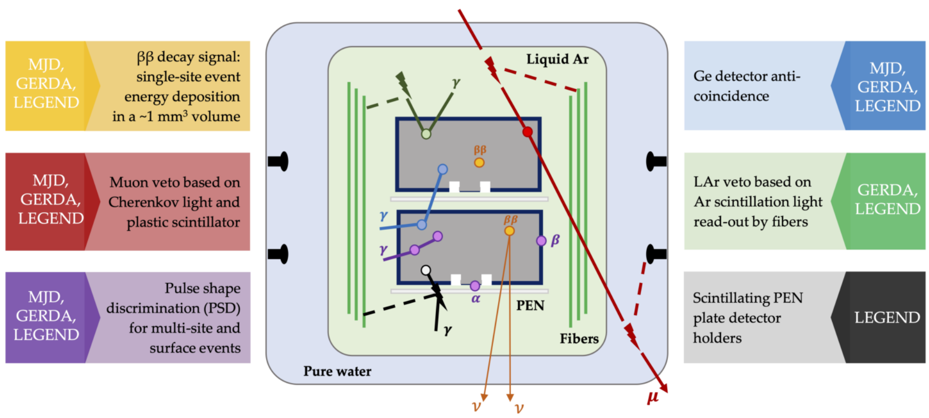

Figure 2.28: Graphical representation of the background reduction strategy of LEGEND. The anticipated backgrounds can be largely rejected by using muon and liquid argon veto systems, as well as scintillating materials, such as detector holders made from PEN. These techniques are supported by analysis methods such as detector anti-coincidence cuts and pulse shape discrimination techniques to reject multi-site events, and alpha and beta surface events. Figure and caption from [82].

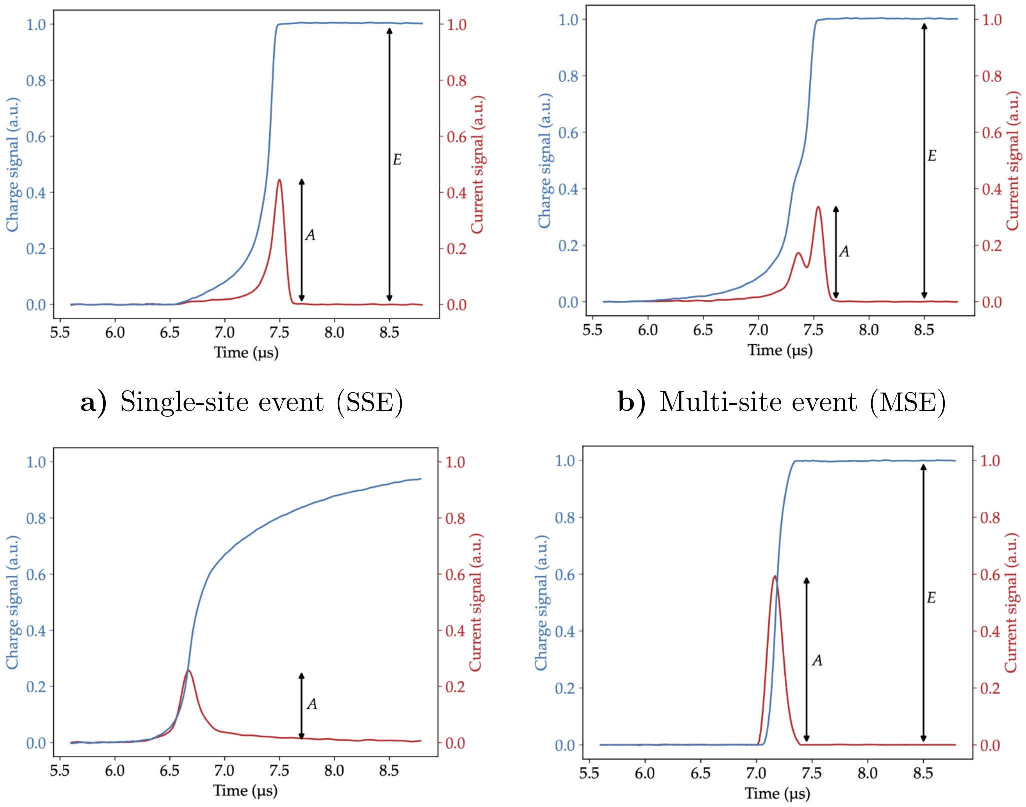

a) Single-site event (SSE) **b)** Multi-site event (MSE)

c) n^+ surface event **d)** p^+ event

Figure 2.29: Charge and current signal of a single-site event in 2.29a, multi-site event in 2.29b, n^+ surface event in 2.29c and p^+ event in 2.29c

in the A/E distribution which is shown in Figure 2.30. In addition, also n^+ surface events as well as events close to the p^+ signal readout contact show topology differences in the charge and current signal as illustrated in Figures 2.29c and 2.29d. By using the same quantitive discriminator, cuts on these events can be set, which is described in detail in [32].

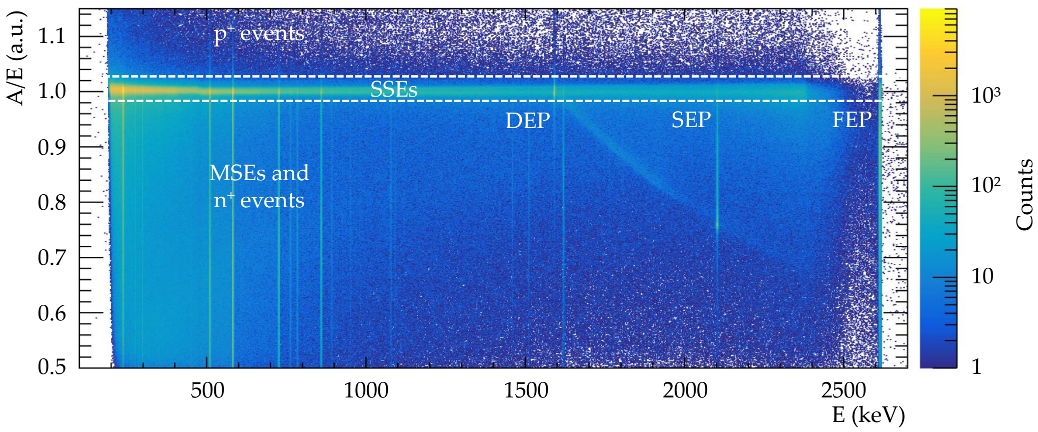

Figure 2.30: Normalized A/E distribution for a ^{228}Th calibration run as a function of energy with the SSE band located around $A/E = 1$. MSEs and n^+ surface events have $A/E < 1$ while events close to the p^+ contact have $A/E > 1$.

Chapter 3

Characterization of Signal Readout Electronics for LEGEND-200

One of the main objectives of this work was the characterization and analysis of the novel HPGe detector readout electronics in LEGEND-200 at LNGS. To this end, different test configurations have been set up in July and October 2021 in the LEGEND-200 clean room at LNGS to test the performance of all components. A special focus was set on the noise performance. First, the signal readout architecture in LEGEND-200 at LNGS is described in its different stages in Section 3.3 with focus on charge sensitive amplifier where Section 3.2 gives a general overview about electronic noise in readout systems. Following, the different tests and their corresponding results are shown in Section 3.4.

3.1 Signal readout architecture in high-purity germanium detectors

A typical readout chain for HPGe detectors is shown in Figure 3.1. The detector operated as a diode is biased with the HV as reverse bias voltage and acts electronically as capacitor C_D in the circuit. When energy is deposited in the detector bulk, the charge signal is proportional to the energy deposited. The signal is then integrated by the charge sensitive amplifier (CSA), and a voltage signal is released as output. The voltage signal can then be processed by a DAQ system to digitize the signal before enabling further offline digital signal processing (DSP) to extract energy information etc. In ^{76}Ge-based $0\nu\beta\beta$ decay searches, the detector and the CSA are typically operated at cryogenic temperatures such as e.g. 87.2 K for LAr. Since DSP enables the possibility for offline analysis, PSD techniques can easily be applied, and a number of

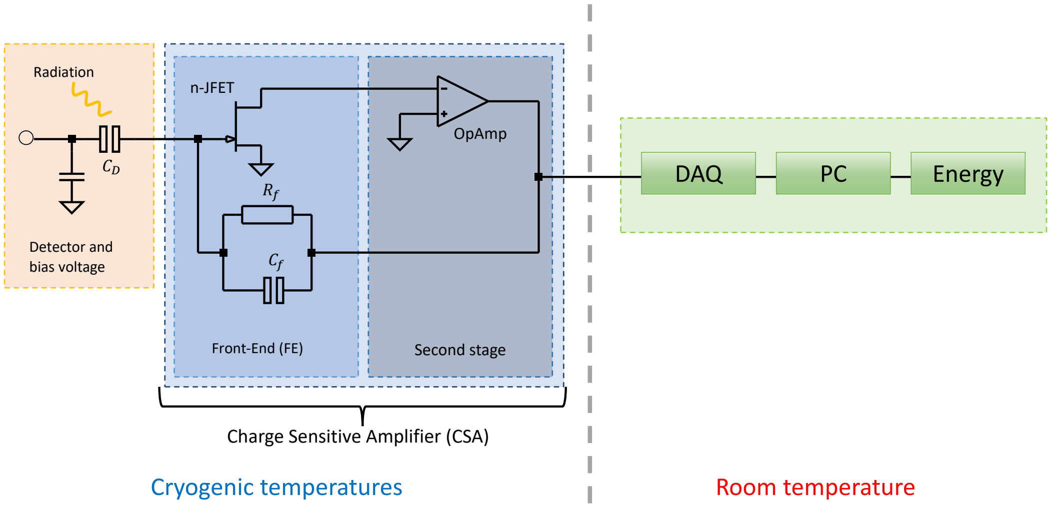

Figure 3.1: Example of a readout chain for HPGe detectors where the detector with its bias voltage is followed by the charge sensitive amplifier which integrates the charge and outputs a voltage signal which is then send to a data aquisition system which digitizes the signals before enabling the further digital signal processing with the energy reconstruction etc. Plot idea from [32].

different shaping filters can be used to increase resolution and effectively reject radioactive backgrounds.

3.1.1 Charge sensitive amplifier (CSA)

In a typical event from HPGe detectors, an energy deposition of 1 MeV in germanium corresponds to 3.38×10^5 electron-hole pairs which creates a charge of $Q_S \approx 55\,\mathrm{fC}$ with a signal collection time of $\mathcal{O}(100\,\mathrm{ns})$ why the signal can be modelled as a short delta-like current pulse I_S. Since the physical quantity of interest is the deposited energy, this short current pulse has to be integrated to extract the energy E

$$E \propto Q_S = \int I_S(t)dt \tag{3.1}$$

In HPGe detector systems, the main purpose of a CSA is to perform this integration while returning a voltage output signal in a range which is amplified so that it can be processed by the DAQ. A configuration of the most simple CSA can be found in Figure 3.2. It consists of a feedback capacitor C_f in parallel with an inverted operational amplifier (OpAmp) with gain $-A$, which is commonly known as an integrator. If a current pulse enters the CSA, also a

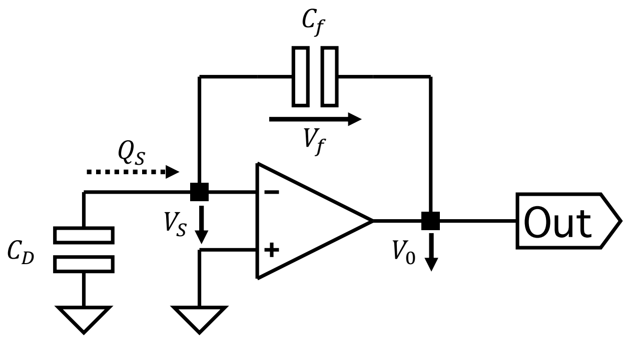

Figure 3.2: Basic configuration of a charge sensitive amplifier where a feedback capacitor C_f is in parallel with an inverted operational amplifier with gain $-A$. The input signal is modelled as a delta-like current pulse. Figure idea from [83].

voltage pulse is generated according to the general capacitor equation

$$V_S = \frac{Q_S}{C_D + C_i} \tag{3.2}$$

with C_D the detector capacitance and C_i the total input capacitance of the CSA. Following, this voltage is then amplified by the gain $-A$ of the OpAmp to $V_O = -A \cdot V_S$. By applying Kirchhoff's second law via the closed-loop going from the left node over the capacitor to the second node on the right closing via ground as illustrated in Figure 3.2, one can derive

$$V_S = V_f + V_O \quad \text{and} \quad V_O = -A \cdot V_S \tag{3.3}$$

$$\Rightarrow V_f = (A+1) \cdot V_S \tag{3.4}$$

An ideal OpAmp has infinite input impedance so that no current flows into the amplifier. Therefore, all input charge Q_S is flowing onto the feedback capacity C_f leading to

$$Q_S \ (= Q_f) = C_f \cdot V_f \overset{3.4}{=\!=} C_f \cdot (A+1) \cdot V_S \tag{3.5}$$

$$\Rightarrow V_O = \frac{-A}{C_f \cdot (A+1)} Q_S \overset{A \gg 1}{\approx} \frac{-Q_S}{C_f} \tag{3.6}$$

As seen in Equation 3.6 for the simple example of a CSA, the output voltage V_O of the circuit is directly proportional to the signal charge Q_S coming from the detector system. Furthermore, it shows that on the one hand, the feedback capacity C_f should be small to achieve large output signals, but on the other hand not too small to map the desired dynamic range of the detector system to

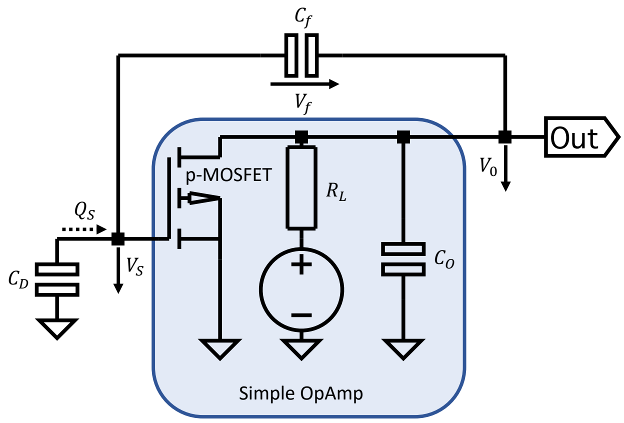

Figure 3.3: Basic configuration of a charge sensitive amplifier with a real OpAmp. The OpAmp consists of a p-metal–oxide–semiconductor field-effect transistor (MOSFET) with transconductance g_m, a load resistance R_L and a output capacitance C_O. Plot idea from [83].

output signals with $\mathcal{O}(1\,\mathrm{V})$ so that they can be processed by the flash analog to digital converter (FADC) in the DAQ which typically favours $C_f = \mathcal{O}(100\,\mathrm{fF})$. In real circuits, OpAmps do not act as a infinite fast device with no current flowing into itself. The time response of a real CSA is not instantaneously, but rather often times much slower than the signal itself. This time response affects the measured pulse shape. Figure 3.3 shows a schematic of a simple real CSA. The OpAmp consists here of a p-MOSFET with transconductance g_m, a load resistance R_L and a output capacitance C_O. Since the output current changes as the input voltage varies, the voltage gain of the OpAmp can be calculated to [83]

$$A_V = g_m \cdot Z_L \quad \text{with} \quad \frac{1}{Z_L} = \frac{1}{R_L} + i\omega C_O \tag{3.7}$$

$$\Rightarrow A_V = \frac{g_m}{\frac{1}{R_L} + i\omega C_O} \tag{3.8}$$

with Z_L the load impedance, ω the frequency and i the imaginary unit. The load impedance Z_L is the parallel combination of the total load resistor R_L and the total load capacitor C_O (c.f. Figure 3.3) where the latter one is unaviodable since every real gain device has an output capacitance, following stages have input capacitances and other components in the circuit introduce stray capacitances which all contribute to the total load capacity C_O [83]. Equation 3.8 states that at low frquencies ω, the amplifier has a constant gain $A_V = g_m \cdot R_L$. However, at higher frequencies the gains drops off linearly. This is

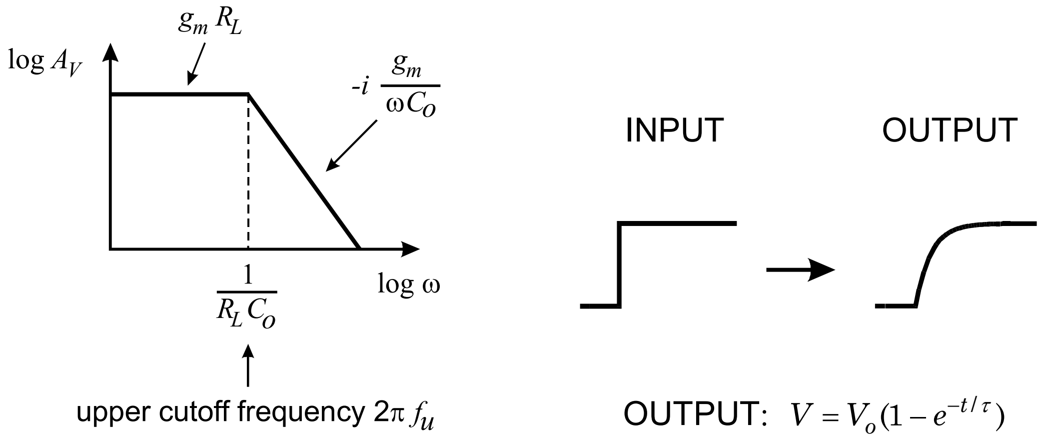

a) Frequency response **b)** Pulse response

Figure 3.4: Frequency and pulse response of a real amplifier. While at low frequencies the gain is constant with $A_V = g_m \cdot R_L$, it drops linearly with a 90° phase shift. This translates also in pulse response where the shape of the input pulse is changed. Figures from [83]

illustrated in Figure 3.4a together with the cutoff frequency $f_U = 1/(R_L C_O)$ at which the asymptotic low and high frequency responses intersect [83]. Moreover, the frequency response also translates into a time response which disturbs the shape of the input signal as illustrated in Figure 3.4b. because a voltage step from the detector must first charge up the output capacity [83].
In practical applications, CSA often use multiple stages all of which contribute to a overall frequency response. As seen in Figure 3.1, the CSA here consists of a junction-gate field-effect transistor (JFET) as first stage followed by a commercial OpAmp stage. Since the JFET cancels out the slow loading of the high output capacity of the OpAmp by acting as a current source for the following section, this allows to generate higher cutoff frequencies and therefore the possibility to process faster signals whithout disturbing the signal shape which is very important for the application of PSD techniques. In addition, the signal-to-noise ratio of a CSA is mainly determined by the first component closest to the detector as explained in Section 3.2. Because JFETs have much slower electronic noise then, for example, commercial OpAmps, this gives another advantage of the layout with a JFET in the first stage.
If now a readout chain of this layout is used inside a HPGe detector radiation application, one major problem still remains: if several events deposit their energy in the detector and the corresponding charge is measured with the CSA, the feedback capacity C_f is loaded with more and more charge until it

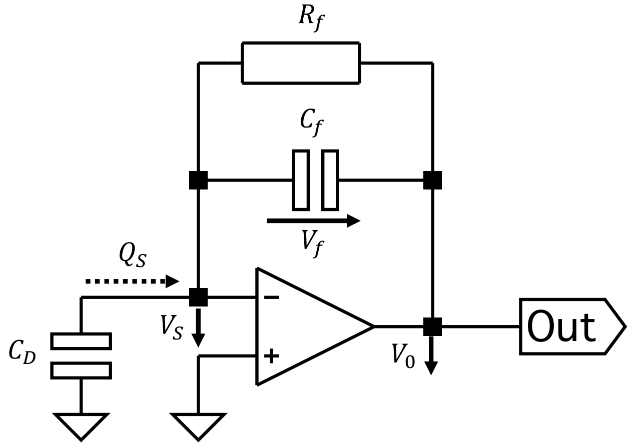

Figure 3.5: Charge sensitive amplifier with feedback resistor: since the readout of multiple events loads the capacity until it saturates, the resistor enables the constant drain off the charge from the resistor.

saturates when the OpAmp reaches its maximum output voltage. To avoid this behavior, the charge has to drain off the capacitor. This can be achieved by a feedback resistor R_f in parallel to the feedback capacity over which the charge can constantly drain off, as shown in Figure 3.5. This leads to an output pulse shape with an exponentially decaying tail with a decay time $\tau = R_f \cdot C_f$. Since the resistor and the capacitor values do not change during measurement campaigns, every output waveform of every event shows the same decay tail independent of the energy deposited.

3.1.2 Requirements for $0\nu\beta\beta$ decay experiments

Since $0\nu\beta\beta$ experiments are low background experiments, the electronic readout chain has to fulfill special requirements. At first glance, the CSA should be placed as close as possible to the detectors because this reduces the capacity load due to reduced cable length and the pick-up noise and is crucial to keep the electronic noise low (c.f. Section 3.2 for electronic noise). Another advantage is the extended bandwidth of the system, which enables faster signal rise times and therefore the application of PSD techniques as explained in the previous section. On the other hand, reducing the material load near the detector is crucial because this highly increases the background contribution coming from the readout system. Furthermore, the used materials must be ultra-radiopure and screened to measure the activity. Therefore, a compromise between these two requirements has to be found for every experiment. In addition, the CSA must be capable of driving differential signals over a length of $\mathcal{O}(10\,\mathrm{m})$ in order to get signals out of the cryostat to the DAQ system without using too much power since this could lead to bubble formation in the LAr due to local boiling which enacts microphonic noise. Moreover, the CSAs have to work with a lot of different detector types and capacities with high reliability during many cooling cycles and to be robust against electrostatic discharges when connecting it to the detector.

3.2 Electronic noise in readout systems

Electronic noise describes an unwanted disturbance in a electronic signal e.g. by random fluctuations of the charge carrier. It is generated by electronic devices through several different effects. Concerning readout electronics, electronic noise impairs the signal integrity by degradation of the signal and leads to worse resolution. To compare the performance of charge sensitive amplifiers, the total noise is commonly expressed as the root mean square (RMS) voltage of the signal baseline which is typically Gaussian distributed due to the randomness. If n electrons move with velocity v through a sample between two electrodes, a current is induced which depends on the spacing l of the electrodes (Ramo's theorem [69]) with the fluctuation of this current given by the total differential

$$i = \frac{nev}{l} \tag{3.9}$$

$$\langle \mathrm{d}i \rangle^2 = \left(\frac{ne}{l} \langle \partial v \rangle \right)^2 + \left(\frac{ev}{l} \langle \partial n \rangle \right)^2 \tag{3.10}$$

where the two terms add quadratically as they are statistically uncorrelated [83]. Following this equation, one can see that the total noise consists of two mechanisms:

1. **Thermal noise**: Random fluctuations of the charge carrier velocities v because of their thermal motion

2. **1/f noise and shot noise**: Random fluctuations of the charge carrier number n

3.2.1 Noise sources

Thermal noise (also called Johnson or Nyquist noise) is produced by random fluctuations of free charge carriers (Brownian motion) and is intrinsic to all conductors and resistors why it is one of the main sources of noise in detector electronics. At frequencies $\lesssim 300\,\mathrm{GHz}$ (microwave), thermal noise is Gaussian and can be described by the Rayleigh-Jeans approximation [84]

$$\frac{\mathrm{d}P_n}{\mathrm{d}f} = 4k_\mathrm{B}T \qquad \text{spectral noise density} \tag{3.11}$$

$$P = \frac{V^2}{R} \qquad \text{power in a resistance} \tag{3.12}$$

$$\Rightarrow \frac{\mathrm{d}V_n^2}{\mathrm{d}f} \equiv e_n^2 = 4k_\mathrm{B}TR \qquad \text{spectral voltage noise density} \tag{3.13}$$

with T the absolute temperature, R the resistance and k_B the Boltzmann constant. The spectral noise density in Equation depends on the range of frequencies the system is sensitive to, the so-called bandwidth B_f such that the RMS noise fluctuations in terms of volts is obtained by

$$V_{RMS}^2 = \int_0^\infty e_n^2 A^2(f) df = e_n^2 \cdot B_f \text{ for } {}^{A(f)=const}_{\text{with } f \in B_f} \tag{3.14}$$

$$\rightarrow V_{RMS} = \sqrt{4 k_\mathrm{B} T R B_f} \tag{3.15}$$

where the $A(f)$ is the frequency-dependent gain of the amplifier. Equation 3.15 shows that thermal noise is independent of the frequency why it is called white noise, and that it increases with the square root of the bandwidth B_f of the amplifier and the square root of the temperature why it can be reduced by reducing the bandwidth or the system operating temperature [84]. Furthermore, if the gain of the amplifier $A(f)$ is actually frequency-dependent, this can also lead to higher thermal noise.

1/f noise or pink noise is caused by the slow fluctuations of properties of condensed-matter materials of devices like e.g. the fluctuations of defects or traps in e.g. semiconductors. It has a 1/f dependency described by

$$P_n(f) \propto \frac{1}{f^\alpha} \tag{3.16}$$

with α typically being around one [84]. Pink noise undergoes a corner frequency at which it becomes comparable to white noise in the system [84].

Shot noise occurs when charge carriers randomly penetrate a sample volume in statistical indepent processes like e.g. the current flow in a semiconductor diode via emission over a barrier [84]. The spectral noise current density for bandwidth B_f can be written as [84]

$$\frac{\mathrm{d}I_n^2}{\mathrm{d}f} \equiv i_n^2 = 2eI \qquad \text{spectral noise current density} \tag{3.17}$$

$$I_{RMS}^2 = \int_0^\infty i_n^2 A^2(f) df = i_n^2 \cdot B_f \qquad \text{for } {}^{A(f)=const}_{\text{with } f \in B_f} \tag{3.18}$$

$$\rightarrow I_{RMS} = \sqrt{2eIB_f} \tag{3.19}$$

with I the DC current. Since in ohmic conductors like resistors the number of available charge carriers is not limited, the fields caused by local fluctuations in the charge density are equalized by additional carriers wherefore no shot noise exists [84]. As well as for thermal noise, the shot noise is white noise and can become dominant at small currents since it is dependent on the square root of the current I.

Electromagnetic interference (EMI) can be another source of noise where external sources can introduce EMI that is picked up by the cables and circuit components if they act like antennas [85]. Examples of EMI are the 50 Hz mainline noise and its harmonics (100 Hz, 150 Hz etc.), noise from modern rapid switching AC-DC power supplies or noise coming from programmable logic controller (PLC) systems which can operate different types of machines, robotics or different types of motors in setups.

3.2.2 Mathematical formalism

Since CSA readout electronics in semiconductor detector measure signal charge, it is common to express the noise in terms of equivalent noise charge (ENC) which corresponds to the charge that is needed at the input of the CSA to have a signal-to-noise ratio of one. Therefore, the ENC noise is measured in number of electrons e^-. In general, real CSA circuits contain different stages with different components which can all contribute to the total noise. In a CSA configuration consisting of two stages 1 and 2 with amplification A_1 and A_2 and corresponding noise N_1 and N_2, a signal S leads to a reduced signal-to-noise ratio of [84]

$$\left(\frac{S}{N}\right)^2 = \left(\frac{S}{N_1}\right)^2 \frac{1}{1 + (\frac{N_2}{A_1 N_1})^2} \tag{3.20}$$

This Equation shows that the signal-to-noise ratio is mainly driven by the first gain stage which is closest to the detector as long as the gain of the first stage is high enough and the noise of the second stage not too high wherefore noise calculations only take this stage into consideration.
The ENC noise in a HPGe detector readout system with CSA is illustrated in Figure 3.6 where it is represented by a ideal noiseless amplifier with gain A, a series voltage generator s with series resistance R_s, a parallel current generator p with parallel resistance R_p and a series current generator $1/f$. The input to the CSA is modelled by the detector capacitance C_D and the corresponding signal $Q\delta(t)$ represented by a delta-like charge signal. The ENC noise is then composed of three uncorrelated terms which conclude with the three noise

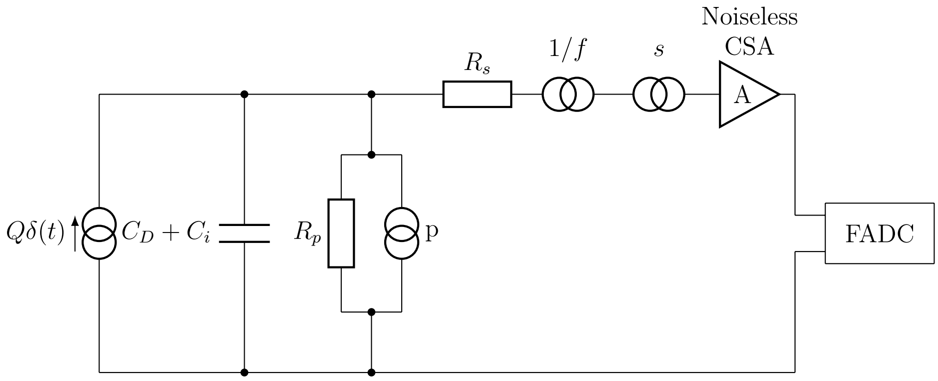

Figure 3.6: Signal and noise sources in the readout system of a HPGe detector with a CSA where the output signal is transmitted to the FADC. The input to the CSA is modelled by the detector capacitance C_D and the corresponding signal $Q\delta(t)$ represented by a delta-like charge signal. In the following, the CSA consists of a noiseless amplifier with gain A, a series voltage generator s with series resistance R_s, a parallel current generator p with parallel resistance R_p and a series current generator $1/f$. Plot idea from [32, 88].

sources described in Section 3.2.1 [86, 87]

$$\mathrm{ENC}^2 = \underbrace{\alpha \frac{1}{\tau_s} \frac{2k_\mathrm{B}T}{g_m} C_{tot}^2}_{\text{series: ENC}_p^2} + \underbrace{\beta A_f C_{tot}^2}_{\text{1/f: ENC}_s^2} + \underbrace{\gamma \left(eI_{tot} + \frac{k_\mathrm{B}T}{R_F} \right) \tau_s}_{\text{parallel: ENC}_{1/f}^2} \tag{3.21}$$

with $C_{tot} = C_{det} + C_F + C_i$ the total capacitance consisting of detector C_{det}, feedback C_F and CSA input capacitance C_i, R_F the feedback resistor, $I_{tot} = I_{det} + I_{gate}$ the total current consisting of the detector leakage current I_{det} and the gate current I_{gate} of the JFET, g_m the transconductance of the JFET, k_B the Boltzmann constant and T the operating temperature which is 87.3 K in LAr. The constants α, β and γ are related to the signal shaping filter with the shaping time τ_s and has values for an example of a Gaussian shaper of $\alpha = 0.89$, $\beta = 1$ and $\gamma = 1.77$ [87].

The **series noise** in Equation 3.21 is dominantly driven by the shot noise of the JFET because the JFET is the first stage in the CSA closest to the detector as explained above. It is proportional to the operating temperature T wherefore it benefits from the LAr operating temperature and to the squared total capacitance which is dominated by the detector capacitance wherefore detectors with low capacitances are preferred [87]. Furthermore, a JFET with a high transconductance g_m can further reduce the noise by the trade-off

of an increasing input capacitance C_i of the CSA [83]. Assuming a shaping time of $\tau_s = 10\,\mu s$, detector capacitance of $C_{det} \sim 1\,pF$ (typical for BEGe detectors) and CSA input capacitance of $C_i = 10\,pF$, the series noise has values of $ENC_s \sim 10\,e^-$.
The **1/f noise** in Equation 3.21 is mainly composed of the 1/f noise of the JFET where the amplitdue A_f depends on the dielectric properties and the fabrication process of the JFET why the sophisticated selection of a suitable JFET is also crucial for the noise [89]. The 1/f noise also scales with the squared total capacitance wherefore it also benefits from low capacity detectors, but is in general subdominant [32].
The **parallel noise** is dominantly produced by the total current I_{tot} of the system which is dominated by the leakage current I_{det} and the thermal noise of the feedback resistor R_F as largest resistance [87]. The parallel noise also benefits from lowering operating temperature as well as from low detector leakage current I_{det}. Additionally, a high feedback resistance R_F can further reduce noise. However, too high R_F values would also lead to longer signal decay times which sustains pile-up. In typical CSA applications, a compromise between these two considerations has to be found.
In addtion, Equation 3.21 shows that the parallel noise is proportional to the shaping time $ENC_p^2 \propto \tau_s$ while the series noise is inverse proportional to the shaping time $ENC_s^2 \propto \tau_s$ and 1/f does not depend at all from the shaping time. Figure 3.7 shows the total ENC noise as function of the shaping time τ_s for a typical readout system. The figure illustrates that the noise curve shows a minimum at which the total ENC noise is minimal, the so-called *optimal shaping time*. This minimum always exists independently of the chosen shaping filter [88].

3.2.3 Energy resolution

The energy resolution of a HPGe detector system is composed of three statistically uncorrelated terms: the ENC noise, the statistical fluctuations in the charge production process, the so-called Fano limit and the efficieny of the charge collection process in the crystal and the electronic system

$$w_{det}^2 = w_{\mathrm{ENC}}^2 + w_{stat}^2 + w_{col}^2 \tag{3.22}$$

The contribution of the ENC noise to the resolution is constant in terms of energy and given by [90]

$$w_{\mathrm{ENC}} = \frac{\eta}{e} \cdot \mathrm{ENC} \tag{3.23}$$

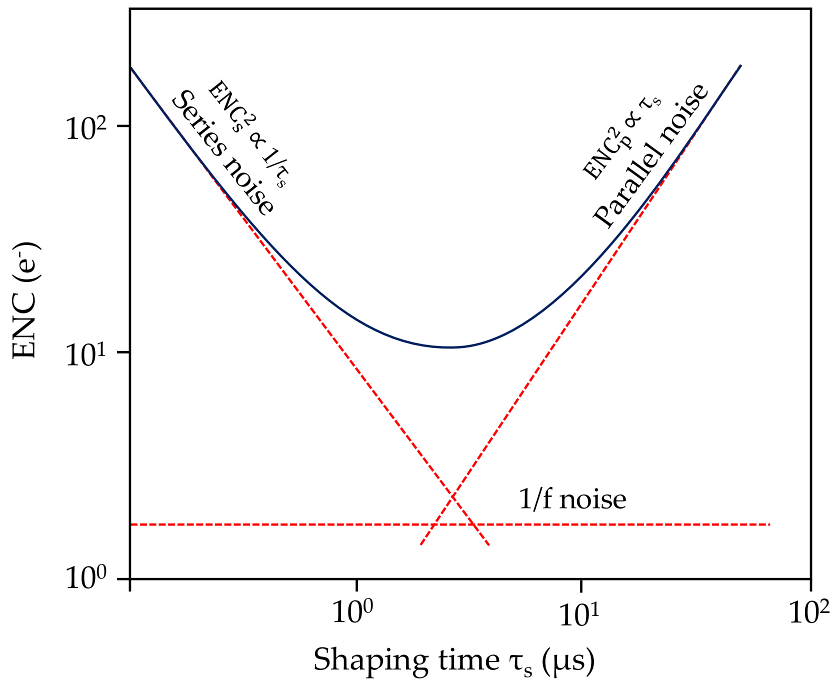

Figure 3.7: Example of a noise curve showing the three components of the ENC noise and their dependency from the shaping time τ_s. Plot from [32]

with the ENC noise coming from Equation 3.21 and η the average energy to create a electron-hole pair which is $\eta = 2.96\,\mathrm{eV}$ in ^{76}Ge so that the term η/e refers to the voltage produced at the readout of the detector per charge e which was measured inside the bulk.
The second contribution to the resolution comes from the statistical fluctuations in the charge production process. Assuming Poissonian statistics, the average number $\langle N \rangle$ of electron-hole pairs produced in a energy deposition with energy E and the corresponding uncertainty can be written as [90]

$$\langle N \rangle = \frac{E}{\eta} \tag{3.24}$$

$$\sigma_{\langle N \rangle} = \sqrt{\frac{E}{\eta}} \tag{3.25}$$

$$\Rightarrow \sigma_E = \eta \cdot \sigma_{\langle N \rangle} = \sqrt{\eta E} \tag{3.26}$$

where Equation 3.26 shows the following statistical uncertainty of the energy due to this fluctuations. In reality, this calculated uncertainty is not measured because the Poissonian assumption of this process is not fully true [91]. Therefore, the Fano factor $F < 1$ corrects for this behaviour given the correct contribution to the resolution as [91]

$$w_{stat} = \sqrt{F \cdot \eta E} \tag{3.27}$$

This Fano factor has been measured for germanium along the years where recent publications favour values of $F \sim 0.11$ [92–95].
The third term accounts for the efficiency of the charge collection of the detector and the electronic system. On the one hand, crystal imperfections or the use of not fully depleted detectors can lead to recombinations in the crystal lattice resulting in incomplete charge collection. On the other hand, CSAs with a too short time constant $R_F C_F$ or too short shaping times τ_s in the subsequent shaper can cause sub-optimal charge integration of the deposited charge, resulting in worse resolution. In all cases, the effect is a systematic energy underestimation inducing the presence of low-energy tails in the spectral lines [90]. Because of the complexity of the physics involved, this contribution is normally expressed by the empirical formula [90]

$$w_{col} = c \cdot E \tag{3.28}$$

where c is a constant.
Summarizing, the total energy resolution can be written as

$$w_{det} = \sqrt{\frac{\eta^2}{e^2}\mathrm{ENC}^2 + \eta F \cdot E + c^2 \cdot E^2} \tag{3.29}$$

$$\Rightarrow \mathrm{FWHM}(E) = 2\sqrt{2\log(2)}\sqrt{\frac{\eta^2}{e^2}\mathrm{ENC}^2 + \eta F \cdot E + c^2 \cdot E^2} \tag{3.30}$$

with FWHM being the full width at half maximum (FWHM) for a spectral energy peak at energy E. At lower energies, the ENC noise dominates while the others take over at higher energies. In general, the maximum resolution can be achieved by ultra-low ENC noise and perfect charge collection efficieny (resulting in low c) which would then limit the resolution only by the Fano limit of the crystal.

3.3 Signal readout system in LEGEND-200

In LEGEND-200, a novel readout system based on previous implementations by GERDA and MJD is used which is shown in Figure 3.8.

Here, the CSA consists of two stages called LMFE and CC4. The latter drives the signal over differential lines outside the cryostat to the so-called HEs, which are located at the flange of the cryostat lock to the cleanroom above. There, the signal is transported to the DAQ system called `FlashCam`. The HV system consists of a filter card also mounted at cryostat flange connected with the HV crate outside. In addition, a pulser line can pass differential pulses directly to the CC4, which transfers them single-ended to the LMFE. In the following sections, a more detailed prescription of the functionalities is given.

3.3.1 LEGEND-200 charge sensitive amplifier (CSA)

The CSA in LEGEND-200 consists of two stages where the very front end called LMFE contains the JFET, the feedback resistor R_f and feedback capacity C_f and a additional pulser line with pulser capacity C_P as shown in Figure 3.9.

The JFET is realized by a commercially available in-die three-terminal MOXTEK MX11 n-channel ultra-low noise JFET with low input capacitance $C_{GS} = 2.6\,\text{pF}$ and a transconductance $g_m = 10\,\text{mSv}$ at $110\,\text{K}$ [96]. The high transconductance and low input capacitance make it perfect suitable for low-noise detector applications since they reduce electronic noise (c.f. Equation 3.21). The whole LMFE is made on a Suprasil substrate with sputtered traces patterned via photolithography and chemical wet etching while the pulser capacity $C_f \approx 400\,\text{fF}$ and the pulser capacity $C_P \approx 100\,\text{fF}$ are realized by stray capacitances between the traces. The feedback resistor is sputtered to a thin film of amorphous germanium (aGe) with a resistance of $R_f \approx 1\,\text{G}\Omega$ at LAr temperature and $R_f \approx 600\,\text{k}\Omega$ at room temperature. All pads are connected by Al(1%Si) wire bonds and the whole LMFE is mounted in a low-mass frame made from PEI.
Following, the LMFE is connected to the second stage called CC4 via Axon pico-coaxial signal cables with length of $\sim 1\,\text{m} - 1.5\,\text{m}$. A photograph of the CC4 is shown in Figure 3.10

The second stage contains the OpAmp (LMH6654) produced by small-footprint surface-mount device (SMD) parts on a low-mass Kapton board. The separation of the two stages enables the possibility to use less radiopure commercial OpAmp at a position with less stringent radiopure requirements containing very good noise performance. To reduce the amount of material at the location of the CC4, seven channels are each summarized in one single CC4 circuit board. At the end of the CC4, signals are driven differentially via a 10 m long Kapton

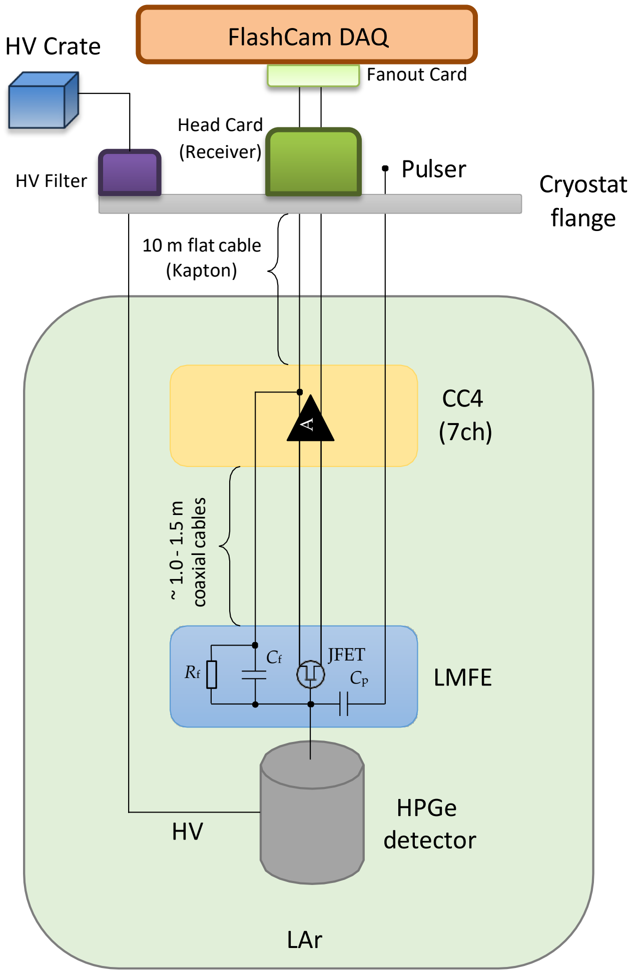

Figure 3.8: Readout scheme of LEGEND-200: while the HPGe detector and the CSA consisting of the low-mass front-end (LMFE) and the CC4 are operated in the LAr, the signals are received at the cryostat flange by the head electronics (HE) which transmits them via the fanout board to the `FlashCam` DAQ system. The HV system consists of a filter card also located at cryostat flange connected with the HV crate outside. Figure idea from [32].

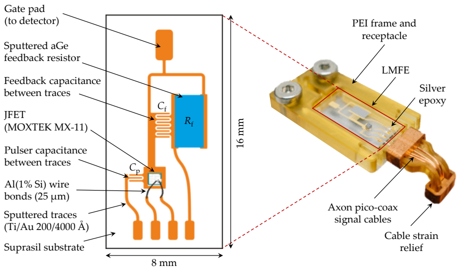

a) Layout and photograph of the custom-designed LEGEND-200 LMFE

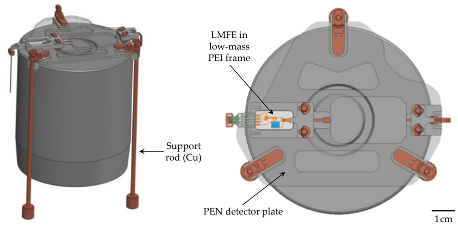

b) Layout of a mounted LMFE on a LEGEND-200 HPGe detector.

Figure 3.9: Layout (left) and mounting (right) of a LMFE in LEGEND-200. It consists of of an MX11 JFET, a feedback resistor R_f , feedback capacitance C_f and a pulser capacitance C_P hosted on a Suprasil substrate which is mounted in a low-mass polyetherimide (PEI) frame. Figure from [32]. The right plot shows a LMFE mounted on the bottom of the detector with a wire bond conection from the Q_{in} gate pad to the p^+ readout contact of the detector. The detector is hold by a PEN plate supported by ultra-pure copper support rods. Rendering provided by M. Busch.

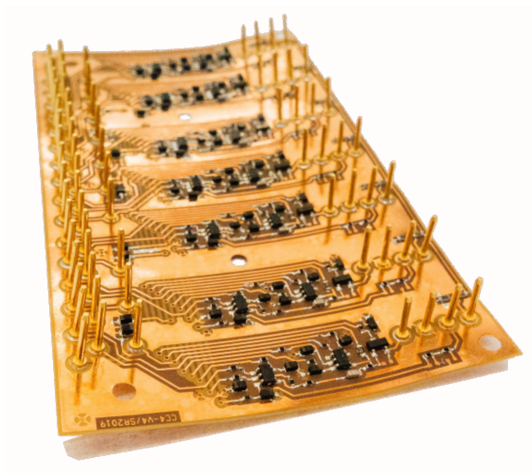

Figure 3.10: Photograph of the CC4 preamplifier consisting of seven identical channels. Detailed information about the CC4 can be found in [97]. Image courtesy of M. Willers.

flat band out to the flange at the top of the lock to the flange going out of the cryostat (c.f. Figure 3.8). The use of differential drivers reduces the common noise, which is electronic noise with the same polarity on both differential lines. The signal with offsets of $\pm 2.7\,\mathrm{V}$ is then received outside the cryostat at the flange from the HE which receives the signals and provides a buffer termination as compensation for the offsets coming from the MX11 JFETs (c.f. Figure 3.11a). The HE is then capable of sending the signal further to the fanout board by providing the common mode of $0.9\,\mathrm{V}$ needed for the `FlashCam` DAQ system (c.f. Figure 3.11c). The `FlashCam` system is a modular DAQ system consisting of four 250 MHz FADCs which can provide 16-bit effective waveforms sampled at 62.5 MHz by combining the four FADCs and downsampling [98]. Since `FlashCam` contains four FADCs each processing each signal, the fanout board is needed which can divide the input signal into four identical signals in terms of height and shape (c.f. Figure 3.11b). The `FlashCam` readout software finally stores the raw waveform data on disk in a propiertary data format while gaining some additional information such as e.g. baseline values by sampling longer baseline values before the trigger event. Furhtermore, `FlashCam` provides the trigger information as well as coincidence and timing information among all 160 channels.

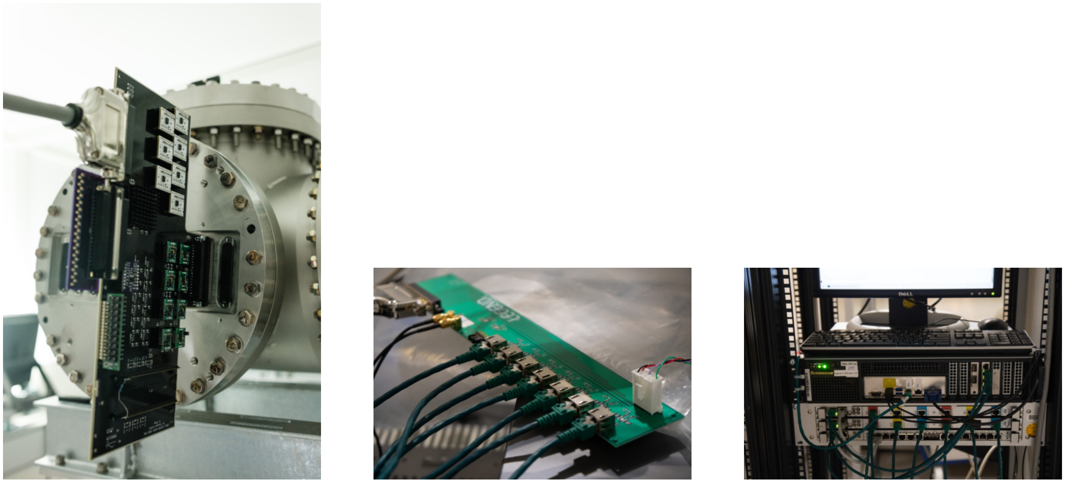

a) Head electronics (HE) **b)** Fanout board **c)** `FlashCam` DAQ system

Figure 3.11: Head electronics (HE) (left), fanout board (middle) and `FlashCam` system (right) in the LEGEND-200 clean room above the cryostat at LNGS during commissioning. The HE is mounted at the cryostat flange containing the buffer boards (small white boards) for all seven channels coming from the CC4. The signals are further transmitted by the grey cable to the fanout board, which splits the input signal into four identical signals in terms of height and shape to be readable by the four FADCs of `FlashCam`. Pictures provided by M. Willers.

3.4 Full chain tests in LEGEND-200

3.4.1 Integration tests

The course of this thesis inlcuded a research stay in July 2021 at LNGS in which a integration testing of the LEGEND-200 electronics was performed. At LNGS, a small setup for integration testing was available including:

- 9 production CC4s in the finalized design
- One 7 channel head electronics system consisting of a single head card and a single fanout board.
- Several dummy front-end (DFE) in a Printed Circuit Board (PCB) version with a feedback capacity of $C_f = 400\,\mathrm{fF}$, feedback resistor of $R_f = 1\,\mathrm{G\Omega}$, a pulser capacitance of $C_P = 100\,\mathrm{fF}$ and commercial BF862 JFET. The DFE used the LMFE instead in the first stage for fast electronics testing with a pulser because the LMFE as an extremely sensitive component of high radiopurity is not suitable for fast and intensive testing of different readout chain configurations due to its difficult handling and the sensitive cabling already attached to every finished LMFE. Figure 3.12 shows 7 DFE connected to a CC4 at the Kapton flat band hanging out of the LEGEND-200 lock. Since the BF862 has different behavior than the MX11 JFET of the LMFE and the feedback resistor is in the value range of the LMFE one at cryogenic temperatures, the output of the readout chain behaves as with a real LMFE.
- Two connector boards with SMA adapters which allow injecting pulses directly into the long Kapton flat band cable and into the head card itself without the need to use the pulser line on the head card itself (c.f.). In LEGEND-200, the fanout board contains a differential pulser input which is fed through the head card over a separate pulser line in the CC4 and LMFE which can be bypassed with the connector board to see the circuit response without the influence of the pulser line itself.
- A arbitrary waveform generator (Keysight 333600A Series) to inject differential pulser signals into the circuits.
- Several power supplies (Keithley 2220-30-1 Dual Channel DC) to generate supply voltages for the head card and the fanout board.
- A small `FlashCam` system consisting of 12 channels for data taking together with a small data acquisition server which was used to analyze the data offline using PYTHON.

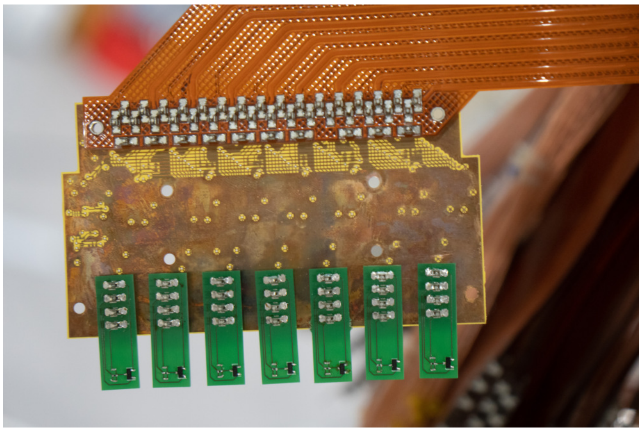

Figure 3.12: 7 Dummy front-end (DFE) connected to a CC4 board at the end of a Kapton flat band cable in the LEGEND-200 clean room at LNGS. The DFE consists of a feedback capacity of $C_f = 400\,\mathrm{fF}$, feedback resistor of $R_f = 1\,\mathrm{G\Omega}$, a pulser capacitance of $C_P = 100\,\mathrm{fF}$ and commercial BF862 JFET and can be used for fast pulser testing.

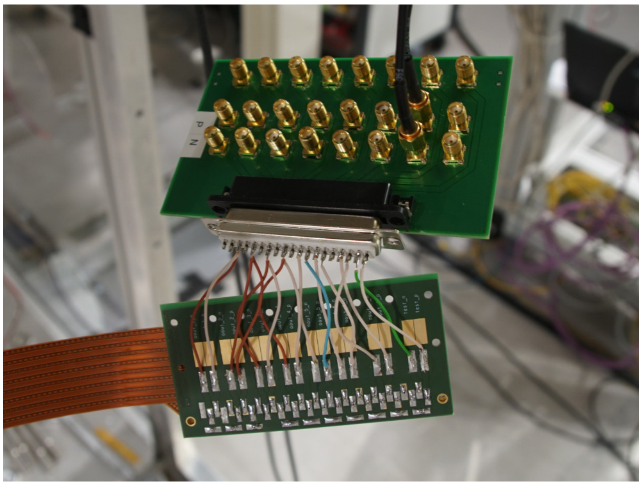

Figure 3.13: Connector board connected to the long Kapton flat band cable in the open lock at the LNGS clean room. Using this connector board, it was possible to directly inject pulses into the readout chain by avoiding the use of the pulser line of the head card itself.

Figure 3.14: The glove box with the open lock and the signal cables in the LEGEND-200 clean room at LNGS. Since the gate valve to the cryostat was closed, it was possible to directly access the cable, which is connected to the head card flange on top of the glove box.

Using this test setup, the hole readout chain with all newly developed components could be intensively tested for the first time in their final position in the LEGEND-200 clean room at LNGS. Here, the lock system was open so that it was possible to use the original long Kapton flat band cable, which will later connect the detector channels in the LAr cryostat and the final flange connection on top of the lock system. A picture of the open lock with the cable coming out can be found in Figure 3.14.

3.4.1.1 Buffer card testing

The buffer card is a subcard of the head card and provides the buffer termination for the incoming signals as well as the output impedance for the signals transferred from the head card at the cryostat flange to the fanout board. Each head card can handle 7 channels so that 7 individual buffer boards are placed

Table 3.1: Channel mapping of the two different buffer board versions tested in the setup.

Channel		input impedance Z_{in}	output impedance Z_{out}
CH1/CH2/CH3	("low")	$50\,\Omega$	$3.5\,\Omega$
CH4/CH5/CH6/CH7	("high")	$420\,\Omega$	$50\,\Omega$

on each head card. A picture of the buffer boards is shown in Figure 3.11a. The inital design of these cards consisted of two different types which have been connected to the individual channels of the head card according to Table 3.1 with the two types referred to as high and low impedance according to the table.
Figure 3.15 shows the response of these two buffer card types for a square wave pulse injected into the head card using the long Kapton flat band cable in the lock with the connector board. As expected, the two board configurations have different gain and therefore different signal amplitude. However, the zoom on the leading edge (c.f. Figure 3.15b) shows that the response at leading edge differs significantly between the configurations. Figure 3.16 shows the rise times for channel 1 and channel 2 as examples of the two configurations. The zoom at the end of the rise (c.f. Figure 3.16b) shows that the rise time from 10% to 90% maximum signal amplitude (RT90) for the low impedance configuration in channel 1 (48 ns) was much shorter than for the high impedance configuration in channel 4 (112 ns). However, the low impedance signal tends to take much more time to rise to its maximum amplitude with a rise time from 90% to 99% maximum signal amplitude (RT99) 1088 ns compared to 192 ns for the high impedance configuration.

By changing the output impedance taking all other possible influences into account, it could be shown that this behavior depends only on the output impedance. Figures of these comparisons can be found in the Appendix. To further analyze the features of the output impedance and investigate its influence on the rise time, the buffer board of channel 1 was modified so that different output impedance values could be tested.

Figure 3.17 shows the resulting response for four different output impedance configurations. The output impedance with $Z_{out} = 50\,\Omega$ shows the cleanest signals without any ringing. To better understand the differences between the four measurements, Figure 3.18 shows distributions of the rise times for RT90 and RT99 for the 1000 acquired waveforms for each configuration after interpolation the leading edge.

The Figure illustrates that the $Z_{out} = 50\,\Omega$ has by far the lowest rise times with very sharp distributions not only for RT90, but also for RT99. Moreover,

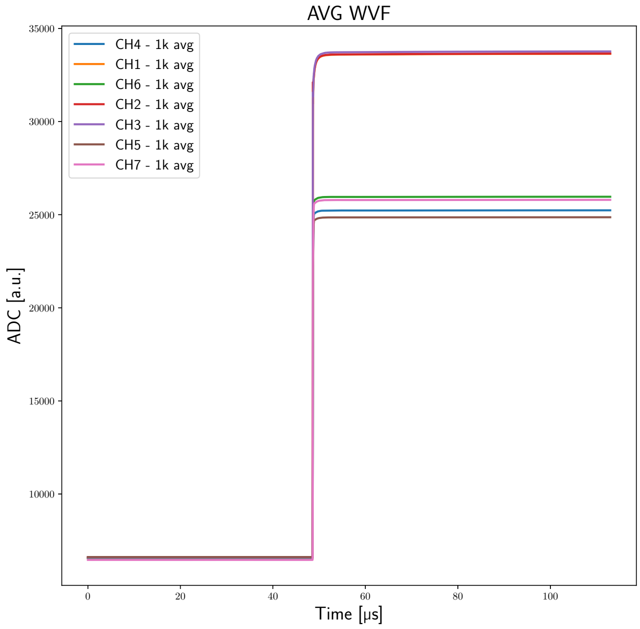

a) Full waveform

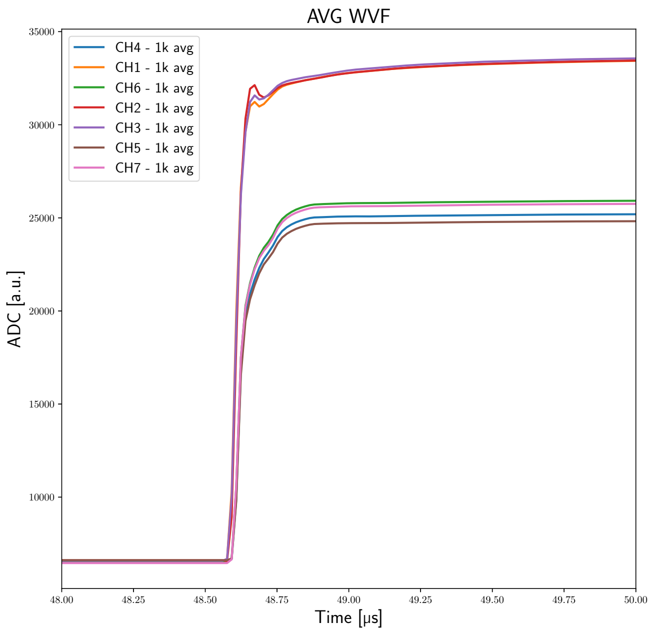

b) Zoom on leading edge

Figure 3.15: Response of the head electronic for square wave pulse injected into the long Kapton flat band cable for the channel mapping with different buffer board configurations according to Table 3.1. The injected pulse was a 1 V differential signal with 10 ns leading edge where 1000 waveforms have been averaged to generate cleaner signals.

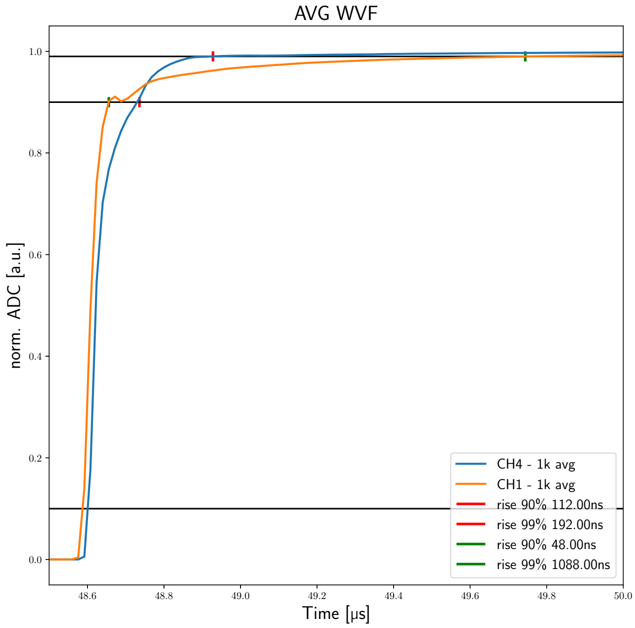

a) Full rising edge

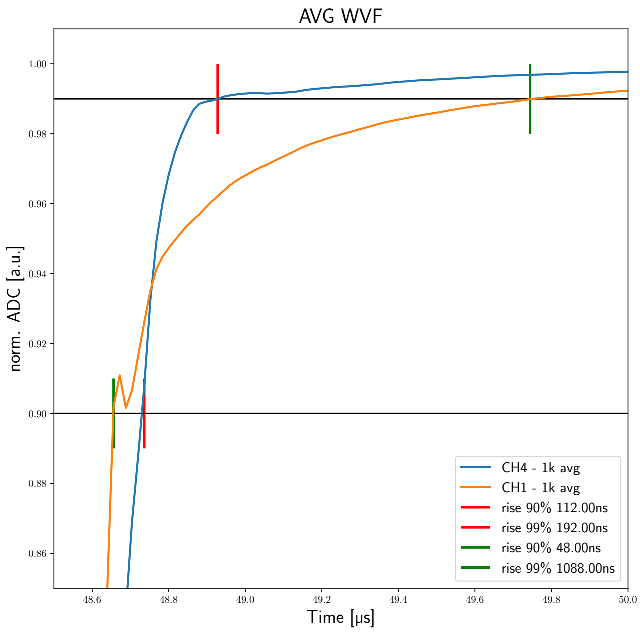

b) Zoom on end of rise

Figure 3.16: Rise Times of the head electronic for square wave pulse injected into the long Kapton flat band cable for a low CH1 and high (CH4) impedance channel (c.f. Table 3.1). The injected pulse was a 1 V differential signal with 10 ns leading edge where 1000 waveforms have been averaged to generate cleaner signals. Rise 90% corresponds to the rise time from 10% to 90% maximum amplitude where rise 99% is the rise time from 10% to 99%.

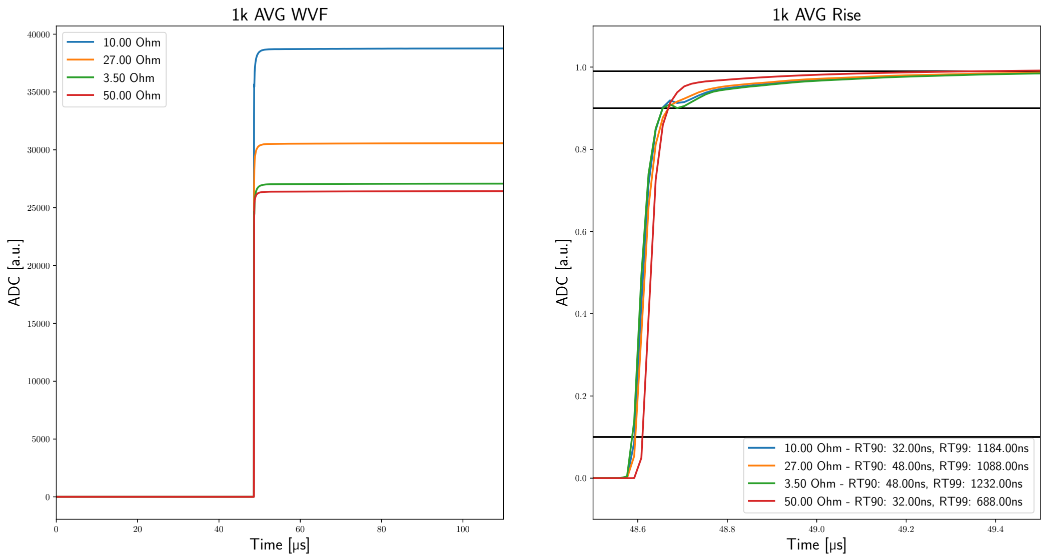

a) Full wvf and rise

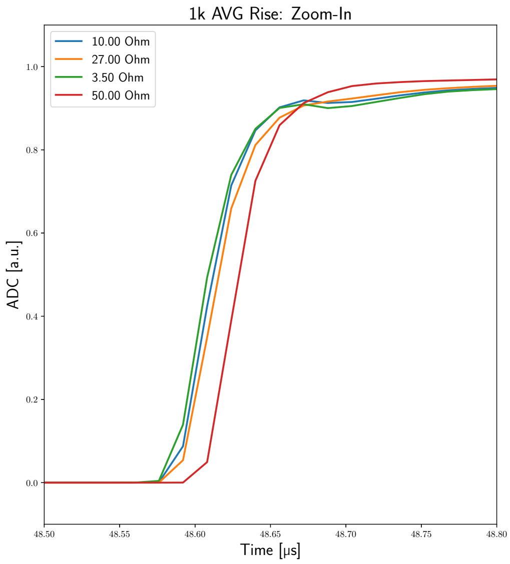

b) Zoom on rising edge

Figure 3.17: Response of the head electronic for square wave pulses injected into the long Kapton flat band cable for the channel mapping with channel 1 buffer board modified to four different output impedance configurations. The left plot shows the raw signal for 1000 waveforms averaged while the middle plot shows normalized waveforms with their corresponding rise time values for RT90 and RT99. The right plot is zoomed on the leading edge.

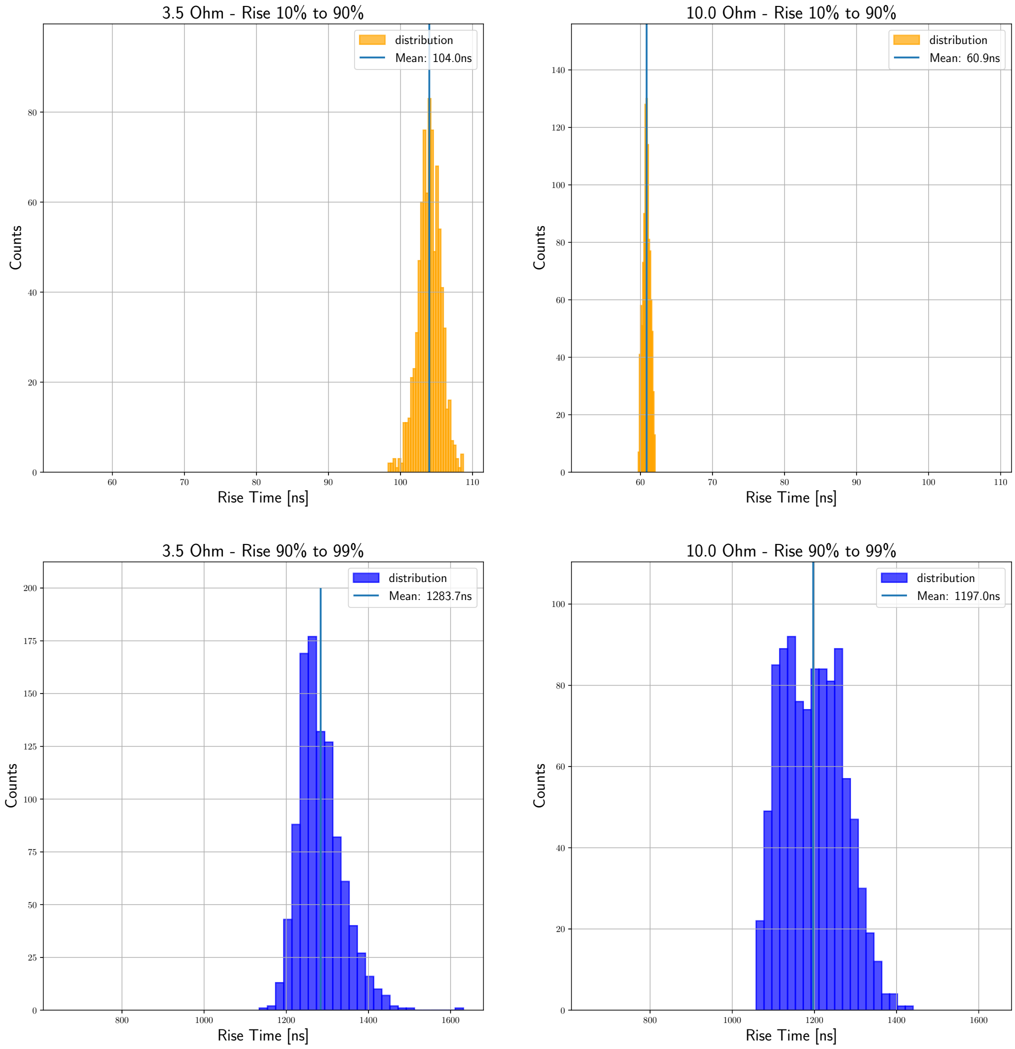

a) $3.5\,\Omega$ and $10\,\Omega$

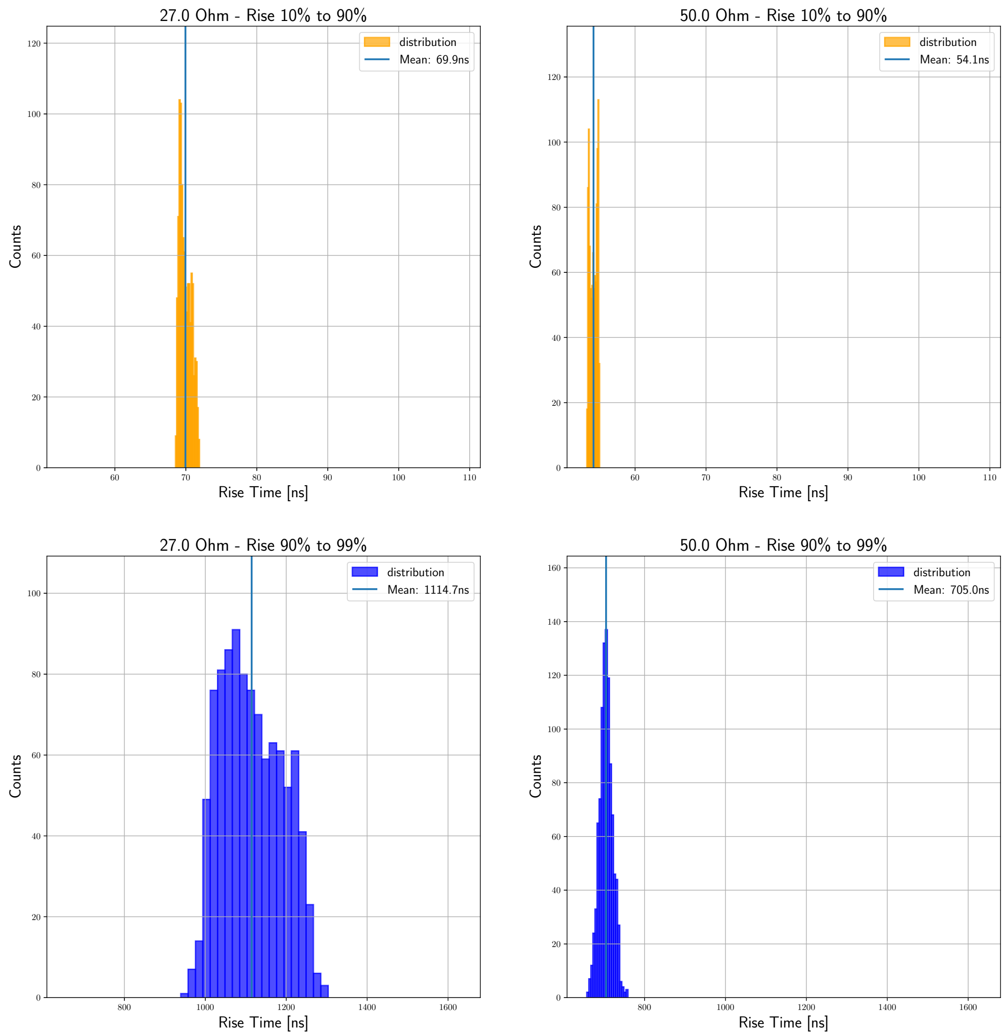

b) 27 Ω and 50 Ω

Figure 3.18: Rise time distribution for 1000 square wave pulses injected into the long Kapton flat band cable for the channel mapping with channel 1 buffer board modified to four different output impedance configurations. The yellow distributions correspond to the RT90 values while the blue ones to the rise time from 90% to 99% maximum signal amplitude. All waveforms have been interpolated at the leading edge to increase rise time extraction efficiency.

the very low values for RT99 confirm the higher signal integrity already seen in the response plot in Figure 3.17. Summarizing, the measurements show that a output impedance with $Z_{out} = 50\,\Omega$ shows fastest rise times of RT90 = 54.1 ns (RT99 = 759.1 ns) and highest signal integrity.

3.4.1.2 CC4 testing

To check the signal integrity and the correct functionality of the CC4, six production CC4 have been tested by injecting pulses into the pulser input of the head electronics via the long Kapton flat band cable to each CC4 which are connected with 7 DFE at each channel. Six different CC4s have been tested named according to their type of connector to the Kapton flat band cable (reverse or straight) and the production number. 1000 waveforms have been acquired with `FlashCam` for all 7 channel. Figure 3.19 shows the resulting waveform output of all 7 channels at the rising edge where the 1000 waveforms have been averaged for plotting. The full waveform decay can be found in Figure 3.20. In all channels, the reverse CC4 1 shows distortion in the rising edge, leading to higher rise time. Furthermore, straight CC4 number 2 has a delayed start point of the rising edge in all channels and features an overshoot in CH4, which also results in a faster rise time. The reverse CC4 2 and 3 have almost similar properties in the rising edge in all channels with slightly faster rise times of $\sim$ 8 ns for reverse CC4 2 and reverse CC4 3 showing a slight distortion in CH3. However, they feature lower amplitudes in CH3 and CH5 due to a missing signal of one of the differential signal lines. The reverse CC4 2 and 3 show almost identical responses in all channels and similar rise times with slightly faster rise times of $\sim$ 5 ns for straight CC4 2. These rise times correspond with the rise times of reverse CC4 1, which also features a missing signal of one of the differential signal lines in CH4. Overall, the CC4 performance is good, and no major issues could be identified. The distortions, as well as the missing signals, maybe occur due to badly connected cables. If the problems would occur due to the bad performance of the CC4, a further study with multiple detectors and multiple CC4s could identify them.
To further investigate the performance, Figure 3.21 shows the distributions of the decay times among all channels. At first glance, the figure illustrates sharp and clean decay time distributions in all channels for all CC4 with values in the range of $\sim$ 500 µs which is expected for the values of the DFE. Moreover, the relative difference in the decay time between the CC4s stays the same among the channels. Summarizing, this indicates that no major problems have been identified for the CC4s.

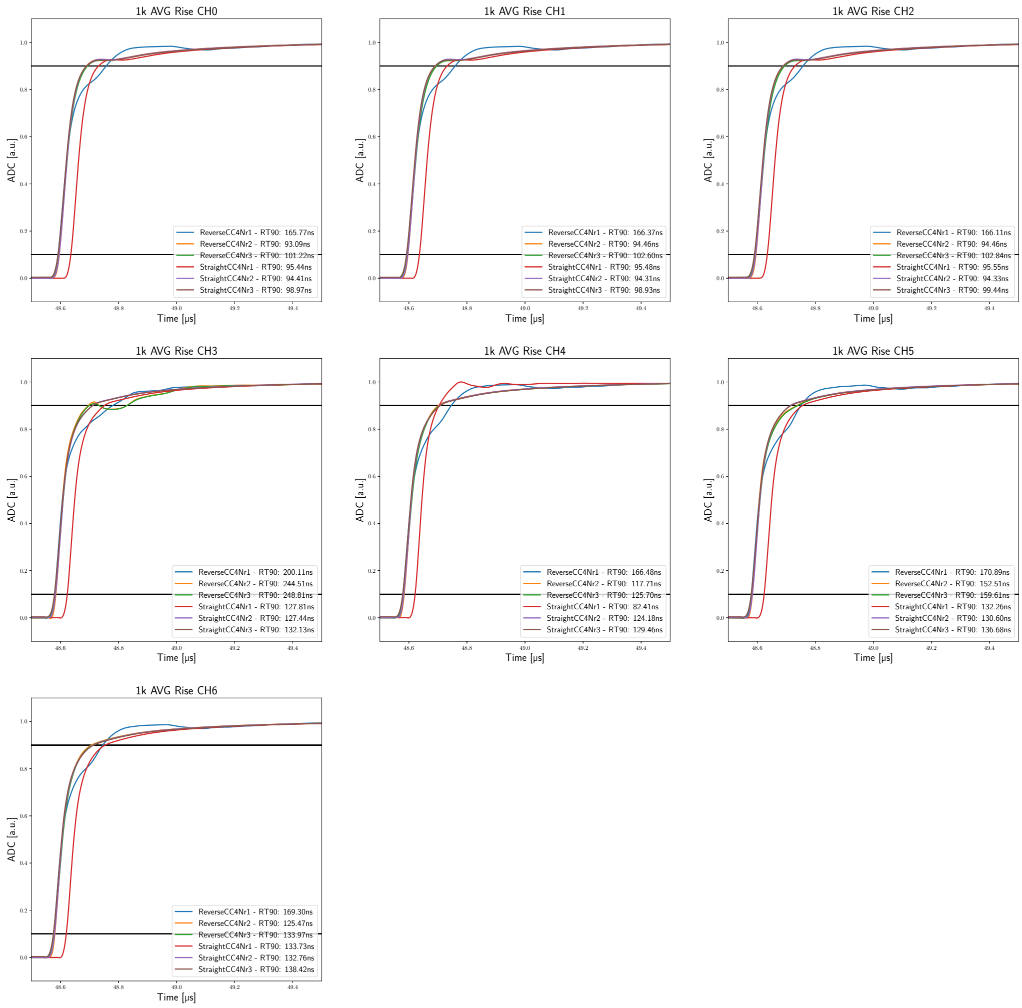

Figure 3.19: Averaged output waveforms of all six tested CC4s at the rising edge. A square wave was injected into the pulser input of the head electronics, and 1000 waveforms have been acquired with `FlashCam`. The rise times are calculated individually for each waveform and averaged.

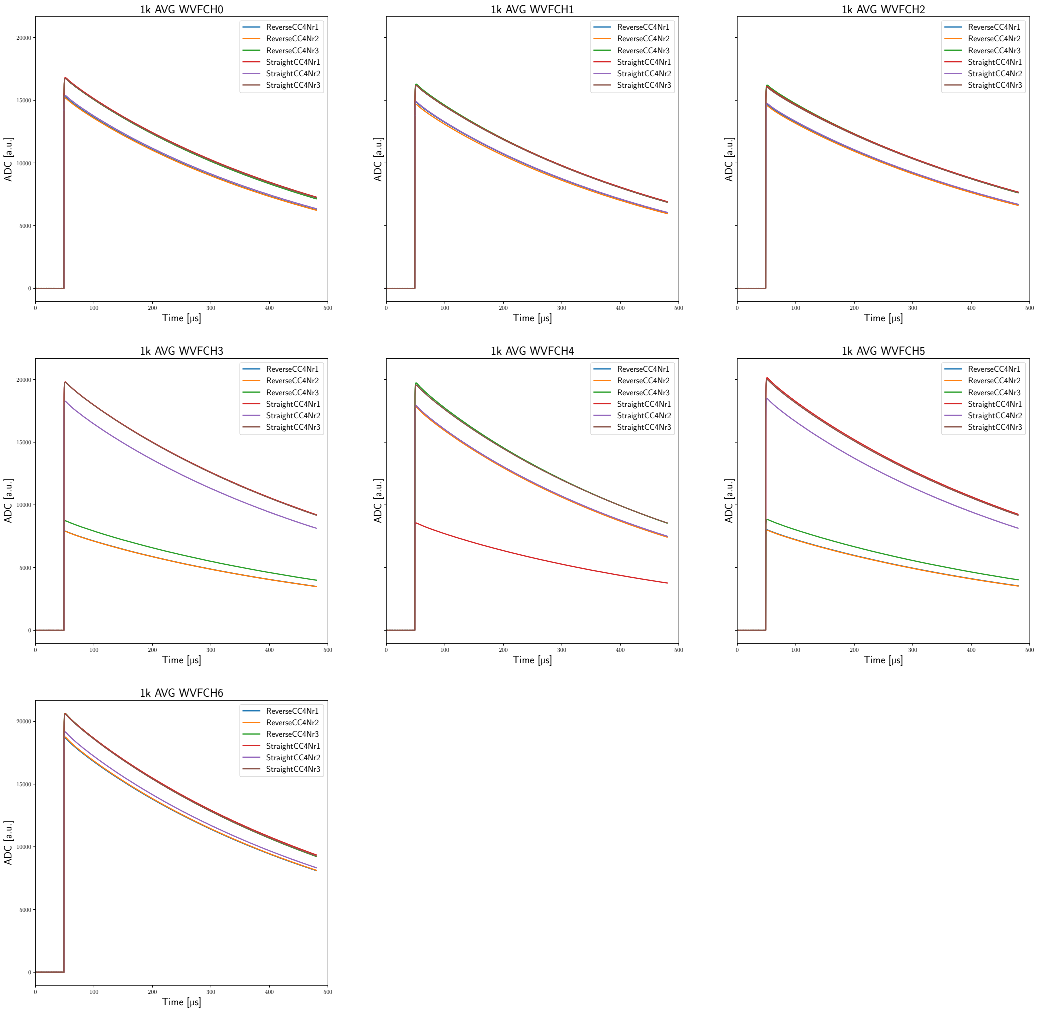

Figure 3.20: Averaged full output waveforms of all six tested CC4s. A square wave was injected into the pulser input of the head electronics, and 1000 waveforms have been acquired with `FlashCam`.

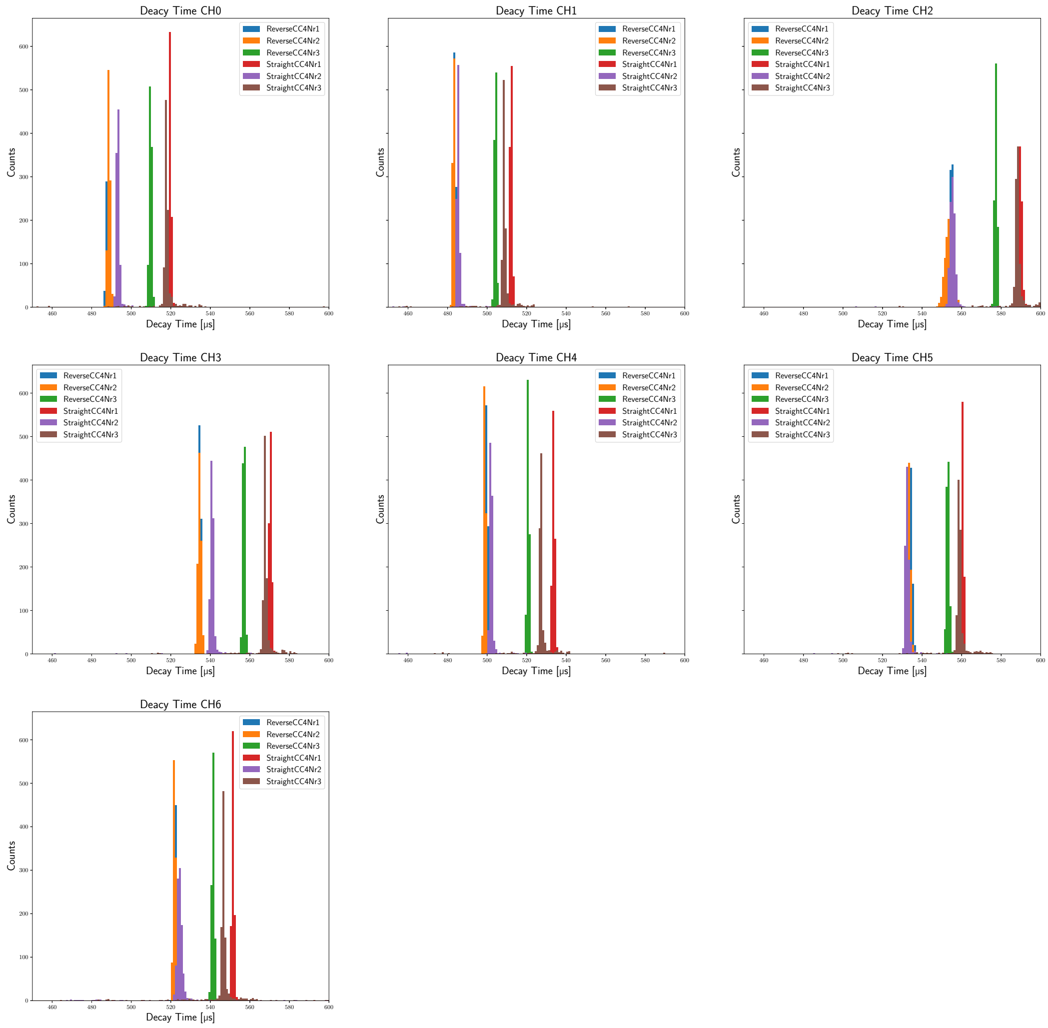

Figure 3.21: Decay Times of all six tested CC4s for all seven channels. A square wave was injected into the pulser input of the head electronics, and 1000 waveforms have been acquired with `FlashCam`. Following, an offline analysis extracted the decay times by an exponential fit to the decay tail.

3.4.2 Commissioning tests

The course of this thesis included a second research stay in October and November 2021 at LNGS in which the commissioning of the first detectors in the LEGEND-200 cryostat was performed. To be able to deploy the detectors in the LAr cryostat, the HV system was tested to check performance which is described in Section 3.4.2.1. Following, the so-called 4 detector test is explained in Section 3.4.2.2 given an overview of the setup and the corresponding measurement together with the analysis of the full data set.

3.4.2.1 High voltage system testing

The high voltage (HV) system of LEGEND-200 consists of a CAEN HV system which can provide HV in 120 individual channels each. A picture of the CAEN system is shown in Figure 3.22a. It is connected with special HV cables to the filter card, which is a custom-designed HV filter system mounted at the cryostat flange on top of the lock to filter noise. The HV is then feed through the cryostat with custom-designed clean HV cables before they connect to each detector via wire bonding. To test its functionality, two HV cables coming out of the lock next to the signal cables (c.f. Figure 3.14) have been connected through a capacitor to the pulser line of two DFEs. Following, square wave pulses have been injected into the pulser input of the head electronics consisting of a single fanout board and a head card mounted at the flange (c.f. Section 3.4.1). The chain was closed by a CC4 connected with the DFE hosting the HV connection. The data was acquired with the `FlashCam` system for several runs. An example of a resulting waveform is shown in Figure 3.23. The waveform features high frequency all over its range which could lower resolution. To investigate its origin, different measurements were performed where each measurement consists of the simultaneous readout of two HV connected and four HV disconnected channels with a single CC4. After the extraction of the baseline of each aquired waveform, the power spectrum density (PoSD) was calculated for each individual waveform by a periodogram with Hann window. The individual PoSD are averaged to make them comparable. In a first measurement round, the following measurements were performed:

- *HVGrounded_ CAENOff*: The HV system was grounded at the flange, but the system itself switched off.
- *HVNotconnected_ FilterGERDAmod*: The HV system was turned on without any voltage applied, and the filter card was modified according to improvements found in GERDA.

a) CAEN HV system

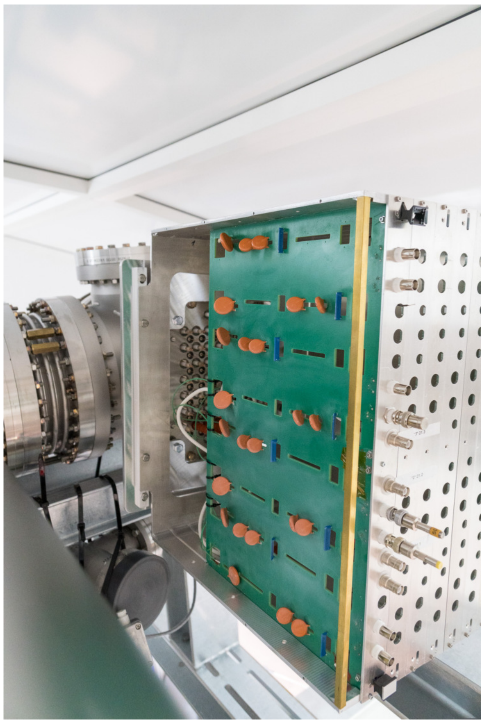

b) HV filter card mounted at the flange on top of the lock

Figure 3.22: The HV system of LEGEND-200 consisting of a CAEN HV system and a custom-designed filter card. The CAEN system is connected with special HV cables to the filter card which is mounted at the flange on top of the lock system. The HV is the feed through the cryostat with custom-designed HV cables which then connect to the detectors via wire bonding.

- *HVconnectedBut0V_Jumper*: The HV was turned on without any voltage applied, and the jumper on the CAEN system was plugged in.
- *HVconnectedBut0V_NoJumper*: The HV was turned on without any voltage applied, and the jumper on the CAEN system was not plugged in.
- *HVconnected_Jumper*: The HV was turned on with 5 V applied, and the jumper on the CAEN system was plugged in.
- *HVconnected_NoJumper*: The HV was turned on with 5 V applied, and the jumper on the CAEN system was not plugged in.

The so generated PoSD for all measurements can be found in the Appendix. To account for the amount of noise not originating from the HV system, all

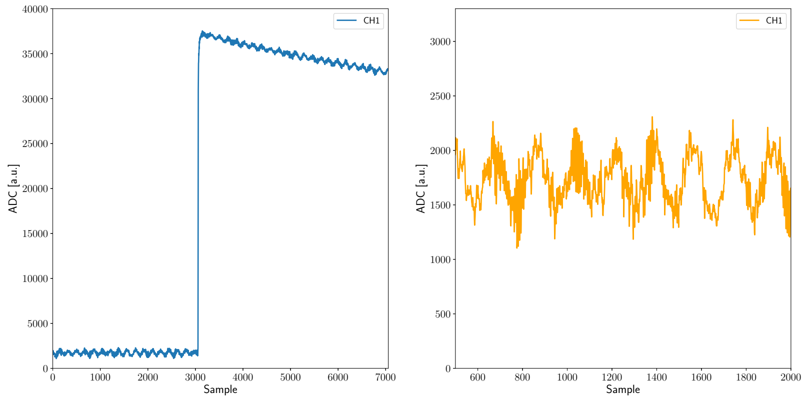

Figure 3.23: Example waveform of the HV test where the HV system without any voltage applied was connected over a capacity to the pulser line of a DFE. The waveform features high frequency noise on its hole range.

PoSD of the channels not connected to HV have been averaged and subtracted from the connected ones. Figure 3.24 shows the resulting PoSD of the not connected channels. It features very low noise with a dominant peak at 25 kHz. In contrast, Figure 3.25 shows the resulting PoSD of the two HV connected channels in the range between 0.1 MHz and 2 MHz for all six measurements after substracting the not connected one. At first look, a much higher noise can be identified throughout all measurements. However, the switching off of the CAEN system results in a lower noise by several order of magnitudes, as can be seen on the orange and blue curves. Furthermore, the modification of the filter card could further suppress the noise while even suppressing the dominant peak at 350 kHz down to a subdominant one. To better investigate the influence of a connected jumper, Figure 3.26 shows the percentage difference between the PoSD of the jumper connected and not connected measurements. The plot illustrates that a disconnected jumper has no big influence on the dominant peak at 350 kHz compared to switching off the CAEN system.
During commissioning in preparation of the 4 detector test, a possible noise source was identified to be a PLC which is operating next to the lock system in the controlling electronics. To verify this hypothesis, a second HV system test was performed which used the GERDA modifictaion of the filter card and the same measurement setup as described above:

- **Test 1**: HV disconnected and PLC switched off.
- **Test 2**: HV disconnected and PLC switched on.

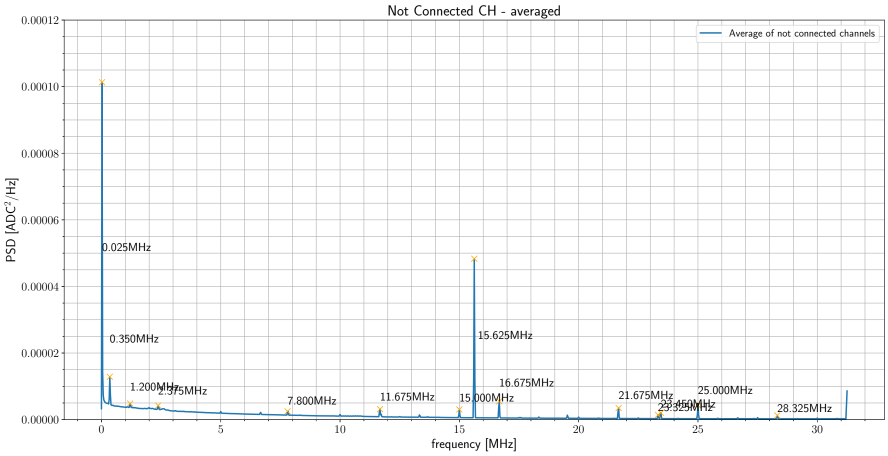

Figure 3.24: Averaged PoSD of all not connected channels. Some dominant peaks are marked and labeled with their corresponding peak frequency.

- **Test 3**: HV connected and PLC switched off.
- **Test 4**: HV connected and PLC switched on.

Instead of full waveforms with pulser events, only baseline data was stored and PoSDs have been generated according to the described procedure (c.f. Appendix). Following, Figure 3.27 shows the PoSD for the tests with PLC switched on subtracted from the tests with PLC switched off for the cases with and withput applied voltage to the HV system. The effect of switching off the PLC is clearly visible in the resulting PoSD. As a switching device, the PLC seems to be the major source for 350 kHz noise dominant in all previous measurements. It is unknown where the 60 kHz and 1.2 MHz noise as well as the high-frequency noise is arising from. Therefore, the 4 detector is perfect for the determination of noise in a detector setup in the LAr to characterize the real influences on the detector performance and the energy resolution.

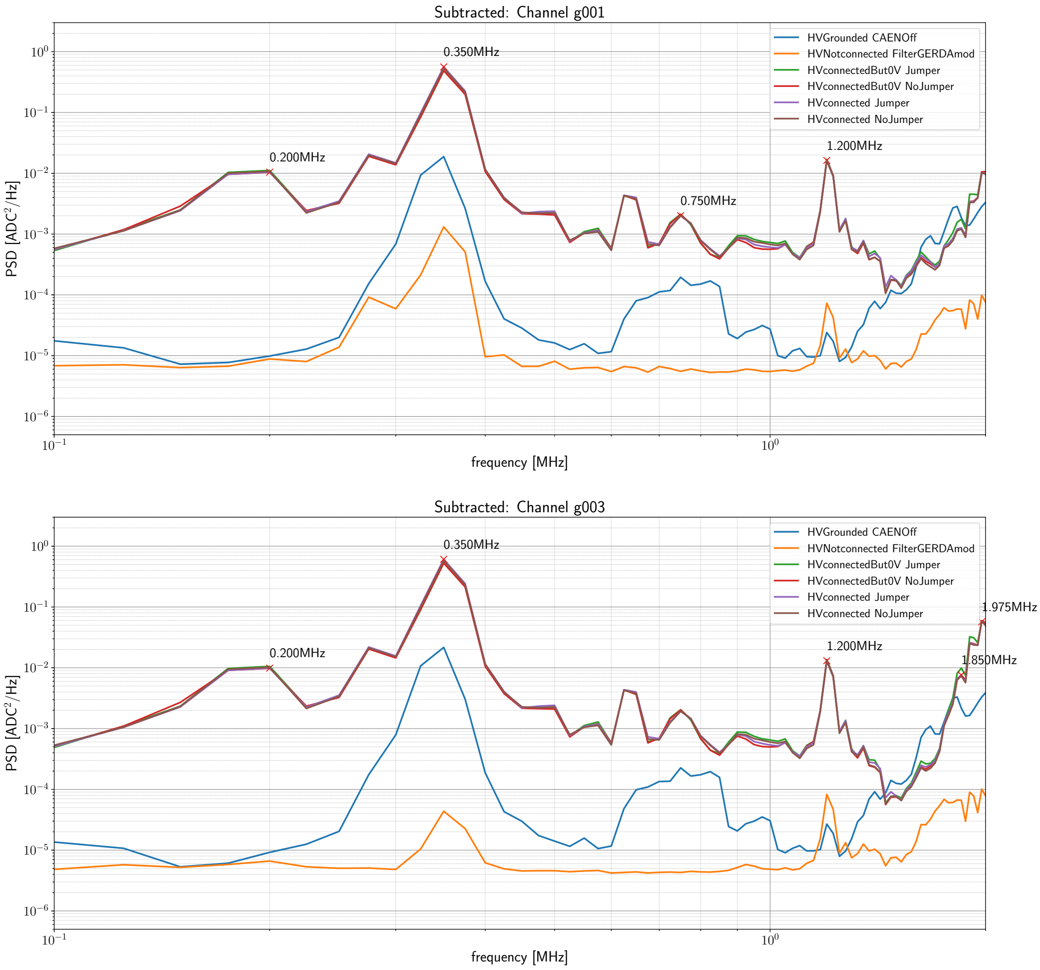

Figure 3.25: PoSD of the two connected channels in the range between 0.1 MHz and 2 MHz where the average PoSD of the not connected channels has been substracted. Dominant peaks are marked and labeled with their corresponding peak frequency.

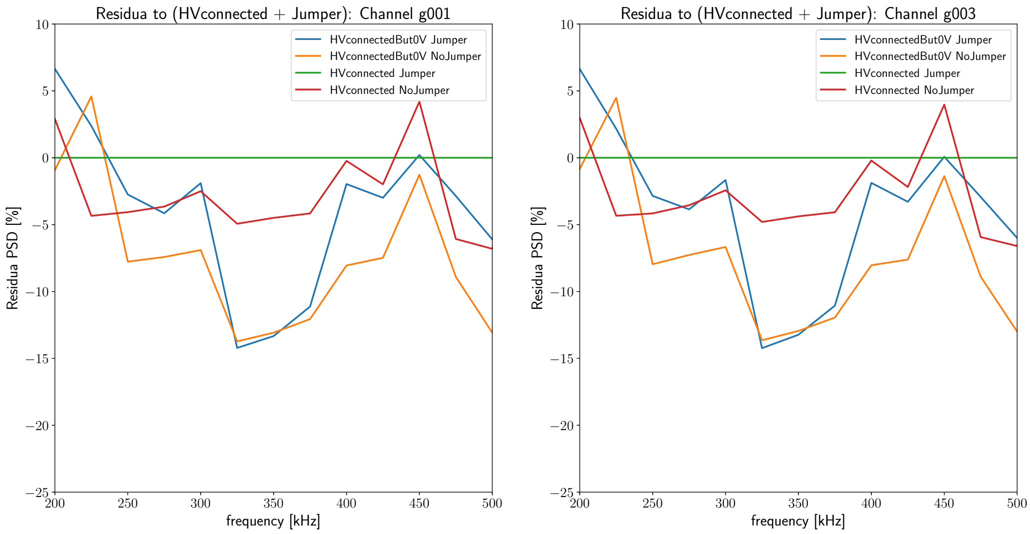

Figure 3.26: Percentage difference between the PoSD of the jumper connected and not connected measurements around the dominant peak at 350 kHz

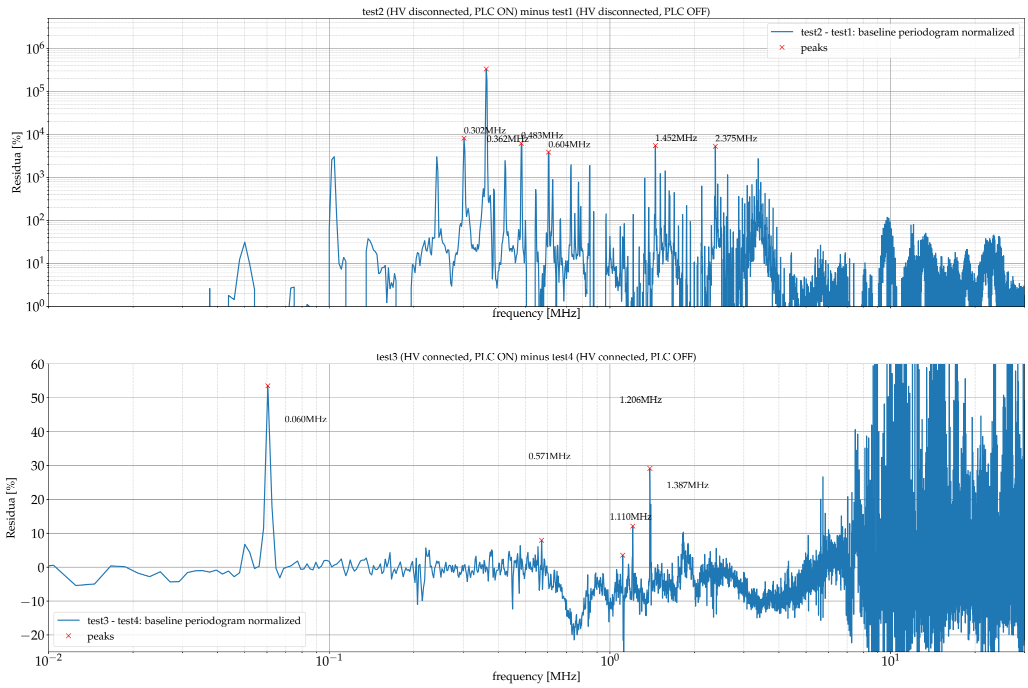

Figure 3.27: PoSD of the tests PLC switched on subtracted from the tests with PLC switched off for the cases with and withput applied voltage to the HV system. The residua in perecentage are plotted versus the frequency with the upper plot in log scale on both axes.

No	Str	Pos	Detector	Type	Mass (kg)	V_B (V)	Ch	Plate	LMFE
1	1	Top	P00749B	PPC	0.922	-	1	PEN	104
2	1	Bottom	P00909A	PPC	0.600	2200	0	PEN	55
3	2	Top	B00079B	BEGe	0.736	3500	3	Si	9
4	2	Bottom	B00035B	BEGe	0.810	4000	2	Si	110

Table 3.2: Overview of the detectors installed in the 4 detector test. The actual applied bias voltage is denoted as V_B with V_{op} being the optimal operation voltage. Detector 1 could not be depleted at all so that the remaining LMFE was used for pulser testing. Detector 2 had reduced V_B due to too high leakage current.

3.4.2.2 The 4 detector test

At the beginning of November 2021, the first 4 detectors operated in LEGEND-200 could be installed in the LAr cryostat to perform further test the electronic performance of the full detector system. Two strings are installed with string 1 containing two PPC and string 2 containing two BEGe detectors. The remaining CC4 channels have been equipped with clean DFE. Table 3.2 shows an overview of the detectors and their properties. Due to high leakage current, one PPC detector could not be depleted at all and one featured a reduced bias voltage. The disconnected detector remained in the cryostat so that its LMFE could be used for pulser testing. A picture of the detectors in the lock before lowering into the LAr cryostat can be found in Figure 3.28. After the detectors have been installed in this final configuration, the two strings have been lowered down the cryostat. Using the source insertion system (SIS), a ^{228}Th source was lowered into the LAr close to the detector so that a calibration measurement for ~ 3 h could be performed while a waveform generator pulsed differential signals in the range ~ 5 MeV with a fequency of 0.2 Hz.
^{228}Th is a radioactive isotope with half-life of $T_{1/2} = 1.9$ yr which decays via several alpha and beta decays to the stable nucleus ^{208}Pb. The decay scheme is illustrated in Figure 3.29. During this decay scheme, various excited states are produced (mostly ^{212}Bi and ^{208}Tl) which radiate intense gamma lines with energies in the range from 200 keV up to 2.6 MeV from which a precise energy calibration can be produced. Furthermore, the high statistics DEP peak can be used for PSD calibration. The most prominent gamma lines are listed in Table 3.3.

The data analysis procedure strictly follows the approach from Edzards developed for the Post-GERDA test [32]. It is based on a hierarchical structure shown in Figure 3.30 consisting of three `Tier` stages comparable to those in GERDA [100]. The procedure was based on a highly customized PYTHON

Figure 3.28: Photograph of the two strings of the 4 detector test in the lock before lowering into the cryostat. The two BEGe detectors are on the left, the two PPC detectors on the right. The CC4 is seen in the middle connected to the LMFEs of the detector while having additional channels filled up with DFEs. Image courtesy of M. Willers.

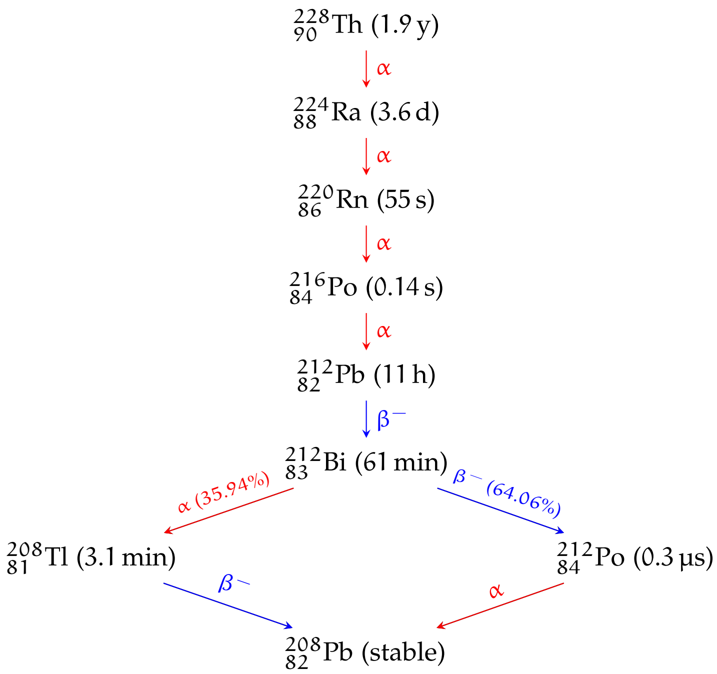

Figure 3.29: Decay scheme of radioactive isotop ^{228}Th which decays via several alpha and beta decays to the stable nucleus ^{208}Pb. Scheme adapted from [90]

Isotope	Energy (keV)	Intensity (%)	Isotope	Energy (keV)	Intensity (%)
^{208}Tl	510.77(10)	22.6(2)	^{212}Bi	893.408(5)	0.378(19)
	511.00	Annihilation	^{212}Bi	952.120(11)	0.17(3)
^{208}Tl	583.187(2)	85.0(3)	^{212}Bi	1078.62(10)	0.564(19)
^{137}Cs	661.657(3)	85.1(2)	^{208}Tl	1592.511(10)	DEP
^{212}Bi	727.330(9)	6.67(9)	^{212}Bi	1620.5(1)	1.47(3)
^{208}Tl	763.13(8)	1.79(3)	^{208}Tl	2103.511(10)	SEP
^{212}Bi	785.37(8)	1.102(13)	^{208}Tl	2614.511(10)	99.754(4)
^{208}Tl	860.557(4)	12.5(1)			

Table 3.3: Most prominent gamma lines with their corresponding energy and intensity of the ^{228}Th decay chain. Uncertainties are given in brackets. Data from [99]

code developed. The code enables the use of customized JUPYTER notebooks and global configuration files to meet the requirements of the 4 detector test. The raw waveforms, timestamps and baselines acquired with `FlashCam` are initially converted to the HDF5 format in the `Tier1` stage. The waveform data has a length of 15000 samples resulting in a total trace length of 240 µs per event (sample time for `FlashCam` 16 ns). In the `Tier2` stage, several waveform computations are performed resulting in several waveform quality parameters as well as event information parameters such as energy, current or rise time. Figure 3.31 shows an example for a typical event in the the detector 3 (BEGe). After the baseline (averaging over the first 500 samples) is subtracted (green curve) from the raw waveform data (blue curve), an exponential fit (red curve) is performed in the range from 3000 to 13000 samples in the decay tail. In a next step, all decay times are programmed and the resulting distribution is fitted with a Lorentzian function to extract the peak position τ_0 [32]. The resulting distributions with the corresponding fits can be found in the Appendix. Following, the waveform can be pole-zero corrected (orange curve), which is essentially the correction of the exponentially decaying tail with the help of a IIR filter, and the decay time τ_0 of each channel [101]. Detailed information about pole-zero correction can be found in Section 4.2.4. The energy is then extracted with asymmetrical trapezoidal filter with a varying rise and flat top time where the best energy resolution was found to be at a filter rise time of 4 µs and a flat top time of 3 µs. The specific filter parameters need to ensure a sufficiently long flat top time for complete charge integration and sufficient long rise time to integrate away high-frequency noise. The filter time plays an important role in the underlying electronic noise. More details about electronic noise and the underlying processes can be found in Section 3.2. Finally, the energy is extracted using a fixed-time-pickoff (FTP) which is a fixed time point relative to the onset of the charge collection t_0, e.g., at the center or maximum of the flat top region.

Furthermore, to ensure sufficient data quality, several quality parameters are extracted from the waveforms and used for quality cuts. The baseline mean and RMS is calculated by averaging over the first 500 samples of the waveforms and calculating the standard deviation while the baseline slope is generated by a linear fit in the range. Cuts set on the resulting baseline mean and RMS distributions enable sufficient data quality since these two quantities are estimators for the stability of the detector leakage current and the electronic noise. Respectively, the baseline slope is a proxy for pre-trace pile-up where a cut on the slope distribution is able to reject such events by setting a threshold on the slope parameters. The resulting distributions together with their cut windows can be found in the Appendix. In-trace pile-up was rejected by a method from [32] where the number of energy depositions in an event is counted

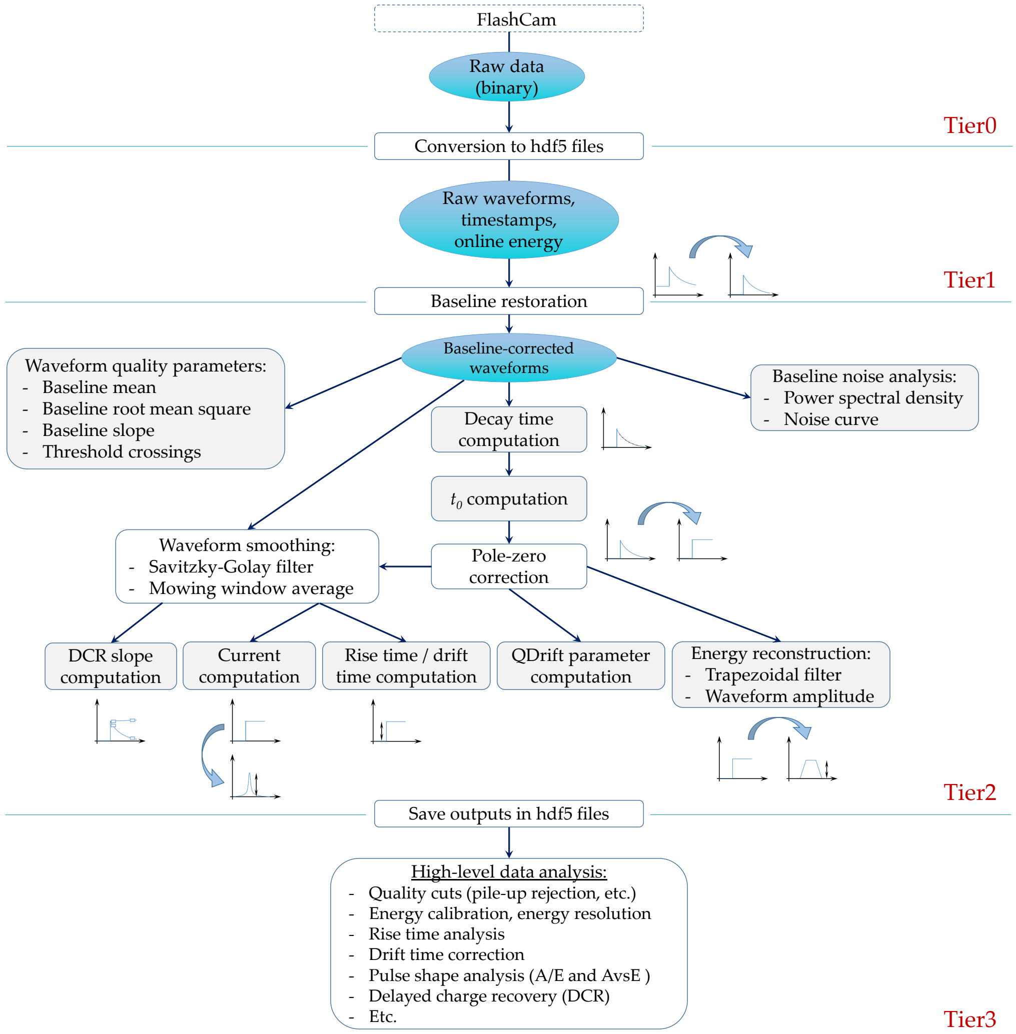

Figure 3.30: Overview of the analysis chain used for processing the data taken with the 4 detector test. The outputs of the `Tier2` level are indicated by the grey colored boxes. Figure and caption from [32] where also a detailed description of the procedures is presented.

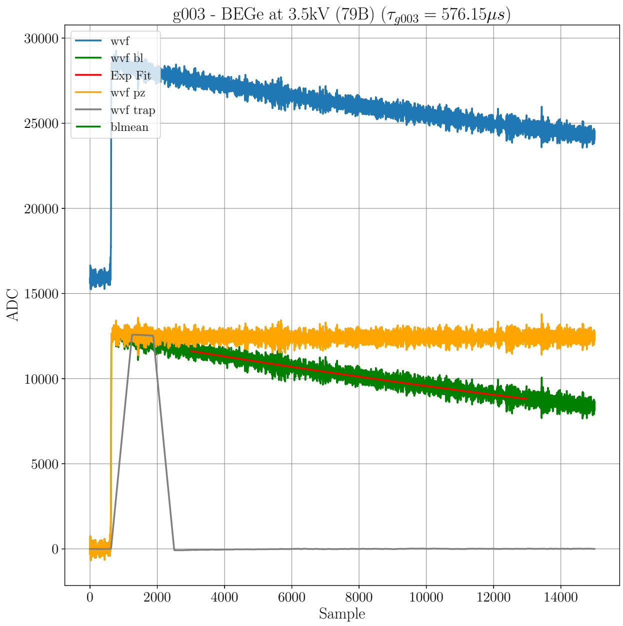

Figure 3.31: Waveform example of an event in the detector 3 (BEGe). The blue curve is the unprocessed data, the green one the baseline subtracted where the baseline is calculated by averaging over the first 500 samples. The red fit curve shows an exponential fit in the range from 3000 to 13000, from which the pole-zero corrected waveform (orange) can be calculated by a infinite impulse response (IIR) filter. The energy can then be extracted with a trapezoidal shaper (grey) with varying rise and flat top time where the energy corresponds to the maximum height of the resulting trapezoidal curve.

with a trapezoidal filter with rise time of 200 ns and flat top time of 2 µs where the number of depositions is calculated by the number of times the resulting trapezoidal filter curve exceeds a specific threshold [32]. In addition, several quality cuts are set on the rise rime, drift time, decay time and energy greater than zero. The resulting survival probabilities are summarized in Table 3.4.

The so-generated spectra are now energy calibrated by identifying the most prominent peak and its peak center μ_{FEP} in the spectrum with the FEP at 2614.511 keV and calibrating the spectrum according to the formula

$$E[\mathrm{keV}] = E[\mathrm{ADC}] \cdot \frac{2614.511\,\mathrm{keV}}{\mu_{\mathrm{FEP}}} \tag{3.31}$$

The resulting spectra for the three detector channel are illustrated in Figure It can already be seen that the measurement is highly limited by statistics. Several monoenergetic gamma lines can be identified in this spectrum which

CH	Detector	Type	Survival Probability (%)
0	P00909A	PPC	60.27
1	LMFE	-	88.70
2	B00035B	BEGe	60.61
3	B00079B	BEGe	89.49
4	DFE	-	94.46
5	DFE	-	91.22

Table 3.4: Survival probabilites after cuts for all channels of the 4 detector test.

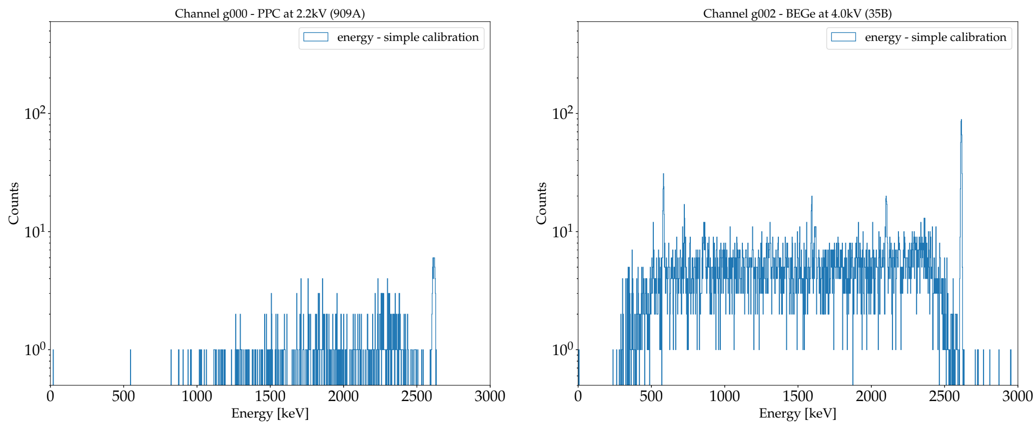

a) CH0 and CH2

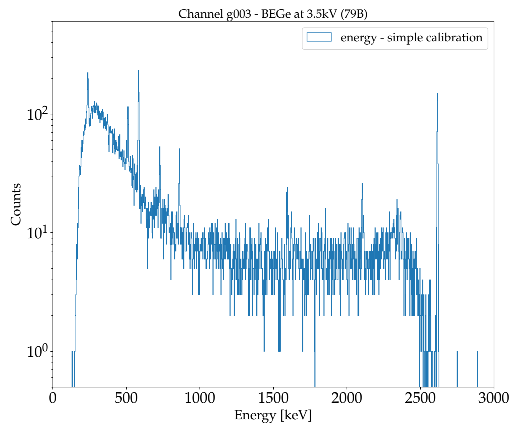

b) CH3

Figure 3.32: Energy spectrum of the three connected detectors in the 4 detector after simple calibration according to Equation 3.31. The most prominent peak and its peak center μ_{FEP} in the spectrum was identifyied with the FEP at 2614.511 keV.

could be fitted with a fit function of the form [90]

$$f(E) = \underbrace{A \cdot \exp\left(-\frac{(E-\mu)^2}{2\sigma^2}\right)}_{\text{Gaussian}} + \underbrace{\frac{B}{2}\mathrm{erfc}\left(\frac{E-\mu}{\sqrt{2}\sigma}\right)}_{\text{Low-energy step}} + \underbrace{C + D\cdot(E-\mu)}_{\text{Linear background}}$$
$$+ \underbrace{\frac{F}{2}\exp\left(\frac{E-\mu}{\delta}\right)\mathrm{erfc}\left(\frac{E-\mu}{\sqrt{2}\sigma}+\frac{\sigma}{\sqrt{2}\delta}\right)}_{\text{Low-energy tail}} \tag{3.32}$$

where A, B, C, D and F are normalization factors, μ the peak position, σ the standard deviation of the Gaussian distribution and δ the decay constant of an exponential. The formula consists of a Gaussian function with a background modelled by a low-energy step with a linear background and a low-energy tail. The low-energy tail corresponds to the peak shape distortion due to incomplete charge collection or pile-up events in the energy spectrum [90]. An arbitray peak searching algorithm was now implemented which searches for significant peaks in the simple calibrated spectrum of Figure 3.32 in a appropiate window around the peaks and accepts peaks as found if the found peak center is less than 5 keV away from the expected peak center according to the simple calibration in Equation 3.31 and the values from Table 3.3. Afterwards, the identified peaks are fitted with Equation 3.32. However, because the statistical limitations in the energy spectrum are too large, only the FEP was fitted with Equation 3.32 while the fits for the other peaks used a simpler function of the form

$$f(E) = \underbrace{A \cdot \exp\left(-\frac{(E-\mu)^2}{2\sigma^2}\right)}_{\text{Gaussian}} + \underbrace{C + D\cdot(E-\mu)}_{\text{Linear background}} \tag{3.33}$$

$$\tag{3.34}$$

only consisting of a Gaussian together with a linear background. The peak search in the appropiate fit windows together with the fit function are illustrated in the Appendix. Following, the peak centers in terms of ADC units are extracted and plotted with their corresponding calibration energy to fit a calibration curve of the form

$$E[\mathrm{keV}] = a \cdot E[\mathrm{ADC}] + b \tag{3.35}$$

where a and b denote the fit parameters. The resulting calibration curve is shown in Figure 3.33. The detectors and the corresponding electronics show high linear behavior over the full energy range, with only tiny deviations, all originating from the statistical limitations of the fits. It can be seen that

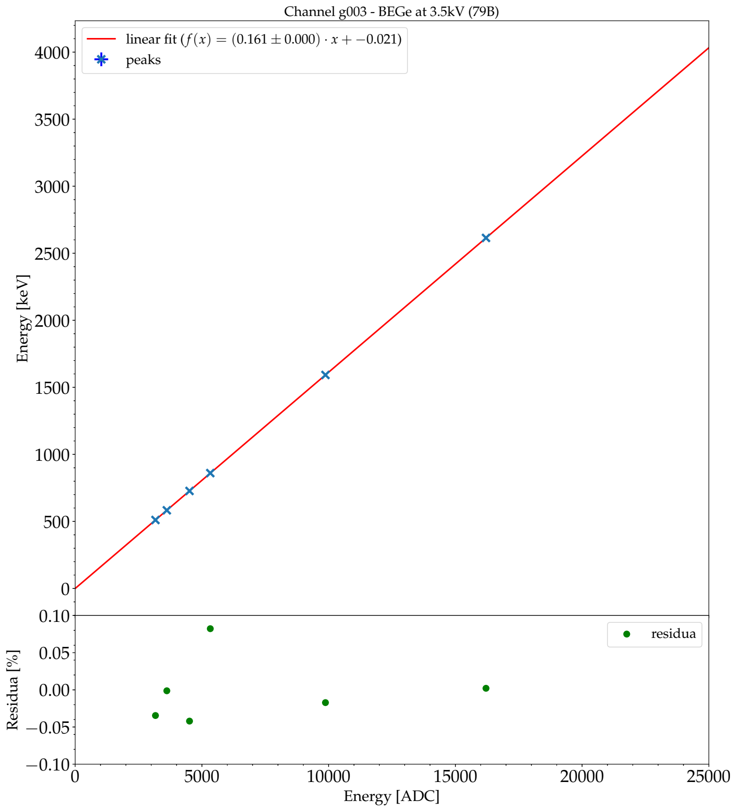

a) BEGe B00035B

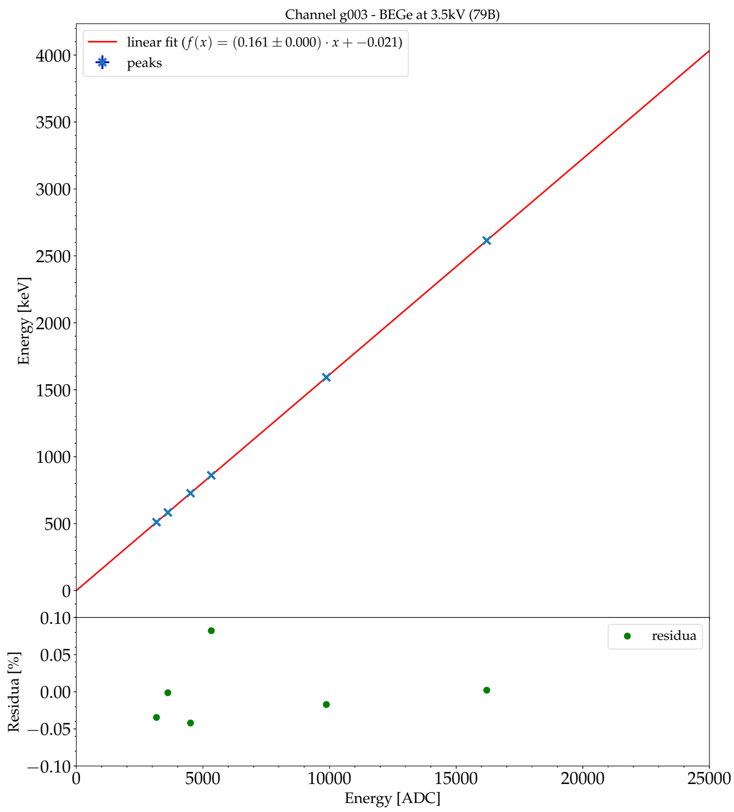

b) BEGe B00079B

Figure 3.33: Energy calibration curves for the two BEGe detectors in the 4 detector test. The data points are marked with their size corresponding to the uncertainties. The linear fit is shown as red curve with the corresponding fit parameters given in the legend. The lower plot illustrates the residuals. Since the PPC detector in channel 1 was highly limited by statistics only a simple calibration was performed.

CH	Detector	Type	FWHM (keV)	PGT FWHM (keV)
2	B00035B	BEGe	8.47	2.21
3	B00079B	BEGe	5.42	2.77

Table 3.5: Energy resolution of the two BEGe detectors in the ^{228}Th calibration run in the 4 detector test. The resolution in terms of FWHM is shown for the $Q_{\beta\beta}$ value at 2039.06 keV. The values in the PGT column correspond to the measured resoltuions during he calibration runs in the post gerda test coming from [32].

detector 2 (BEGe) performed best since here, the algorithm could identify much more clean peaks than for the two others. In addition as already seen in the spectrum in Figure 3.32, the PPC detector was not performing well, so only a simple calibration was possible here since no peaks above background could be identified. Reasons could be the limiting statistics, the exact position of the calibration source (which could not be determined exactly), or the reduced bias voltage and , therefore, the high leakage current. The bad performance of the PPC detectors in the setup will be investigated in future detector performance tests.
To determine the energy resolution, the FWHM of each identified energy peak was extracted. Because of the statistics, the peak function from Equation 3.30 was reduced to a simplified function of

$$f(E) = \sqrt{a \cdot E + b} \tag{3.36}$$

with a and b being fit parameters. The resulting energy resolution with the corresponding fit can be found in Figure 3.34 (the PPC detector is not included since no peaks have been identified) With the fitting parameter, the energy resolution at $Q_{\beta\beta}$-value at 2039.06 keV can be calculated resulting in values listed in Table 3.5 together with the measured resolutions for the same detectors in the post GERDA test before the LEGEND-200 setup [32]. The values clearly show a much worse performance with a factor of $\sim 2-3$ worse in the resolution at the $Q_{\beta\beta}$ value. The performance is very likely to originate from the high electronic noise which is disturbing the waveforms as seen in Figure 3.31. To reinforce this, Figure 3.35 shows the PoSD of all channels (c.f. Section 3.4.2.1).

It indicates high frequency noise around 2 MHz being one of the main noise sources disturbing the signals and leading to the poor energy resolution. Because the two DFE channels show no big noise arising in this range in contrast to all other channels, it hints that the noise is somehow disturbing into the HV cable line since only the detector channels and the LMFE of the second PPC which had no HV applied show this type of distortion in their PoSDs. This has to be

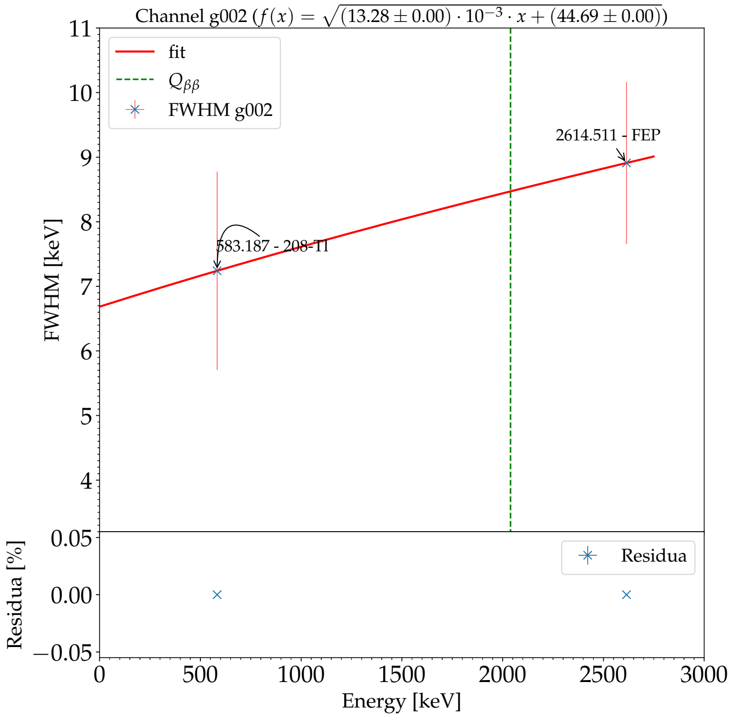

a) BEGe B00035B

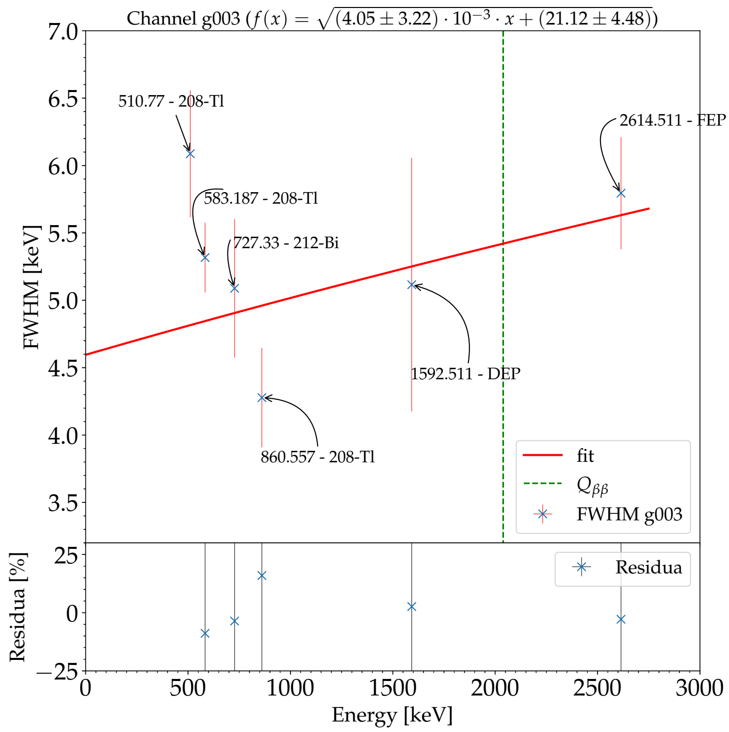

b) BEGe B00079B

Figure 3.34: Resulting energy resolution in terms of FWHM versus the energy of the 4 detector test for the two BEGe detectors. The data points are fitted with the fit function from Equation 3.36 while the resulting parameters are given in the title of each plot. The lower plot shows the residuals.

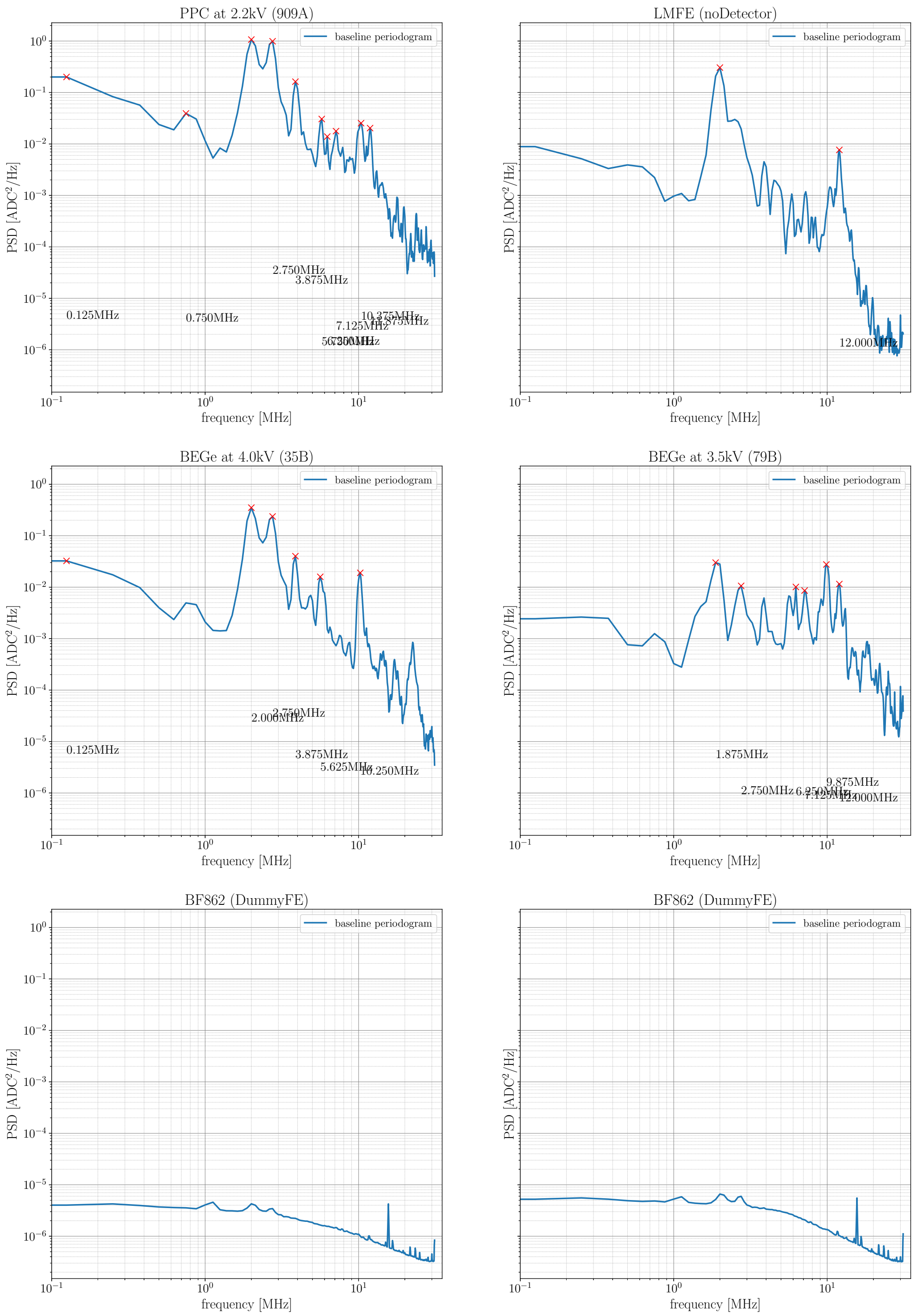

Figure 3.35: PoSD of all connected channels of the 4 detector test in the range between 0.1 MHz and 35 MHz where the PoSD wa s generated as explained in detail in Section 3.4.2.1. Dominant peaks are marked and labeled with their corresponding peak frequency.

investigated in future electronic campaigns to clearly determine the origin of the noise.
To further check, several stability plots for baseline, energy, etc. have been generated, which are illustrated in the Appendix for completeness.

Chapter 4

Development of Signal Readout Electronics for LEGEND-1000

4.1 Charge Sensitive Amplifier (CSA) for LEGEND-1000

In LEGEND-1000, the baseline design is a readout scheme based on state-of-the-art application-specific integrated circuit (ASIC) technology. ASIC technology allows to integrate the whole CSA into a single low-mass chip while achieving a huge miniaturization as illustrated in Figure 4.1. The main advantage for the $0\nu\beta\beta$ decay searches is that this configuration would allow achieving the ultimate noise performance. Since there is no need for a second stage further away from the detector such as the CC4 in LEGEND-200 (c.f. Section 3.3), the high amplification gain is already applied directly at the detector itself. In addition, the elimination of the second stage leads to faster rise times, and the whole circuit is less sensitive to external noise such as pick-up noise because no separate components and no cables between the components and the stages exist.

Moreover, another advantage could be a potential higher per-channel radiopurity. In principle, ASIC chips can be produced out of clean materials, which allows to place them very close to the detector. Furthermore, the miniaturization reduces the overall mass of the readout electronics, which facilitates low background level contributions to the overall background, and can enable much easier installation of the readout electronics since only the chip needs to be placed close to the detector. The elimination of the second stage could potentially reduce backgrounds due to reduced cables, too.

In principle, the readout ASIC for LEGEND-1000 challenges the same aspects as already explained in Section 3.1.2. The proximity to the detector enables an excellent noise performance and fast rise times which is crucial for the energy resolution and the PSD (c.f. Section 3.2). Furthermore, this includes a low threshold, a large dynamic range, low input and feedback capacitance,

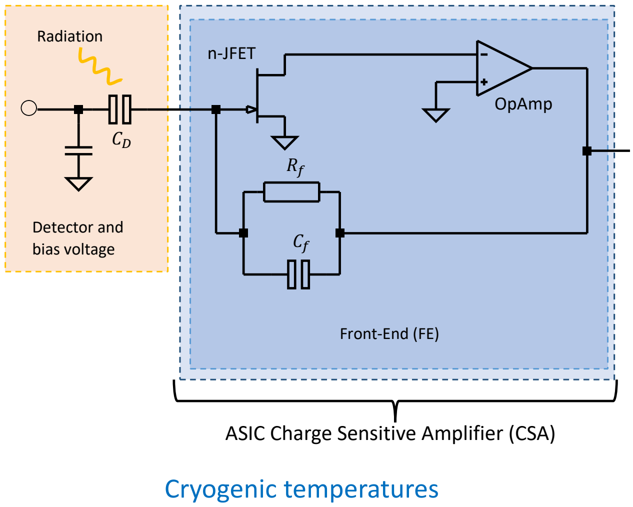

Figure 4.1: Example of a readout chain for HPGe detectors with a ASIC based CSA. By the use of the ASIC technology, it is possible to integrate the two stages used in LEGEND-200, consisting of the LMFE and the CC4 (c.f. Figure 3.8) into one single low-mass chip and achieving an excellent noise performance. The chip will just need one bias voltage while driving the signal differentially out of the cryostat without the need of second stage in between.

a sufficient bandwidth, small dimensions and mass, radiopure material and a clean production process, a differential signal output, functionality at cryogenic temperatures, robustness to electrostatic discharges and low power consumption. So far, commercially available ASIC chips are designed with a different objective that is focused on simplifying the ASIC design and not on the specific requirements of LEGEND (i.e., high radiopurity and a minimal number of cables). Therefore, they trade design complexity of the ASIC chip for additional power supply lines and external components, which is more cost-effective but less radiopure. Therefore, a CSA chip based on ASIC technology for LEGEND-1000 must avoid any external components with an on-chip low-dropout (LDO) regulator which can generate stable supply voltages even in the case where the ASIC chip draws more current and can potentially avoid power supply noise.

Figure 4.2 shows a rendering of the baseline design for LEGEND-1000 in the ideal setup: The chip is mounted on top of a ICPC detector, which is held by a PEN plate supported by rods made from ultra-pure copper. The ASIC chip itself is mounted on a long flex cable substrate which contains only one power supply line, one pulser line, and two signal cable lines.

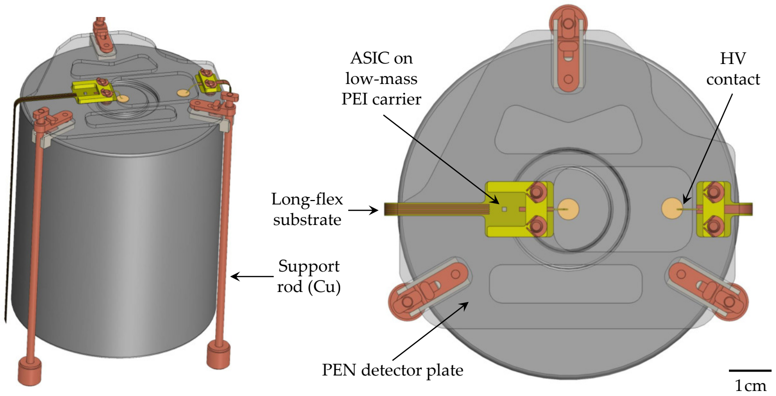

Figure 4.2: Preliminary design study of a LEGEND-1000 ICPC detetor with a ASIC based CSA readout on top of the detctor. The chip is located on a long-flex substrate and is connected to the p^+ contact of the detector by wire bonding. Ideally, the chip has only one power supply, two signal lines and one pulser line which add up to four individual cable lines on the flex cable. The detector is mounted on a PEN plate and hold by support rods made from ultra-pure copper. Renderings provided by M. Busch.

4.1.1 Application-specific integrated circuit (ASIC) technology

Traditionally, the CSA in a HPGe readout system is based on a JFET in the front-end (c.f. Figure 3.1). A MOSFET is also a field effective transistor with a similar operating principle with a gate that is electrically insulated from the drain-source channel by a thin layer of metal oxide and, therefore, higher input impedance [89]. MOSFETs are typically used to design a integrated circuit (IC) realized using so-called complementary metal-oxide semiconductor (CMOS) technology. CMOS technology is a type of fabrication process for IC and is characterized by the complementary use of n- and p-type MOSFETs in s single substrate. While CMOS technology is mainly used in digital electronics applications, it has nowadays also great importance in analog electronics because it has low electronic noise levels, low power consumption, and high speeds [102]. It is characterized by the size of the transistors with typical values of 250 nm, 180 nm or 65 nm. Smaller transistors require lower power consumption, higher speeds, and need less space, but can handle lower supply voltages and hence lower dynamic range without affecting electronic noise. However, smaller transistors also increase production costs, wherefore typically a trade-off has to be found for the used technology [67]. ASICs are chips designed and fabricated by CMOS technology and characterized by being ICs custom-designed for a particular use rather than a general-purpose. The development process is based on circuit simulations and prototype production in several design cycles and prototype versions before producing a final chip. In contrast to digital ASICs, analog ASIC cannot be controlled from outside and are limited in flexibility, but have no digital noise from switching clock devices and feature high reliability.

4.1.2 Status and overview

In the past, several attempts for the design of a ASIC based readout system for HPGe detectors have been undertaken. The main problems arised to be the integration of a proper continous RC-feedback loop with decay times $\mathcal{O}(100\,\mu s)$ as desired for LEGEND. In IC, the use of high ohmic resistors with high linear characteristics over the whole dynamic range is not as trivial as for analog circuits such as e.g. for the LMFE (c.f. Section 3.3). In the past, several publications have tried to realize feedback loops using various IC techniques as e.g. in GERDA with a substrate isolated nMOSFET operating in the subthreshold area without achieving the stability and linearity requirements for LEGEND especially at cryogenic temperatures [103].
Recently, a commercially available CUBE ASIC from XGLab SRL, a single-channel low-noise CSA based on CMOS technology was tested together with a HPGe detector [81]. It could be shown that the CUBE ASIC features very low electronic noise with minimal baseline noise of 655 eV FWHM obtained at a filter rise time of 4 µs as illustrated in Figure 4.3. In addition, the chip showed very good energy resolution of 2.3 keV FWHM at the $Q_{\beta\beta}$ of ^{76}Ge and very good PSD performance with highly reliable cuts on the SEP and FEP [81]. Moreover, radiopurity measurements performed by direct gamma counting, ICP-MS, and radon emanation techniques have shown that the chip already fulfills the very stringent background limitations for LEGEND-1000 [63, 81]. However, several disadvantages remain for the CUBE ASIC: most important, the chip does not include a continuous feedback circuit with a high ohmic resistor R_F but instead uses a pulsed reset capacitor where an external logic signal discharges the capacity. This is not appropriate for LEGEND-1000: the experiment will have more than 400 individual channels of HPGe detectors to achieve the overall mass of 1 t. If now the readout electronics is based on ASIC technology with pulsed reset, all 400 channels need to reset simultaneously since otherwise no coincidence cuts between the detectors can be applied. The reset time would mainly be driven by the detector with the highest leakage current in low rate physics runs, which will lead to high detector dead times in which no events will be recognized by the whole detector array. Longer dead times generally need longer overall measurement times to achieve the same exposure as for shorter dead times. In addition, the CUBE ASIC is not optimized for

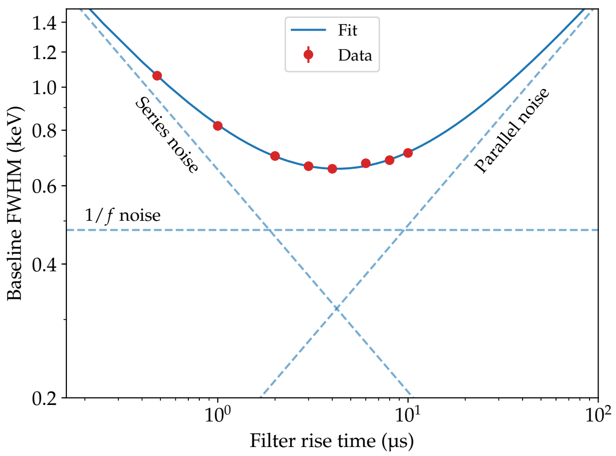

Figure 4.3: Baseline noise performance of the CUBE ASIC with the PONaMa1 HPGe PPC detector. A minimum baseline noise of 655 eV baseline FWHM was obtained at a filter rise time of 4 µs . The dashed lines in the plot correspond to the series (down-sloping), parallel (up-sloping), and 1/f (horizontal) noise contributions. Figure and caption taken from [32, 81].

highest detector capacitances since it was originally designed for a low capacity silicon drift detector and can therefore not handle the ICPC detectors with a higher capacity, which are the LEGEND-1000 baseline design [81]. Moreover, the CUBE ASIC has a large number of external components on a separate bias board with the need of several external supply voltages and no internal LDO. Last but not least, it cannot drive differential signals over ranges of $\mathcal{O}(10\,\mathrm{m})$ which is needed to get signals out of the cryostat to the DAQ.

4.2 The LEGEND 1000 Berkeley ASIC (LBNL ASIC)

4.2.1 Overview

The LBNL LEGEND-1000 ASIC is a single-channel low-noise CSA based on 180 nm CMOS technology. The chip is currently developed at LBNL where chiplet 5 was avalibale at TUM for extensive testing during the summer 2021. Chiplet 5 was produced as $1\,\mathrm{mm} \times 1\,\mathrm{mm} \times 8\,\mu\mathrm{m}$ die together with a testing PCB. Figure 4.4 shows a close-up of the chip and the PCB. The chip was designed to achieve baseline noise levels of $\sim 20\,e^-$ RMS and a threshold of $< 1\,\mathrm{keV}$ with a dynamic range up to $\sim 10\,\mathrm{MeV}$ and contains a feedback capacitance of $C_f \approx 500\,\mathrm{fF}$.

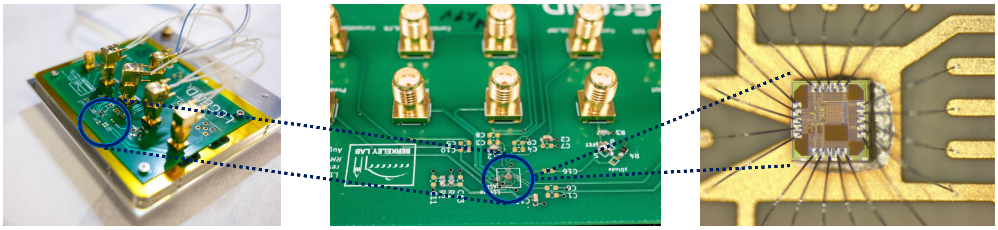

Figure 4.4: Close-up of the LBNL ASIC prototype chiplet 5 for LEGEND-1000. The chip (right) is connected to the traces on a testing board (middle) via special wire bonds. The board contains the bypass capacitor for the main supply voltage and several SMA connectors for signal outputs, pulser input and power supply.

Signal rise times of $\mathcal{O}(10\,\mathrm{ns})$ are the design goal resulting in a bandwidth of $20-50\,\mathrm{MHz}$. It is optimized for detector capacities of $1.0 \leq C_D \leq 5\,\mathrm{pF}$ and it can drive signals differentially over cables with $\mathcal{O}(10\,\mathrm{m})$ with characteristic impedance of $50\,\Omega$. In the final design, it should contain a LDO regulator providing a single 1.9 V supply voltage. However, the chiplet 5 still needs bypass capacitors on the test board to generate stable power supply while it already needs only one power input signal of $V_{DD} = 1.9\,\mathrm{V}$ and a ground connection $V_{SSA} = 0\,\mathrm{V}$. A common mode voltage of $V_{CM} = \frac{V_{DD}}{2}$ is generated together with all bias currents needed for the device: The input stage of the CSA needs a current of $I_{INP} = 8\,\mathrm{mA}$, the casode stage (second CSA) which controlls linearity and dynmaic range needs $I_{CAS} = 0.5\,\mathrm{mA}$ while the feedback stage which discharges the feedback capacity C_f requires a bias current of $I_{FB} = 100\,\mathrm{pA}$. The buffer stage controls the single-to-differential input, DC-level gain and bandwidth and needs a bias current of $I_{BUF} = 1\,\mathrm{mA}$ with a bias current of $I_{S2D} = 30\,\mathrm{\mu A}$ of the differential driver at the end of the circuit. The board contains a pulser capacity made from a stray capacitance between the traces on the board of $C_P \approx 22\,\mathrm{pF}$ to test the chip with pulser input signals.

4.2.2 Measurement setup

The chip was extensively tested during summer 2021 in three different measurement campaigns:

1. The first measurement has been performed at room temperature where the testing board was installed in an aluminum box to reduce the electronic noise (in the following referred to as **room temperature**). An arbitrary waveform generator (Keysight 33522B Series) was used for the generation of input signals in the form of square waves with different

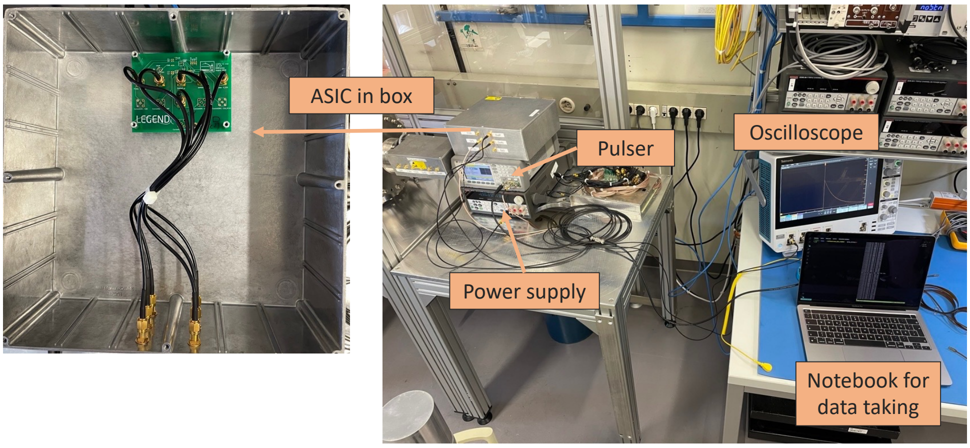

Figure 4.5: Overview of the measurement setup at room temperature. The LBNL ASIC on the testing board is contained in aluminium box (left) while pulsed with the pulser with arbirtray square waves. The power supply generates the 1.9 V supply voltage for the board while data is taken with the oscilloscope which stores the data on a notebook.

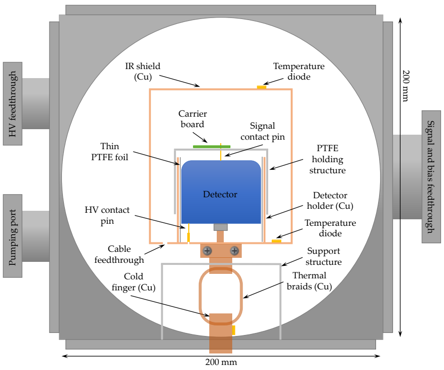

a) Simplified sectional view of the CUBE^3 cryostat

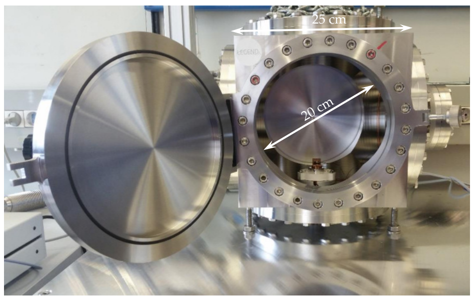

b) LBNL ASIC in the CUBE^3 cryostat.

Figure 4.6: Simplified sectional view (left) of the CUBE^3 cryostat together with the measurement setup for the LBNL ASIC (left). Since no detector was installed, the PCB hosting the chip was mounted into a copper box to allow thermal coupling and then placed inside the cryostat. All cables have been feed through the signal feedthrough on the right with ribbon cables. Simplified sectional view from [32].

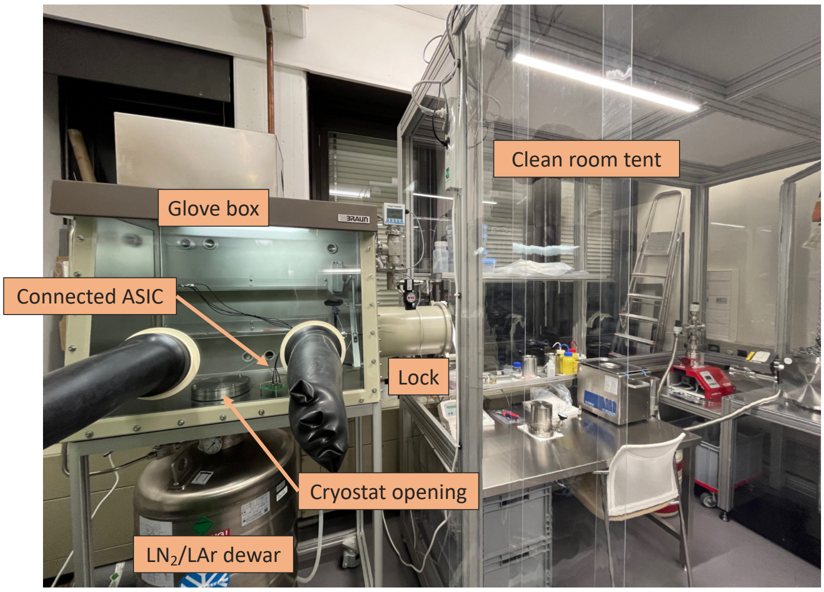

Figure 4.7: The TUM electronics and detector test stand: the glove box contains a cryostat which can be filled with LN_2 or LAr from the outside and several flanges as feedthrough to connect signal and supply cables the same way as for the warm setup. The glove box itself is pressurized with nitrogen and contains a lock to bring parts in after pressurizing. The lock opening goes into a cleanroom tent where the preassembly of the electronics can be done.

rising edges of $\mathcal{O}(10\,\mathrm{ns})$, pulse width of 10 ms, frequency of 50 Hz and an input termination of 50 Ω while the power was supplied by a standard power supply (Keithley 2230-30-1 DC) at 1.9 V. The output signals of the positive and negative output have then been acquired with an oscilloscope (Tektronix MSO4 4 Series) which stores the raw waveform data of the positive and negative outputs (CH1 + CH2) of the differential signal in a CSV format on disk while providing DC coupling with 1 MΩ termination. The scope was set to sample at $62.5\,\mathrm{MS\,s^{-1}}$ with 12-bit vertical resolution and the full bandwidth of 350 MHz while triggering on the clock signal provided by the waveform generator. The analysis was performed offline using PYTHON. Figure 4.5 shows a image of the setup.

2. A second measurement was performed in a vacuum cryostat with residual pressure of $p = 2.3 \times 10^{-6}$ mbar and residual temperature of $\sim 84\,\mathrm{K}$ (in the following referred to as **vacuum and cold**). The CUBE^3 setup was built at TUM during the measurement campaign for the CUBE ASIC and is shown in Figure 4.6 [81]. The ASIC is mounted in a copper box

with signal and supply cables going through a hole in the copper box. The CUBE[3] cryostat is made from stainless steel with a quick lock door for easy access (c.f. Figure 4.6b) with additional feedthrough flanges at the outsides. The cables are fed through the signal flange on the right outside of the cryostat, where they connect to scope, supply and pulser in the same way as for the setup at room temperature. The copper box is thermally coupled to a cold finger which is inserted into a LN_2 dewar. The cryostat is evacuated with a pumping unit (Pfeiffer HiCUBE 80) consisting of a diaphragm forepump and a tubromolecular pump (TMP). The temperature of the setup was monitored using three temperature diodes (Lake Shore DT-670). During data taking, the vacuum valve between the TMP and the cryostat was closed, and the pump switched off to avoid microphonic noise.

3. The third measurement was performed in a small custom-designed electronic and detector test stand with a LN_2 dewar inside a glove box which is shown in Figure 4.7 (in the following referred to as **liquid nitrogen**). The opening of the dewar is 150 mm and has been designed to insert different types of electronics and detectors into the LN_2 volume. The glove box contains different feedthrough flanges for signal and supply cables which have been connected outside the same way as for the room temperature setup. The box is purged with boil-off nitrogen from the LN_2 dewar and constantly held at an overpressure of 5 mbar to prevent ingress of oxygen, humidty and dust. A residual oxygen concentration of as low as 100 ppm can be achieved after ~ 1 d of purging. Furthermore, it contains a lock system which can be pressurized with nitrogen by a gate walve to smoothly insert parts into the box from outside. The opening of the lock ends in a clean room tent where electronics, cables etc. can be prepared before inserting into the box. The system was designed and built for fast testing of different electronics such as the LBNL ASIC in a highly adaptable system.

4.2.3 First measurement results

Figure 4.8 shows an example of the waveform data taken by the setup at room temperature for different pulser input voltages with a pulser rising edge of 10 ns. At a first look, the waveform data shows clean shapes with equal intervals for each input interval step and decaying tail of $\sim 10\,\mu s$. The rising edge shows a fast rise with small disturbances due to relfections in the system. However, in contrast to the LEGEND-200 waveforms, the waveforms feature a linearly decaying tail that levels off exponentially. The properties of this special decaying tail is explained in detail in Section 4.2.4. To further test the linearity of the ASIC, Figure 4.9 shows the input voltages of the pulser V_{in} versus the output voltage of the chip which refers to the maximum signal amplitude V_{out}. The system features high linearity over the whole dynamic range tested in the warm measurement setup. At small input voltages, there is a small deviation from the linear behavior, which increases with decreasing input voltage. To illustrate in Figure 4.9, a linear fit for all data points without small input voltages was performed to present the amount of deviation in a graphical way. Since the input voltage refers to the energy which would be deposited in a HPGe readout system, the system would not feature linear behavior at small energy windows, which should be avoided for LEGEND because, on the one hand, peaks at lower energies exist, which are needed for calibration measurements and on the other hand, probably other searches for BSM physics could be performed at these low energies with the LEGEND-1000 detector array [63]. It should be mentioned that these non-linearities could maybe be eliminated by adjusting the bias currents of the ASIC which would need further iterations and simulations of the chip design [32].

Another important key feature of CSA designs is the need for fast signal rise times. To measure this, rise time measurements for different input voltages have been performed where the rise time was determined at each voltage step for one hundred waveforms and then averaged to account for possible disturbances due to reflections. An example for rise time extraction of single waveforms at three different voltage steps are shown in Figure 4.10 where the full example of all voltage steps can be found in the Appendix. Here, the rise time is always determined by the time it takes for the waveform to rise from 10% to 90% maximum amplitude.

Figure 4.11a shows the so extracted rise times plotted versus the corresponding input voltage. The LBNL ASIC features a fast rise time from 10% to 90% maximum signal of $< 40\,\mathrm{ns}$ for all input voltages. In general, the rise time for pulser measurements is limited by the rising edge of the pulser itself, which was set manually to 40 ns. As seen in Figure 4.11, the rise time depends linearly on the input voltage with a slope of $-2.96\,\mathrm{ns\,kV^{-1}}$. Since the rising edge of the pulser was fixed to 40 ns for all input voltages independently of the input voltage, this is a real feature of the ASIC itself. In LEGEND-1000, the baseline design proposes the sole use of the larger ICPC detectors. In ICPC detectors drift path-dependent charge trapping (CT) can worsen the energy resolution considerably. As shown in recent analysis studies, the charge trapping can be identified by the correlation of the drift time and the energy, with drift time being the time from the start of the waveform edge to 90% maximum amplitude [104]. If the rise time (and therefore drift time) now depends on

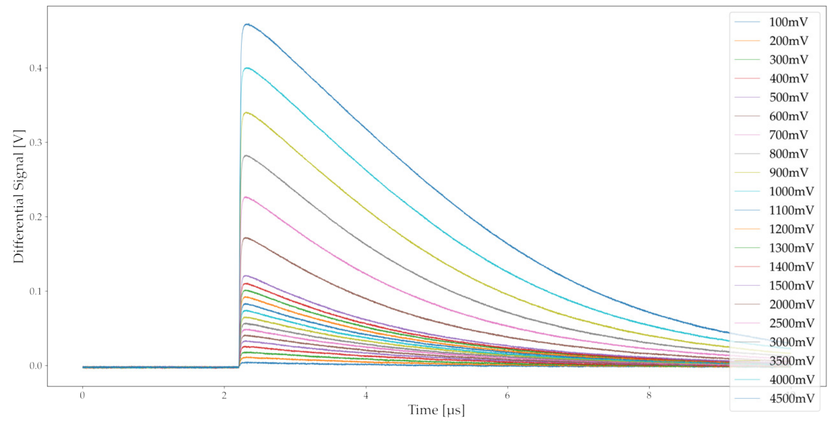

a) Full waveform

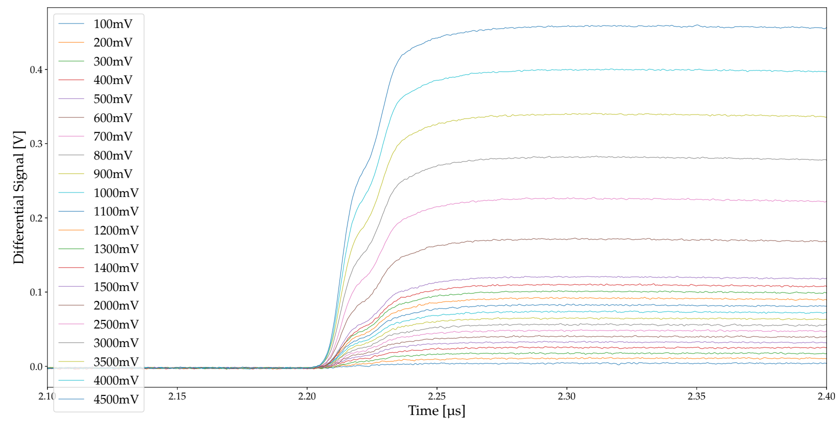

b) Rising Edge

Figure 4.8: Waveform examples obtained with the LBNL ASIC at room temperature for different pulser input voltages with a rising edge of 10 ns. The differential signal is generated by substracting the signals from the positive and negative output (CH1 + CH2) to get an overall positive signal. The right plot shows a zoom on the leading edge which features a fast rise time.

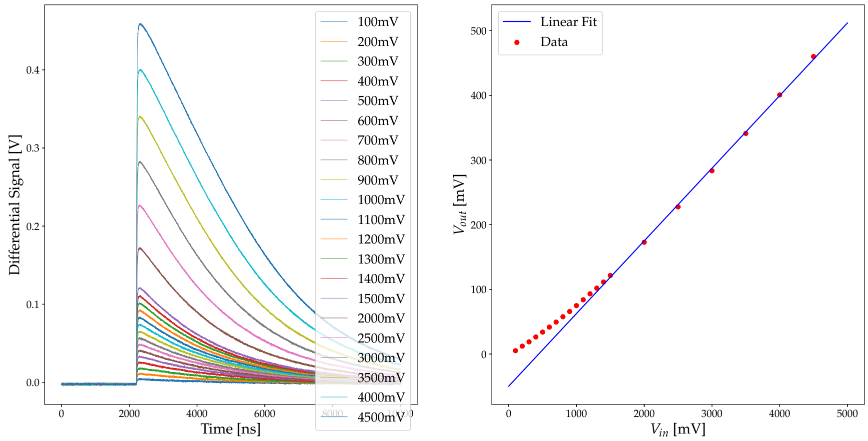

Figure 4.9: Waveforms obtained with the LBNL ASIC for varying input voltages (left) with a rising edge of 10 ns at room temperature. The system linearity (right) is determined by plotting the different input voltages of the pulser V_{in} versus the output voltage of the chip, which refers to the maximum signal amplitude V_{out}. Then, a linear fit for these data points is performed while the data points at small input voltages are excluded.

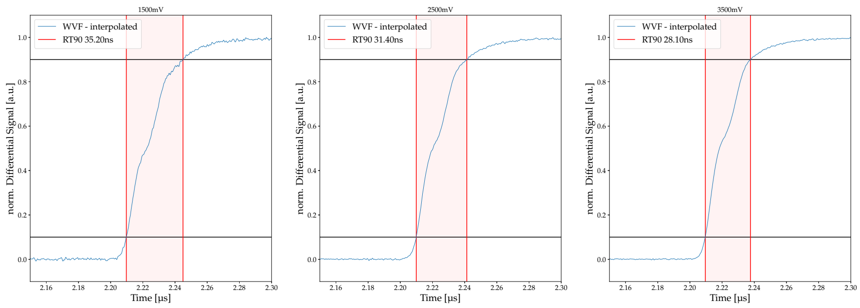

Figure 4.10: Example of rise time extraction of single waveforms at three different input voltages with rising edge 40 ns at room temperature. The rise time is measured as the time the waveforms take to rise from 10% to 90% maximum height (red area).

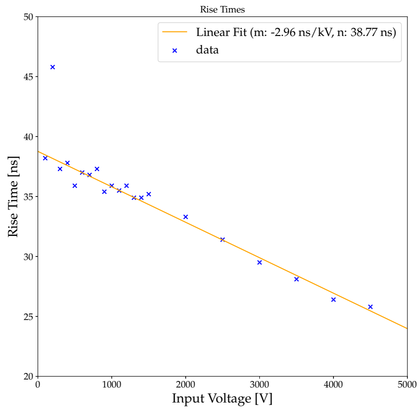

a) Room temperature (pulser rising edge 40 ns)

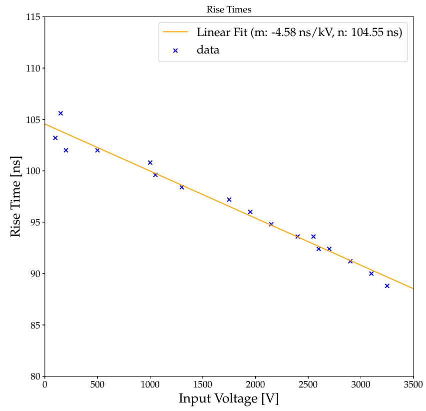

b) Vacuum and cold (pulser rising edge 45 ns)

Figure 4.11: Rise time versus input voltage for different pulser input voltages for the room temperature and vacuum and cold setup. To present the linear dependency, a linear fit of the form $f(x) = m \cdot x + n$ was performed for all data points where the fitting results are shown in the legend.

the energy, this would make the application of this analysis procedure much worse also because of non-linearities introduced by the CSA. Furthermore, other analysis routines that deal with the rise time as input variable would be disturbed. It should be mentioned that, in principle, a correction of a clear linear dependency would be possible but would at least impair the results compared to non-dependent rise times from other CSAs.

To compare with the room temperature measurements, Figure 4.12 shows an example of the waveforms obtained with the vacuum and cold measurement setup. In this setup, the rising edge of the pulser has been slightly increased to 45 ns since this leads to a minimum of disturbing oscillations on top of the waveforms. Since the CUBE^3 setup has a flange with a transition from the cryostat to the laboratory; reflections at this flange can lead to distortions on the waveforms, which depend on the frequency of the input signal and, therefore, the rising edge. At a first look, the waveforms show a much longer decay tail with the same features as for the room temperature measurement, which is expected since the values of resistors, capacitors, etc. change with temperature. In addition, the waveforms show a small undershoot and overshoot at the leading edge (c.f. Figure 4.13 for the individual channels). In terms of linearity, the behavior is unchanged as Figure 4.12 illustrated. The linearity shows small

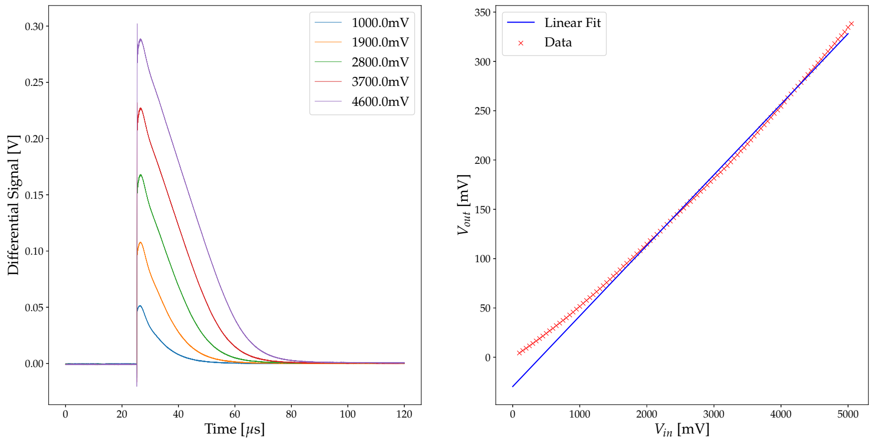

Figure 4.12: Waveforms obtained with the LBNL ASIC for varying input voltages (left) with a rising edge of 40 ns for the vacuum and cold measurement. The system linearity (right) is determined by plotting the different input voltages of the pulser V_{in} versus the output voltage of the chip, which refers to the maximum signal amplitude V_{out}. Then, a linear fit for these data points is performed while the data points at small input voltages are excluded.

deviations at lower input voltages. In addition, the data points have small deviations from the linear fit, with some regions being tiny below the line and others being tiny above the fit line. Concerning rise times, Figure 4.11b shows the rise times versus input voltage which have been acquired the same way as for the measurement performed at room temperature. Compared to room temperature measurements (c.f. Figure 4.11a), the rise times are overall much longer. The longer signal rise times are very likely related to the lower temperature. The resulting of the signal leads to rise times from 10% to 90% maximum signal of $< 105\,\text{ns}$ which is in still in the desired range of $\mathcal{O}(100\,\text{ns})$. In addition, the same linear dependency of the rise time from the input voltage can be found with a slightly higher slope of $-4.58\,\text{ns}\,\text{kV}^{-1}$.

Concering the channel integrity for the positive and negative output of the differential signal, Figure 4.13 shows the output of the single positive and negative channels for different input voltages of the warm and vacuum and cold setup. As Figure 4.13a shows for the data at room temperature, both channels feature the same leading-edge shape without any over- and undershoot. In contrast, Figure 4.13b illustrates a different behavior for the vacuum and cold setup where both channels show overshoot at the end of the leading edge, but

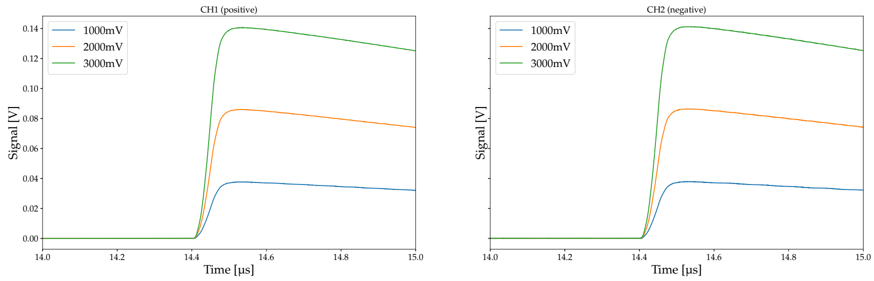

a) Room temperature (pulser rising edge 40 ns)

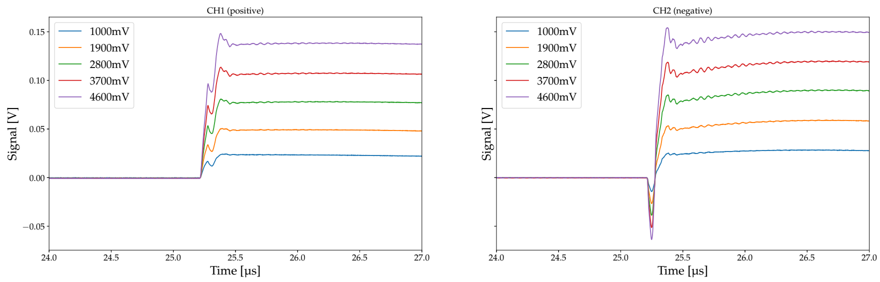

b) Vacuum and cold (pulser rising edge 45 ns)

Figure 4.13: Waveforms of the single positive and negative output channel of the LBNL ASIC at different input volages for the room temperature and vacuum and cold setup. The negative output channel CH2 has been inverted for better illustration.

only the negative output CH2 features a clear and huge undershoot. The ringing and the disturbing oscillations on the waveforms are the same, while only the positive channel shows ringing in the leading edge. The ringing in the leading edge of the negative channel seems to be coincident with the undershoot.

4.2.4 Pole-zero correction

As already mentioned and shown in the previous section, the decay tail of the LBNL ASIC has a quite different behaviour compared to normal CSAs such as in LEGEND-200. To understand the origin of this particular shape, Figure 4.14 illustrates a simplified layout of the ASIC circuit. Instead of using the traditional layout with a feedback resistor R_f and a feedback capacitor C_f in parallel, the feedback loop consists of a feedback capacitor C_f and a nMOSFET in parallel since the use of high ohmic resistors in a ASIC design layout is not simply possible. The nMOSFET is a special type of transistor that features, in principle, three types of operation, which can are represented by the voltage

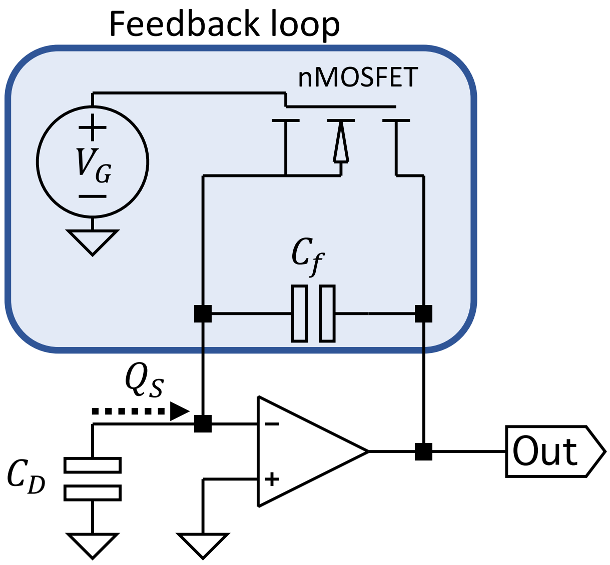

Figure 4.14: Simplified effective circuit layout of the LBNL ASIC. Instead of a feedback loop with a feedback resistor R_f and a feedback capacitor C_f in parallel, the ASIC design consists of a feedback capaciy C_f and a nMOSFET in parallel

between gate and source V_{GS}, the voltage between drain and source V_{DS} and the threshold voltage V_{th}:

- In the cutoff or subthreshold region where the gate-source voltage is below the threshold voltage $V_{GS} < V_{th}$, the transistor is turned-off and no conduction between drain source exists despite from small subthreshold currents due to thermal energy of the electrons.

- In the triode or linear mode where $V_{GS} > V_{th}$ and $V_{DS} < V_{GS} - V_{th}$, an inversion channel is created from source to drain (c.f. Figure 4.15 (a)) so that a small current I_{DS} flows from the drain to the source. This current can be modelled as [105]

$$\begin{aligned} I_{DS} =& \mu_n C_{ox} \frac{W}{L} \left[(V_{GS} - Vth) \cdot V_{DS} - \frac{{V_{DS}}^2}{2}) \right] (1 + \lambda \cdot V_{DS}) \\ \overset{\lambda \cdot V_{DS} \ll 1}{\approx} & \mu_n C_{ox} \frac{W}{L} \left[(V_{GS} - Vth) \cdot V_{DS} - \frac{{V_{DS}}^2}{2}) \right] \end{aligned} \tag{4.1}$$

with μ_n the charge-carrier mobility, W and L the gate width and length, C_{ox} the gate oxide capacitance per unit area and λ the channel length

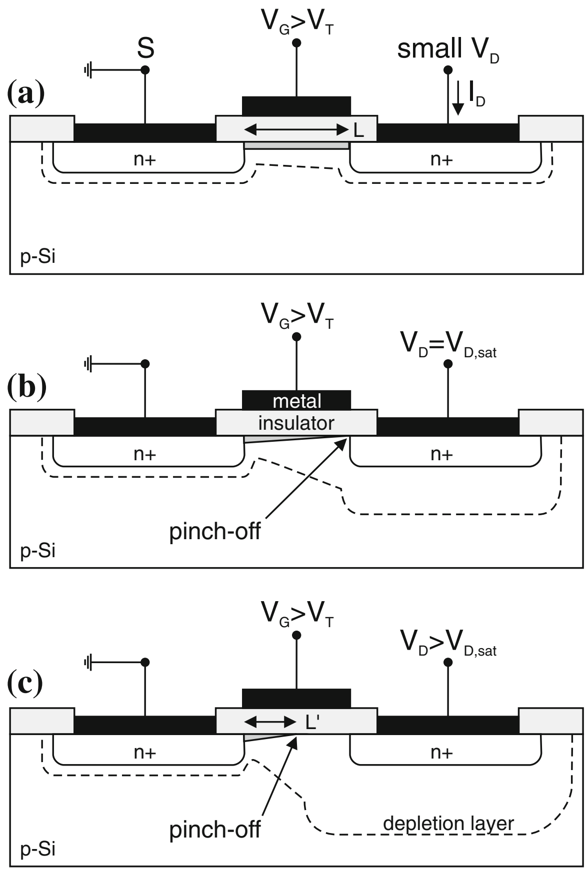

Figure 4.15: Operation principle of a nMOSFET in: triode or linear (ohmic) mode (a), saturated or active mode at the onset of pinch-off (b) and saturated or active mode beyond pinch-off (c). Figure from [102].

modulation parameter. Because in a first approximation the drain source current is proportional to the drain source voltage, the MOSFET acts as a resistor.

- If the drain source voltage further increases, the transistor reaches the saturated region where $V_{GS} > V_{th}$ and $V_{DS} \geq V_{GS} - V_{th}$. At the so-called pinch-off (c.f. Figure 4.15 (b)), the inversion channel length becomes zero and furhter shortened by increasing drain source voltage. The current is

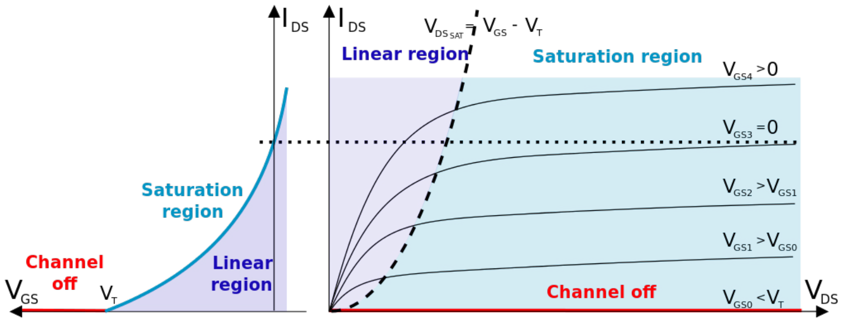

Figure 4.16: Drain source current I_{DS} versus drain source voltage V_{DS} for a nMOSFET. The gate-source voltage sets the pinch-off voltage at which the transition between the linear region to the saturated region takes place and the drain-source current I_{DS} is maxed out. Figure from [106]

therefore maxed out which can be modelled by [105]

$$\begin{aligned} I_{DS} &= \frac{\mu_n C_{ox}}{2}\frac{W}{L}[V_{GS} - Vth]^2[1 + \lambda \cdot (V_{DS} - V_{DSat})] \\ &\overset{\lambda \ll 1}{\approx} \frac{\mu_n C_{ox}}{2}\frac{W}{L}[V_{GS} - Vth]^2 \end{aligned} \tag{4.2}$$

with V_{DSat} being the drain source voltage at the pinch-off.

Graphically, this behaviour leads to a special characteristic curve for the dependency of the drain source current I_{DS} from the drain source voltage V_{DS} which is illustrated in Figure 4.16. The Figure shows already by eye that the regions and therefore the Equations 4.2 and 4.1 are only approximations without concerning the transition areas between the different regions where this approximation no longer holds. Coming back to LBNL ASIC, if now a voltage pulse enters the circuit, the MOSFET reacts according to the behaviour from Figure 4.16 in the RC-circuit configuration shown in Figure 4.14 with the saturation voltage set by the gate-source voltage V_{GS}. If the input voltage is higher than the saturation voltage V_{DSat}, the MOSFET is in the saturated region and the current I_{DS} is maxed out so one can calculate the response of the RC-circuit to

$$
\begin{aligned}
I_{DS} &= -\frac{\mathrm{d}Q_{DS}}{\mathrm{d}t} = -C_f\frac{\mathrm{d}V_{DS}}{\mathrm{d}t} \quad \text{with } Q = C_f \cdot V_{DS} & (4.3)\\
\Rightarrow V_{DS}(t) &= -\frac{1}{C_f I_{DS}} \cdot t + V_{DS,0} & \\
&= k \cdot t + V_{DS,0} \qquad \text{using Eq. 4.2} & (4.4)\\
\text{with } k &= \frac{2C_f}{\mu_n C_{ox}}\frac{L}{W}\frac{W}{L}[V_{GS} - Vth]^{-2} &
\end{aligned}
$$

with $V_{DS,0}$ being a integration constant. Following this, the circuit response of the ASIC in the saturated region is a linear function of the time. On the other hand, if the voltage is below the saturation voltage V_{DSat}, the MOSFET is in the linear region and acts as a resistor with resistance R_{DS} which can calculated with Equation 4.1 to

$$
R_{DS} = \frac{V_{DS}}{I_{DS}} = \beta \cdot \frac{1}{V_{GS} - V_{th} - V_{DS}/2} \quad \text{with } \beta = \frac{1}{\mu_n C_{ox}}\frac{L}{W} \tag{4.5}
$$

With this effective resistance R_{DS}, the response of the RC-circuit can be calculated by using the same RC-circuit discharge formula from Equation 4.3

$$
\frac{\mathrm{d}V_{DS}}{\mathrm{d}t} = -\frac{I_{DS}}{C_f} = -\frac{1}{\beta C_f}\left[(V_{GS} - Vth) \cdot V_{DS} - \frac{{V_{DS}}^2}{2})\right] \tag{4.6}
$$

$$
\Rightarrow V_{DS}(t) = -2(V_{GS} - V_{th})\left[1 - \exp\left(\frac{V_{GS} - V_{th}}{\beta C_f}t - V'_{DS,0}\right)\right]^{-1} \tag{4.7}
$$

with $V'_{DS,0}$ being a integration constant. Following this, the circuit response of the the ASIC in the linear region is a exponential decay.
Figure 4.17 illustrates this behaviour for an example of three different input voltages. If the whole waveform stays below the saturation voltage (left plot) which is shown as green dashed line and equal for all waveforms, the MOSFET only operates in the linear region (pink area) and reacts according to Equation 4.7 with a exponential decay which can be fitted with a simple exponential function in approximation. If the waveform rises above the saturation voltage (middle and right plot), the behaviour changes: as long as V_{DS} and therefore the voltage in the circuit is above the saturation voltage, the current in the MOSFET is maxed out and the circuit reacts in the saturated region with a linear function according to Equation 4.4 which is fitted with a linear function in the purple area. As soon as the waveform crosses the saturation voltage, the behaviour changes again back to the exponential decay since the MOSFET then goes back into the linear region. From a analysis point of view, the saturation

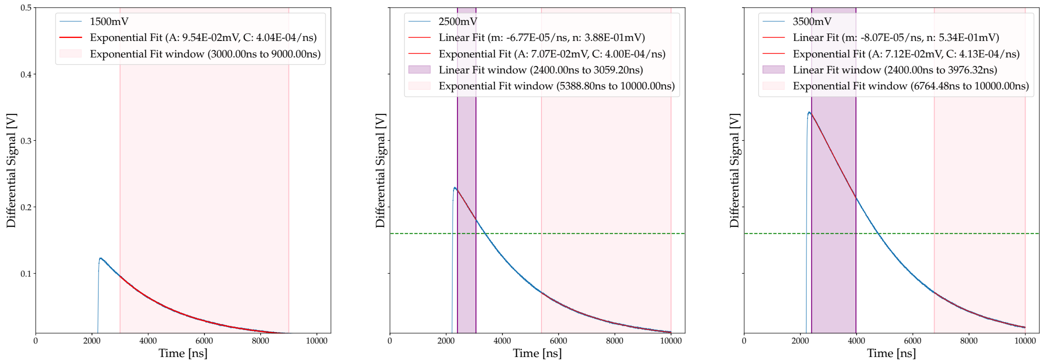

Figure 4.17: Waveforms of the LBNL ASIC at room temperature for three different input voltages with the corresponding linear and exponential decay regions. The regions are divided by the saturation voltage of the MOSFET (green dashed line). Above the saturation voltage, the tail behaves linear, below exponential. The fitting parameters of a simple linear and exponential fit in the corresponding region are shown in the legend.

voltage in Figure 4.17 could be generated by setting a cut as soon as the slope of the first part of the decay changes by applying this method to many waveforms. Then, two regions are generated by splitting the decay tail according to the saturation voltage with a 10% puffer area around the saturation voltage and the highest point of the leading edge to avoid the special MOSFET behaviour at very high voltages where the approximation of $\lambda \cdot V_{DS} \ll 1$ no longer holds and the transisition region between saturated and linear region where the behaviour cannot straightforward be calculated with the methods explained above.

Because this behavior and its corresponding decay tail is a non-linear behavior (the shape of the decay tail changes with the amplitude of the input pulse), it causes problems in the analysis routine, which will be explained in the following. In the LEGEND analysis, the first step after baseline subtraction is the so-called pole-zero correction of the waveform. In terms of electronics, the CSA acts as linear time-invariant (LTI) system, which is a system that produce output signals $y(t)$ always by a convolution of the input signal $x(t)$ with the impulse response of the system $h(t)$

$$y(t) = x(t) \circledast h(t) \tag{4.8}$$

Because CSAs normally feature a clear exponential decay which has a constant decay time for all waveforms, the impulse response of the RC-circuit is known and can be used to deconvolute the actual signal of the corresponding event out of the output signal of the CSA which contains the convolution with the RC-feedback loop impulse response. This can be performed by using a moving

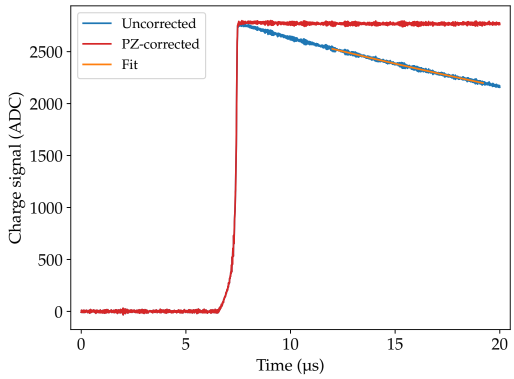

Figure 4.18: Pole-zero corrected waveform for an example waveform of LEGEND-200: An exponential function is fitted to the decay tail after which the recursive function from Equation 4.9 is applied to achieve the deconvolution with the help of an IIR filter. Figure from [32]

window Deconvolution (MWD) which results in the recursive formula [101]

$$y[n] = y[n-1] + x[n] - e^{-\frac{T}{\tau}} x[n-1] \tag{4.9}$$

with $y[n]$ the deconvoluted signal in discrete samples, $x[n]$ the original signal, T the sampling time and $\tau = \frac{1}{R_f C_f}$ the decay time constant. Equation 4.9 can be transferred into an IIR filter, which can be applied to the waveforms by fitting an exponential function to the decay tail and extracting the decay time after which the filter is applied. This is shown for a typical LEGEND-200 waveform with normal RC-feedback loop in Figure 4.18. This method is called pole-zero correction since it corrects for the pole introduced by the exponential decay coming from the RC-feedback loop in the transfer function of the CSA. The deconvolution is a crucial part of the processing since the deconvoluted waveforms are input to all further analysis routines in the current analysis procedure, such as for example the the trapezoidal shaping for energy and current extraction as well as several analysis cuts for delayed charge recovery or the charge trapping correction already mentioned. Most of these routines use differences in the slope of the flat top after pole-zero correction or need the flat top for integration of the tail for parameter extraction [32].
Coming back to LBNL ASIC, an analytical impulse response function $h(t)$ is almost impossible to find. As explained above, MOSFET behavior can be modelled in the linear and saturated region in approximation, but an impulse response function would require accurate and detailed knowledge of the exact behavior also in the transition regions around the saturation voltage as well as

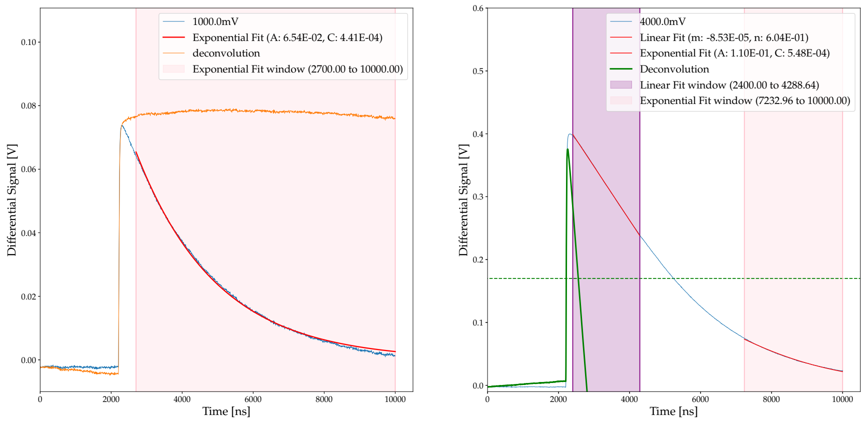

Figure 4.19: Pole-zero correction for two waveform of the LBNL ASIC at room temperature. The green dashed line indicates the saturation voltage, while the pink area refers to the linear region and the purple area to the saturated one. The deconvoluted waveforms are shown as orange (left plot) and green (right plot) curves.

for very high voltages .[1] Figure 4.19 shows an example of a pole-zero correction for two waveforms at room temperature. The right plot shows a waveform that exceeds the saturation voltage to fit both regions. Because no full analytical $h(t)$ exists, which could be used in an approximation for a similar kind of deconvolution, the pole-zero correction fails, which is shown by the green curve, which is the correction with the decay time extracted from the exponential tail at the end of the curve. On the other hand, the left plot shows a waveform that is only acting in the linear region below the saturation voltage. Here, a simple exponential fit was performed and the decay time was extracted, which was then used to deconvolute the waveform with the same IIR filter as in Figure 4.18. The deconvoluted waveform is shown as the orange curve. It can be seen already that also for this region, the approximation of exponential decay (and therefore the MOSFET operating in perfectly in the linear region) is not precise enough so that the flat top is not flat at all and also the baseline features a slope after deconvolution. This comes from the fact that MOSFETs are no linear devices like resistors so that all the behavior analyzed before

[1] It should be mentioned that such response function could in principle be generated by using exact MOSFET models like in [107]. However, they contain a huge number of free parameters which would need to be fitted accurately for every waveform and have model problems at cryogenic temperature.

does not hold in the precision needed for LEGEND-1000. The MOSFET changes its behavior permanently, which makes it almost impossible to model a clear response function. For the experiment itself, this means that every energy event features a different shape which makes it extremely hard to find a suitable and reliable analysis routine. Nevertheless, it should be mentioned that in principle, optimal filtering methods exist for this kind of waveform shape so that an appropriate shaper could extract information like energy and current in a precise way [108]. However, at higher rates and with pile-up events when a previous event is disturbing the waveform of the current event, the state of the circuit and the MOSFET can never be fully determined, which makes it even harder since one cannot rely on an assumable baseline state of the system from which the non-linear behavior starts in contrast to the timely separated input waveform send by a pulser.

4.2.5 Noise measurement results

To determine the electronic noise performance of the LBNL ASIC, a noise measurement campaign was performed in the vacuum and cold setup. Therefore, 10000 waveforms with a pulser input voltage of 1 V have been acquired. Instead of using a multi-channel analyzer (MCA), the electronic noise extraction was performed offline using two different methods. At first, the waveforms have been pole-zero corrected with the help of a simple exponential fit, and the method explained in the previous section by ignoring the unprecise result. After that, the waveforms have been shaped with a symmetrical trapezoidal filter with a fixed flat top time of 2 µs and varying filter rise times $0.5\,\mu s \leq rt \leq 7.5\,\mu s$ for all acquired waveforms. Following this, the baseline values at a fixed time point (ftp) have been extracted and plotted versus the corresponding filter rise time. The resulting distributions show a Gaussian shape from which the FWHM was extracted by fitting a Gaussian function to the data points. Finally, this FWHM is extracted and illustrated in Figure 4.20 versus the filter rise time in semi-log plot. The figure states a minimum baseline noise of 0.176 mV at a filter rise time of 3 µs .[2] As explained in Section 3.2, the noise curve features the series noise as a linear curve with a negative slope in the limit of infinite small filter rise times, the 1/f noise as a vertical shift independent of the rise time, and the parallel noise as a linear curve with a positive slope in the limit of infinite high filter rise times. As deduced in Section 3.1.1 by assuming a sufficiently high gain of the ASIC, it produces a output voltage V_O which is proportional to the signal charge Q_S and inverse proportional to the feedback

[2] It has to be mentioned that the applied shaping filter is far from optimal, and the unprecise pole-zero correction limits the hole method before shaping.

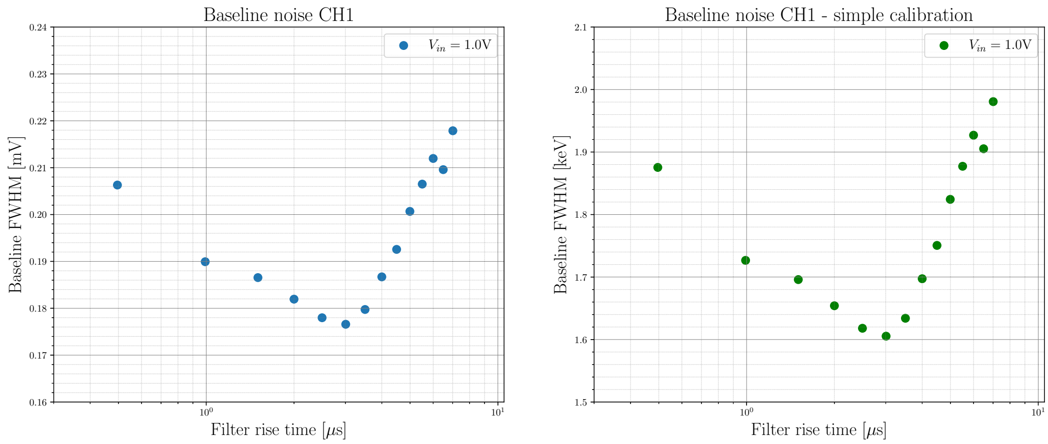

Figure 4.20: Preliminary noise performance of the LBNL ASIC in terms of baseline FWHM for 1 V input voltage at 45 ns pulser rising edge in the vacuum and cold setup. The right plot shows the baseline FWHM in keV for a simple energy calibration assuming a feedback capacity of $C_f = 400\,\text{fF}$.

capacity C_f in a sufficient approximation. Under the assumption of a feedback capacity of 500 fF, this can be used to get a simple energy calibration

$$V_O = \frac{Q_S}{C_f} = \frac{55\,\text{fC}\,\text{MeV}^{-1}}{500\,\text{fF}} = 110\,\frac{\text{mV}}{\text{MeV}} \tag{4.10}$$

with the value of Q_S being typical for germanium. The right plot in Figure 4.20 shows this calibration for the noise curve. Following this, an upper limit of 1.6 keV baseline FWHM is found at a filter rise time of 3 µs. As already mentioned, only an upper limit can be extracted because neither the shaping techniques nor the setup and measurement procedure is optimal. For a more realistic noise curve, the chip has to be connected to a HPGe detector to get calibration data together with a noise curve by using appropiate shaping filter. To better understand the noise performance of the ASIC and therefore also the setup, a power spectrum consisting of the power spectral density versus frequency plot has been generated. Herefore, the baseline of each waveform has been extracted in the length of 40 µs. After that, the power spectrum for each single waveform was generated with a periodogram using a Hann window and the individual power spectra are averaged to get the final power spectrum which is shown in Figure 4.21 [109]. As the figure illustrates, the baseline noise is dominated by high frequency noise > 10 MHz. The 1/f noise at lower frequencies is subdominant.

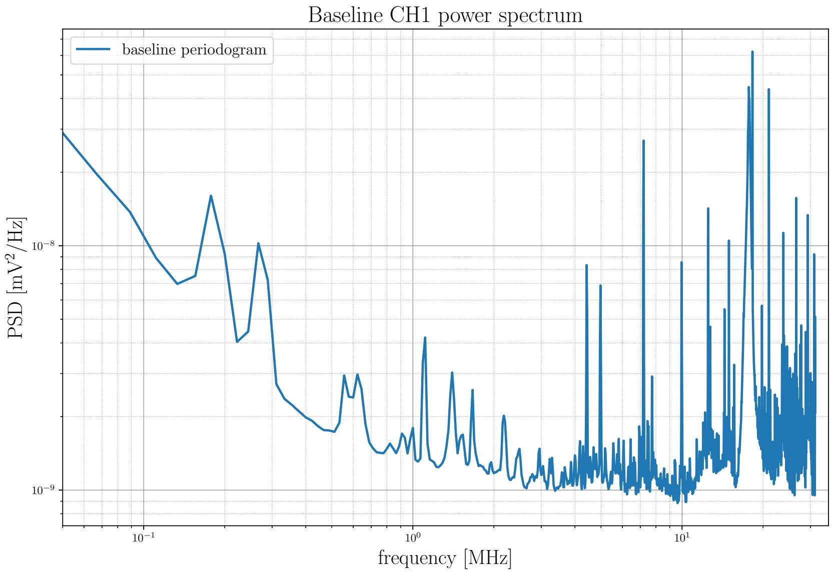

Figure 4.21: Power spectra of the baseline obtained from 10000 waveforms obtained with the LBNL ASIC at 1 V pulser input voltage with 45 ns rising edge in the vacuum and cold setup.

4.3 Second-stage circuit approach

As explained in detail in Section 4.2.4, the major problem of the LBNL ASIC is the decay tail which features non-linearities that are not suitable for a reliable analysis of the pulses. The unavailibility of large-value resistors in IC and therefore ASIC technology presents design problems so that the typical design layout of a CSA made from discrete components with resistive feedback loop $\mathcal{O}(1\,\mathrm{G}\Omega)$ cannot be applied. Therefore, a resistorless solution is needed. As seen for the LBNL ASIC, a first approach by using a nMOSFET feedback loop (c.f. Figure 4.14) features waveforms with the desired decay times, but has non-linearities that arise from the fact that a MOSFET is no linear device as a classical resistor. A new approach from [110] suggests the expansion of such a circuit with a so-called second stage to cancel out arising non-linearities of the MOSFET. The proposed circuit of such a layout is shown in Figure 4.22. The first stage features the typical non-linear behavior for MOSFET based feedback loops with a transfer function that can be calculated in small-signal approximation to [110]

$$V_O = -\frac{I_D}{C_F}\frac{\frac{2}{g_m}C_F}{1+sC_F\frac{2}{g_m}} \tag{4.11}$$

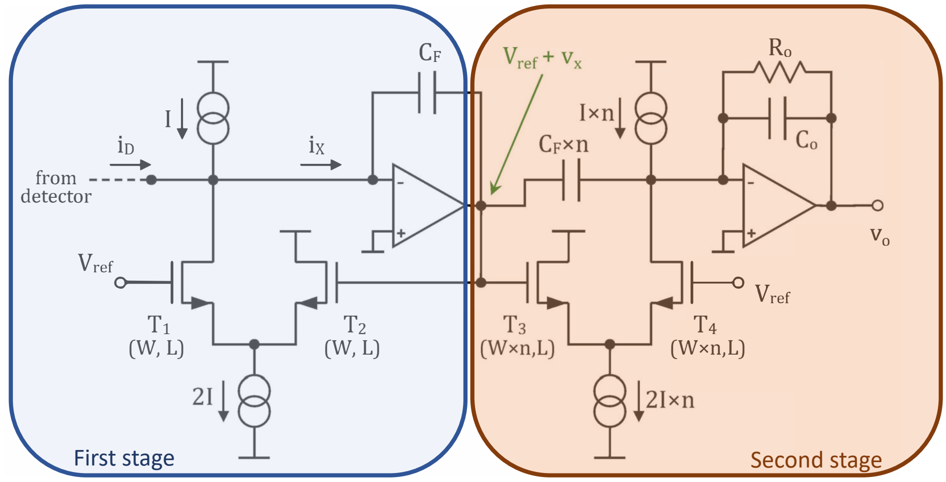

Figure 4.22: Circuit layout of the second-stage circuit approach from Pullia et. al. [110]. The non-linearities introduced from the differential pair T_1/T_2 in the first stage is cancelled out by a second stage employing a second differential pair T_3/T_4 working with the same gate source and drain voltages as the first pair. Figure from [110].

with C_F the feedback capacity, g_m the transconductance of the MOSFET, s the independent variable in the Laplace domain and I_D the Laplace counterpart of the current signal i_D coming from the detector .[3] This transfer function depends on the transconductance g_m, which can be seen as a "small signal" parameter since it can change in a huge amount over the full voltage swing of the CSA resulting in the non-linear behavior with input-dependent decay tail shapes. If now a second stage consisting of a second differential pair T_3/T_4 always working with the same gate, source, and drain voltages as the first pair and a feedback capacitor C_F both only scaled in size with a scale factor n is cascaded to the first stage, the two differential pairs cancel each other out, resulting in a single pole introduced by the C_0R_0 feedback loop resulting in a new transfer function which can be calculated to [110]

$$V_O = \underbrace{\frac{Q_S}{C_F}}_{\text{charge integration}} \underbrace{\left(n\frac{C_F}{C_0}\right)}_{\text{gain term}} \underbrace{\frac{C_0R_0}{1+sC_0R_0}}_{\text{single pole}} \tag{4.12}$$

with Q_S being the signal charge coming from the detector. Equation 4.12 shows that this new transfer function is now independently of the transconductance

[3]The Laplace domain can be understood as the equivalent to Fourier domain where the Laplace relates to discrete signals rather than continous functions.

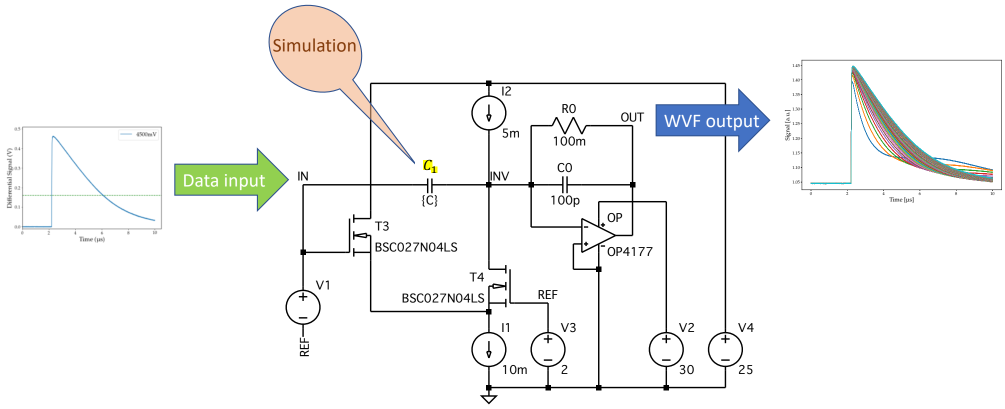

Figure 4.23: Simulation procedure for a proof-of-concept study of a second-stage circuit approach for the LBNL ASIC. Waveforms are acquired with the chip at room temperature for different input voltages. Following, the acquired data is feed into a LTSpice simulation which simulates several possible second stage circuits by varying over components like the feedback capacity C_F. Some components like the OpAmp and the MOSFETs have been preselected by a trial and error study to get appropiate waveforms out of the circuit. At the end, all simulated waveforms are stored on disk.

g_m and only contains linear devices. Furhtermore, it has a clean exponential decay over the full voltage swing as needed with a new decay constant $\tau = \frac{1}{C_0 R_0}$.[4] Because this new decay time constant is now independent of the feedback capacity which has to fulfill special criteria for the charge integration (c.f. Section 3.1.1), it can be adjusted by chosing C_0 without the need to have a high ohmic resistor R_0 to get to appropiate decay tails of $\tau \sim \mathcal{O}(100\,\mu\text{s})$. Furhtermore, the gain term introduced can further amplify the signal to counterbalance the choice of C_0.

To test the possible implementation of such a design into the LBNL ASIC, a proof-of-concept study was conducted in this thesis. Here, a LTSpice simulation was used to simulate a possible second stage circuit while using real waveform data acquired from the ASIC chip as input to the circuit. This procedure is illustrated in Figure 4.23. At first, waveform data was acquired for different input voltages at room temperature to avoid the need to simulate at cryogenic temperatures. Following, a simulation was set up by remodeling the second stage from Figure 4.22 in LTSpice and varying different circuit parameters like supply voltages

[4] A single pole in a transfer function in the Laplace domain as the one seen in Equation 4.12 translates into a exponential decay in the time domain with decay constant at the pole because the Laplace transform of $\frac{1}{s+\alpha}$ is $e^{-\alpha t} \cdot u(t)$ with $u(t)$ the unit step [111].

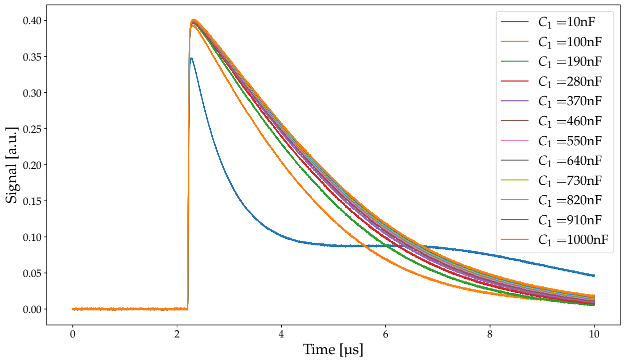

Figure 4.24: Example of the output of the LTSPICE simulation for the variation of the capacitance C_1. The input data to the simulated circuit was based on real ASIC with a pulser input voltage of 4 V. The circuit highly influences the shape of the decaying tail while leaving the leading edge and baseline unaffected.

and currents in the different sources. Finally, after setting all circuit parameters and component types to fixed values at which clean output waveforms could be detected, a optimization was performed based on only the capacitor C_1 as varied parameter. This approach was chosen because no concrete values for the MOSFET behavior in the ASIC can be extracted live, which would be needed to fulfill the coupling of the two differential pairs as explained above. Therefore, it was much easier to vary the capacitance instead of varying the types of the MOSFET or other components. An example of so extracted waveforms with the varied capacitor is shown in Figure 4.24. The variation of this single input parameter highly influences the shape of the decaying tail while leaving the leading edge and the baseline unaffected. In a final step, all resulting waveforms have been fitted with an exponential function, and an optimization algorithm extracted the minimum in terms of covariance of the fit. Figure 4.25 shows the resulting waveform after the optimization. The simulated circuit optimization was able to remove the non-linear behavior of the chip resulting in a clean exponential decay shape with a decay time in the range of typical decay times at room temperature.

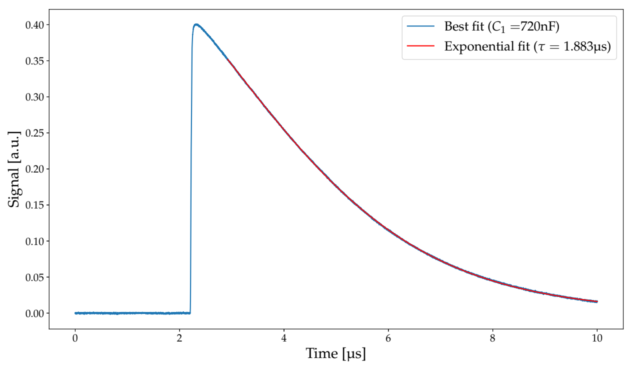

Figure 4.25: Resulting waveform of the proof-of-concept study. The circuit optimization could remove the non-linear behavior of the LBNL ASIC resulting in a clean exponential decay tail shape without concerning real electronic and physical design requirements of a real-world implementation.

Chapter 5
Conclusion and Outlook

The Large Enriched Germanium Experiment for $0\nu\beta\beta$ Decay (LEGEND) will search for $0\nu\beta\beta$ in the isotope ^{76}Ge with unprecedented sensitivity with a target half-life $T^{0\nu}_{1/2} > 10^{28}$ yr which would fully cover the inverted ordering of neutrinos. The observation of $0\nu\beta\beta$ decay would shed light on the nature of neutrinos, whether they are their own antiparticle or not. LEGEND consists of two stages namely LEGEND-200 and LEGEND-1000 where the first stage has already started commissioning in the Laboratori Nazionali del Gran Sasso (LNGS).
Regarding LEGEND-200, the thesis shows major contributions during the first phase of the integration and commissioning of signal readout electronics in the summer and autumn 2021. In a first measurement campaign, integration testing of signal readout electronics was performed during a research stay at LNGS of the author. The thesis presented an optimization for the signal transfer line which improved the rise time and signal integrity of the readout electronics. Furthermore, several component tests were presented which could show the functionality of the charge sensitive amplifier (CSA) in the final setup. In a second campaign, the thesis contributed to the commissioning of the first detectors in LEGEND-200. First, a detailed noise analysis of the readout chain with respect to the high voltage (HV) system was presented which resulted in the identification and reduction of noise sources in the setup. Following, the thesis showed the results of the 4 detector test for the first calibration run with four high-purity germanium (HPGe) detectors in LEGEND-200. The results exhibited the functionality of the signal readout electronics and presented the analysis of the data. Here, the energy resolution was determined as parameter of interest which showed a slightly worse performance because of electronic noise. Summarizing, the contributions of the thesis gave a detailed analysis of the current performance status of the signal readout electronics in LEGEND-200 which is an important milestone in the further success of the experiment. Future measurement campaigns can rely on the obtained results and further increase performance with respect to the current evaluation.
Regarding LEGEND-1000, the thesis presented the analysis and investigation of

a novel CSA based on application-specific integrated circuit (ASIC) technology developed by Lawrence Berkeley National Laboratory (LBNL). The chip integrates the two stages of the current LEGEND-200 CSA design targeting better noise performance. Three measurement campaigns with different setups were performed. The results showed that the chip could improve a number of open issues from previous ASIC based CSA implementations such as reduced number of supply lines, compatibility with higher detector capacitances and differential signal ouput with sufficient rise times. Furthermore, a detailed investigation of the feedback loop and the corresponding reset mechanism inside the chip demonstrated that the decay tail is not suitable for current analysis routines used in LEGEND. The metal–oxide–semiconductor field-effect transistor (MOSFET) used in the feedback loop introduced non-linearities that disturb signal integrity and reliability. To account for this problem, the thesis introduced a possible solution where the circuit is extended with a second-stage to cancel out the non-linearities resulting in output waveforms with clean exponential behavior at proper decay times $\mathcal{O}(100\,\mu\text{s})$. A proof-of-concept study showed that the working principle of such a second-stage circuit is applicable to the LBNL ASIC by simulating the second-stage obtaining clean waveform outputs.
In the future, a more detailed testing of the performance of the LBNL ASIC is needed which needs to connect the chip to a HPGe detector. This tests are planned in the new cryostat test stand at Technical University of Munich (TUM) to fully verify obtained noise results with a BEGe detector.
In addition, a new ASIC based CSA called TUM ASIC is currently under developement relying on the results obtained by this thesis. The main idea is to tackle two different approaches: on the one hand, a second-stage circuit approach as presented in this thesis is developed which would be the best possible solution since all advantages of having a full functioning CSA in one single chip would remain. On the other, a second approach tries to implement a ASIC based CSA with an external resistor consisting of amorphous germanium (aGe) such as the one in the low-mass front-end (LMFE) of LEGEND-200. A preliminary design layout can be found in Figure 5.1 where the chip is connected to the aGe resistor via two wire bonds. This approach would fulfill the radiopurity requirements while gaining the advantages of a ASIC based CSA close to the detector without challenging the difficulties of an internal feedback loop inside the chip.

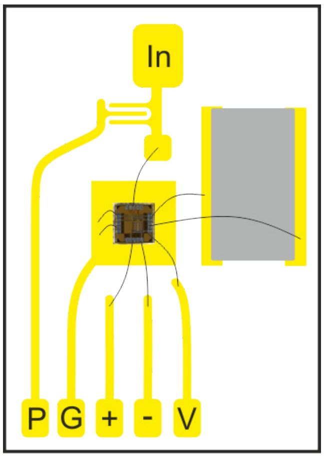

Figure 5.1: Alternative preliminary design layout of ASIC CSA for LEGEND-1000 with an external resistor made of amorphous germanium (aGe). The resistor is connected to the chip via two wire bonds. Figure courtesy to M. Willers.

Appendices

Appendix A

Bibliography

[1] F. Reines and C. L. Cowan, »Detection of the Free Neutrino«, in: *Physical Review* 92.3 (1953), pp. 830–831, DOI: 10.1103/physrev.92.830.

[2] C. L. Cowan et al., »Detection of the Free Neutrino: a Confirmation«, in: *Science* 124.3212 (1956), pp. 103–104, DOI: 10.1126/science.124.3212.103.

[3] F. Reines et al., »Detection of the Free Antineutrino«, in: *Physical Review* 117.1 (1960), pp. 159–173, DOI: 10.1103/physrev.117.159.

[4] Y. Fukuda et al., »Evidence for Oscillation of Atmospheric Neutrinos«, in: *Physical Review Letters* 81.8 (1998), pp. 1562–1567, DOI: 10.1103/physrevlett.81.1562.

[5] Q. R. Ahmad et al., »Direct Evidence for Neutrino Flavor Transformation from Neutral-Current Interactions in the Sudbury Neutrino Observatory«, in: *Physical Review Letters* 89.1 (2002), DOI: 10.1103/physrevlett.89.011301.

[6] M. Agostini et al., »Results on Neutrinoless Double-β Decay of ^{76}Ge from Phase I of the GERDA Experiment«, in: *Physical Review Letters* 111.12 (2013), DOI: 10.1103/physrevlett.111.122503.

[7] GERDA collaboration, »Background-free search for neutrinoless double-β decay of ^{76}Ge with GERDA«, in: *Nature* 544.7648 (2017), pp. 47–52, DOI: 10.1038/nature21717.

[8] K.-H. Ackermann et al., »The Gerda experiment for the search of $0\nu\beta\beta$ decay in ^{76}Ge«, in: *The European Physical Journal C* 73.3 (2013), DOI: 10.1140/epjc/s10052-013-2330-0.

[9] M. Agostini et al., »Upgrade for Phase II of the Gerda experiment«, in: *The European Physical Journal C* 78.5 (2018), DOI: 10.1140/epjc/s10052-018-5812-2.

[10] M. Agostini et al., »Final Results of GERDA on the Search for Neutrinoless Double- β Decay«, in: *Physical Review Letters* 125.25 (2020), DOI: `10.1103/physrevlett.125.252502`.

[11] S. I. Alvis et al., »Search for neutrinoless double- β decay in Ge76 with 26 kg yr of exposure from the Majorana Demonstrator«, in: *Physical Review C* 100.2 (2019), DOI: `10.1103/physrevc.100.025501`.

[12] P.A. Zyla et al., »Review of Particle Physics«, in: *PTEP* 2020.8 (2020), p. 083C01, DOI: `10.1093/ptep/ptaa104`.

[13] C. S. Wu et al., »Experimental Test of Parity Conservation in Beta Decay«, in: *Phys. Rev.* 105 (4 1957), pp. 1413–1415, DOI: `10.1103/PhysRev.105.1413`.

[14] U.F. Katz and Ch. Spiering, »High-energy neutrino astrophysics: Status and perspectives«, in: *Progress in Particle and Nuclear Physics* 67.3 (2012), pp. 651–704, ISSN: 0146-6410, DOI: `10.1016/j.ppnp.2011.12.001`.

[15] Raymond Davis, »A review of the homestake solar neutrino experiment«, in: *Progress in Particle and Nuclear Physics* 32 (1994), pp. 13–32, ISSN: 0146-6410, DOI: `https://doi.org/10.1016/0146-6410(94)90004-3`.

[16] Raymond Davis, »Solar Neutrinos. II. Experimental«, in: *Phys. Rev. Lett.* 12 (11 1964), pp. 303–305, DOI: `10.1103/PhysRevLett.12.303`.

[17] Raymond Davis, Don S. Harmer and Kenneth C. Hoffman, »Search for Neutrinos from the Sun«, in: *Phys. Rev. Lett.* 20 (21 1968), pp. 1205–1209, DOI: `10.1103/PhysRevLett.20.1205`.

[18] Bruce T. Cleveland et al., »Measurement of the Solar Electron Neutrino Flux with the Homestake Chlorine Detector«, in: 496.1 (1998), pp. 505–526, DOI: `10.1086/305343`.

[19] P. Anselmann et al., »GALLEX solar neutrino observations: complete results for GALLEX II«, in: *Physics Letters B* 357.1 (1995), pp. 237–247, ISSN: 0370-2693, DOI: `https://doi.org/10.1016/0370-2693(95)00897-T`.

[20] M. Altmann et al., »Complete results for five years of GNO solar neutrino observations«, in: *Physics Letters B* 616.3 (2005), pp. 174–190, ISSN: 0370-2693, DOI: `https://doi.org/10.1016/j.physletb.2005.04.068`.

[21] A. I. Abazov et al., »Search for neutrinos from the Sun using the reaction $^{71}\mathrm{Ga}(\nu_e,e^-)^{71}\mathrm{Ge}$«, in: *Phys. Rev. Lett.* 67 (24 1991), pp. 3332–3335, DOI: `10.1103/PhysRevLett.67.3332`.

[22] J. N. Abdurashitov et al., »Solar neutrino flux measurements by the Soviet-American gallium experiment (SAGE) for half the 22-year solar cycle«, in: 95.2 (2002), pp. 181–193, DOI: 10.1134/1.1506424.

[23] C. Arpesella et al., »First real time detection of 7Be solar neutrinos by Borexino«, in: *Physics Letters B* 658.4 (2008), pp. 101–108, ISSN: 0370-2693, DOI: https://doi.org/10.1016/j.physletb.2007.09.054.

[24] G. Alimonti et al., »The Borexino detector at the Laboratori Nazionali del Gran Sasso«, in: *Nuclear Instruments and Methods in Physics Research Section A: Accelerators, Spectrometers, Detectors and Associated Equipment* 600.3 (2009), pp. 568–593, ISSN: 0168-9002, DOI: https://doi.org/10.1016/j.nima.2008.11.076.

[25] G. Bellini et al., »Precision Measurement of the ^{7}Be Solar Neutrino Interaction Rate in Borexino«, in: *Phys. Rev. Lett.* 107 (14 2011), p. 141302, DOI: 10.1103/PhysRevLett.107.141302.

[26] S. M. Bilenky, »Bruno Pontecorvo and the neutrino«, in: *Phys. Usp.* 57.5 (2014), pp. 489–496, DOI: 10.3367/UFNe.0184.201405g.0531.

[27] Y. Fukuda et al., »Evidence for Oscillation of Atmospheric Neutrinos«, in: *Phys. Rev. Lett.* 81 (8 1998), pp. 1562–1567, DOI: 10.1103/PhysRevLett.81.1562.

[28] K.A. Olive, »Review of Particle Physics«, in: 40.10 (2016), p. 100001, DOI: 10.1088/1674-1137/40/10/100001.

[29] G. Bellini et al., »Neutrino Oscillations«, in: *Advances in High Energy Physics* 2014 (2014), pp. 1–28, ISSN: 1687-7365, DOI: 10.1155/2014/191960.

[30] Ivan Esteban et al., »The fate of hints: updated global analysis of three-flavor neutrino oscillations«, in: 2020.9 (2020), DOI: 10.1007/jhep09(2020)178.

[31] Kevin J. Kelly et al., »Neutrino mass ordering in light of recent data«, in: *Physical Review D* 103.1 (2021), ISSN: 2470-0029, DOI: 10.1103/physrevd.103.013004.

[32] Frank Arne Edzards, »Characterization of point contact Germanium detectors and development of signal readout electronics for LEGEND«, Dissertation, Munich: Technical University of Munich, 2021.

[33] S. M. Bilenky and C. Giunti, »Neutrinoless double-beta decay: A probe of physics beyond the Standard Model«, in: 30.04n05 (2015), p. 1530001, DOI: 10.1142/s0217751x1530001x.

[34] R N Mohapatra et al., »Theory of neutrinos: a white paper«, in: 70.11 (2007), pp. 1757–1867, DOI: `10.1088/0034-4885/70/11/r02`.

[35] Peter Minkowski, »$\mu \to e\gamma$ at a rate of one out of 109 muon decays?«, in: *Physics Letters B* 67.4 (1977), pp. 421–428, ISSN: 0370-2693, DOI: `https://doi.org/10.1016/0370-2693(77)90435-X`.

[36] Murray Gell-Mann, Pierre Ramond and Richard Slansky, *Complex Spinors and Unified Theories*, 2013, arXiv: `1306.4669 [hep-th]`.

[37] Rabindra N. Mohapatra and Goran Senjanovi ć, »Neutrino Mass and Spontaneous Parity Nonconservation«, in: *Phys. Rev. Lett.* 44 (14 1980), pp. 912–915, DOI: `10.1103/PhysRevLett.44.912`.

[38] Tsutomu Yanagida, »Horizontal Symmetry and Masses of Neutrinos«, in: *Progress of Theoretical Physics* 64.3 (1980), pp. 1103–1105, ISSN: 0033-068X, eprint: `https://academic.oup.com/ptp/article-pdf/64/3/1103/5394376/64-3-1103.pdf`, DOI: `10.1143/PTP.64.1103`.

[39] C. F. v. Weizsäcker, »Zur Theorie der Kernmassen«, in: 96.7-8 (1935), pp. 431–458, DOI: `10.1007/bf01337700`.

[40] M. Goeppert-Mayer, »Double Beta-Disintegration«, in: *Physical Review* 48.6 (1935), pp. 512–516, DOI: `10.1103/physrev.48.512`.

[41] Vladimir I Tretyak and Yuri G Zdesenko, »TABLES OF DOUBLE BETA DECAY DATA—AN UPDATE«, in: *Atomic Data and Nuclear Data Tables* 80.1 (2002), pp. 83–116, DOI: `10.1006/adnd.2001.0873`.

[42] J. Kotila and F. Iachello, »Phase-space factors for double-βdecay«, in: *Physical Review C* 85.3 (2012), DOI: `10.1103/physrevc.85.034316`.

[43] J. Barea, J. Kotila and F. Iachello, »Nuclear matrix elements for double-βdecay«, in: *Physical Review C* 87.1 (2013), DOI: `10.1103/physrevc.87.014315`.

[44] P. Gysbers et al., »Discrepancy between experimental and theoretical β-decay rates resolved from first principles«, in: *Nature Physics* 15.5 (2019), pp. 428–431, DOI: `10.1038/s41567-019-0450-7`.

[45] H Primakoff and S P Rosen, »A Corrigendum to the Article 'Double Beta Decay' by H. Primakoff and S. P. Rosen inReports on Progress in Physics«, in: *Proceedings of the Physical Society* 78.3 (1961), pp. 464–465, DOI: `10.1088/0370-1328/78/3/116`.

[46] Felix Boehm and Petr Vogel, *Physics of Massive Neutrinos*, 2nd ed., Cambridge University Press, 1992, DOI: `10.1017/CBO9780511622571`.

[47] W. H. Furry, »On Transition Probabilities in Double Beta-Disintegration«, in: *Physical Review* 56.12 (1939), pp. 1184–1193, DOI: 10.1103/physrev.56.1184.

[48] M. Fukugita and T. Yanagida, »Barygenesis without grand unification«, in: *Physics Letters B* 174.1 (1986), pp. 45–47, DOI: 10.1016/0370-2693(86)91126-3.

[49] Andrei D Sakharov, »Violation ofCPin variance,Casymmetry, and baryon asymmetry of the universe«, in: *Soviet Physics Uspekhi* 34.5 (1991), pp. 392–393, DOI: 10.1070/pu1991v034n05abeh002497.

[50] WERNER RODEJOHANN, »NEUTRINO-LESS DOUBLE BETA DECAY AND PARTICLE PHYSICS«, in: *International Journal of Modern Physics E* 20.09 (2011), pp. 1833–1930, DOI: 10.1142/s0218301311020186.

[51] Stefano Dell'Oro et al., »Neutrinoless Double Beta Decay: 2015 Review«, in: *Advances in High Energy Physics* 2016 (2016), pp. 1–37, DOI: 10.1155/2016/2162659.

[52] J. Schechter and J. W. F. Valle, »Neutrinoless double-βdecay in SU(2)×U(1) theories«, in: *Physical Review D* 25.11 (1982), pp. 2951–2954, DOI: 10.1103/physrevd.25.2951.

[53] Michael Duerr, Manfred Lindner and Alexander Merle, »On the quantitative impact of the Schechter-Valle theorem«, in: *Journal of High Energy Physics* 2011.6 (2011), DOI: 10.1007/jhep06(2011)091.

[54] V. Cirigliano et al., »A neutrinoless double beta decay master formula from effective field theory«, in: *Journal of High Energy Physics* 2018.12 (2018), DOI: 10.1007/jhep12(2018)097.

[55] Michelle J. Dolinski, Alan W.P. Poon and Werner Rodejohann, »Neutrinoless Double-Beta Decay: Status and Prospects«, in: *Annual Review of Nuclear and Particle Science* 69.1 (2019), pp. 219–251, DOI: 10.1146/annurev-nucl-101918-023407.

[56] Jonathan Engel and Javier Menéndez, »Status and future of nuclear matrix elements for neutrinoless double-beta decay: a review«, in: *Reports on Progress in Physics* 80.4 (2017), p. 046301, DOI: 10.1088/1361-6633/aa5bc5.

[57] L. S. Song et al., »Nuclear matrix element of neutrinoless double-βdecay: Relativity and short-range correlations«, in: *Physical Review C* 95.2 (2017), DOI: 10.1103/physrevc.95.024305.

[58] L. Coraggio et al., »Calculation of the neutrinoless double- β decay matrix element within the realistic shell model«, in: *Physical Review C* 101.4 (2020), DOI: 10.1103/physrevc.101.044315.

[59] Vincenzo Cirigliano et al., »New Leading Contribution to Neutrinoless Double- β Decay«, in: *Physical Review Letters* 120.20 (2018), DOI: 10.1103/physrevlett.120.202001.

[60] K.A. Olive, »Review of Particle Physics«, in: *Chinese Physics C* 40.10 (2016), p. 100001, DOI: 10.1088/1674-1137/40/10/100001.

[61] Oliviero Cremonesi and Maura Pavan, »Challenges in Double Beta Decay«, in: *Advances in High Energy Physics* 2014 (2014), pp. 1–40, DOI: 10.1155/2014/951432.

[62] Matteo Agostini, Giovanni Benato and Jason A. Detwiler, »Discovery probability of next-generation neutrinoless double- β decay experiments«, in: *Physical Review D* 96.5 (2017), DOI: 10.1103/physrevd.96.053001.

[63] LEGEND Collaboration et al., *LEGEND-1000 Preconceptual Design Report*, 2021, arXiv: 2107.11462 [physics.ins-det].

[64] F. E. Emery and T. A. Rabson, »Average Energy Expended Per Ionized Electron-Hole Pair in Silicon and Germanium as a Function of Temperature«, in: *Physical Review* 140.6A (1965), A2089–A2093, DOI: 10.1103/physrev.140.a2089.

[65] Y.P. Varshni, »Temperature dependence of the energy gap in semiconductors«, in: *Physica* 34.1 (1967), pp. 149–154, DOI: 10.1016/0031-8914(67)90062-6.

[66] R. K. Schaevitz et al., »Indirect absorption in germanium quantum wells«, in: *AIP Advances* 1.3 (2011), p. 032164, DOI: 10.1063/1.3646149.

[67] G.F. Knoll, *Radiation Detection and Measurement*, Wiley, 2010, ISBN: 9780470131480, URL: https://www.wiley.com/en-us/Radiation+Detection+and+Measurement%2C+4th+Edition-p-9780470131480.

[68] W. Shockley, »Currents to Conductors Induced by a Moving Point Charge«, in: *Journal of Applied Physics* 9.10 (1938), pp. 635–636, DOI: 10.1063/1.1710367.

[69] S. Ramo, »Currents Induced by Electron Motion«, in: *Proceedings of the IRE* 27.9 (1939), pp. 584–585, DOI: 10.1109/jrproc.1939.228757.

[70] M Agostini et al., »Signal modeling of high-purity Ge detectors with a small read-out electrode and application to neutrinoless double beta decay search in Ge-76«, in: *Journal of Instrumentation* 6.03 (2011), P03005–P03005, DOI: 10.1088/1748-0221/6/03/p03005.

[71] M. Agostini et al., »Characterization of 30 ^{7}6Ge enriched Broad Energy Ge detectors for GERDA Phase II«, in: *The European Physical Journal C* 79.11 (2019), DOI: 10.1140/epjc/s10052-019-7353-8.

[72] C. E. Aalseth et al., »CoGeNT: A search for low-mass dark matter usingp-type point contact germanium detectors«, in: *Physical Review D* 88.1 (2013), DOI: 10.1103/physrevd.88.012002.

[73] G.K. Giovanetti et al., »A Dark Matter Search with MALBEK«, in: *Physics Procedia* 61 (2015), pp. 77–84, DOI: 10.1016/j.phpro.2014.12.014.

[74] D. Akimov et al., »Observation of coherent elastic neutrino-nucleus scattering«, in: *Science* 357.6356 (2017), pp. 1123–1126, DOI: 10.1126/science.aao0990.

[75] H. Bonet et al., »Constraints on Elastic Neutrino Nucleus Scattering in the Fully Coherent Regime from the CONUS Experiment«, in: *Physical Review Letters* 126.4 (2021), DOI: 10.1103/physrevlett.126.041804.

[76] R.J. Cooper et al., »A novel HPGe detector for gamma-ray tracking and imaging«, in: *Nuclear Instruments and Methods in Physics Research Section A: Accelerators, Spectrometers, Detectors and Associated Equipment* 665 (2011), pp. 25–32, DOI: 10.1016/j.nima.2011.10.008.

[77] Tommaso Comellato, Matteo Agostini and Stefan Schönert, »Charge-carrier collective motion in germanium detectors for $\beta\beta$-decay searches«, in: *The European Physical Journal C* 81.1 (2021), DOI: 10.1140/epjc/s10052-021-08889-0.

[78] Mark Thomson, *Modern Particle Physics*, Cambridge University Press, 2013, DOI: 10.1017/cbo9781139525367.

[79] Y. Efremenko et al., »Use of poly(ethylene naphthalate) as a self-vetoing structural material«, in: *Journal of Instrumentation* 14.07 (2019), P07006–P07006, DOI: 10.1088/1748-0221/14/07/p07006.

[80] Christoph Wiesinger, Luciano Pandola and Stefan Schönert, »Virtual depth by active background suppression: revisiting the cosmic muon induced background of Gerda Phase II«, in: *The European Physical Journal C* 78.7 (2018), DOI: 10.1140/epjc/s10052-018-6079-3.

[81] F. Edzards et al., »Investigation of ASIC-based signal readout electronics for LEGEND-1000«, in: *Journal of Instrumentation* 15.09 (2020), P09022–P09022, DOI: `10.1088/1748-0221/15/09/p09022`.

[82] F Edzards, »The Future of Neutrinoless Double Beta Decay Searches with Germanium Detectors«, in: *Journal of Physics: Conference Series* 1690.1 (2020), p. 012180, DOI: `10.1088/1742-6596/1690/1/012180`.

[83] Helmuth Spieler, »Front-End Electronics and Signal Processing«, in: *AIP Conference Proceedings*, AIP, 2003, DOI: `10.1063/1.1604074`.

[84] Helmuth Spieler, *Radiation Detectors and Signal Processing*, `https://www-physics.lbl.gov/~spieler/Heidelberg_Notes/`, (Accessed on 01/10/2022), 2001.

[85] J. Carr and J.J. Carr, *Practical Antenna Handbook*, PRACTICAL ANTENNA HANDBOOK, McGraw-Hill Companies,Incorporated, 2001, ISBN: 9780071374354, URL: `https://books.google.de/books?id=f3asJreno0YC`.

[86] E. Gatti and P. F. Manfredi, »Processing the signals from solid-state detectors in elementary-particle physics«, in: *La Rivista del Nuovo Cimento* 9.1 (1986), pp. 1–146, DOI: `10.1007/bf02822156`.

[87] Valerio D'Andrea, »Improvement of Performances and Background Studies in GERDA Phase II«, Dissertation, L'Aquila: Gran Sasso Science Institute, 2017.

[88] V Radeka, »Low-Noise Techniques in Detectors«, in: *Annual Review of Nuclear and Particle Science* 38.1 (1988), pp. 217–277, DOI: `10.1146/annurev.ns.38.120188.001245`.

[89] P. Barton et al., »Ultra-low noise mechanically cooled germanium detector«, in: *Nuclear Instruments and Methods in Physics Research Section A: Accelerators, Spectrometers, Detectors and Associated Equipment* 812 (2016), pp. 17–23, DOI: `10.1016/j.nima.2015.12.031`.

[90] Giovanni Benato, »Data Reconstruction and Analysis for the GERDA Experiment«, Dissertation, Zurich: University of Zurich, 2015.

[91] U. Fano, »Ionization Yield of Radiations. II. The Fluctuations of the Number of Ions«, in: *Physical Review* 72.1 (1947), pp. 26–29, DOI: `10.1103/physrev.72.26`.

[92] S. Croft and D.S. Bond, »A determination of the Fano factor for germanium at 77.4 K from measurements of the energy resolution of a 113 cm3 HPGe gamma-ray spectrometer taken over the energy range from 14 to 6129 keV«, in: *International Journal of Radiation Applications and Instrumentation. Part A. Applied Radiation and Isotopes* 42.11 (Jan. 1991), pp. 1009–1014, DOI: 10.1016/0883-2889(91)90002-i.

[93] B.G. Lowe, »Measurements of Fano factors in silicon and germanium in the low-energy X-ray region«, in: *Nuclear Instruments and Methods in Physics Research Section A: Accelerators, Spectrometers, Detectors and Associated Equipment* 399.2-3 (1997), pp. 354–364, DOI: 10.1016/s0168-9002(97)00965-0.

[94] M.C. Lépy et al., »Experimental study of the response of semiconductor detectors to low-energy photons«, in: *Nuclear Instruments and Methods in Physics Research Section A: Accelerators, Spectrometers, Detectors and Associated Equipment* 439.2-3 (2000), pp. 239–246, DOI: 10.1016/s0168-9002(99)00932-8.

[95] T. Papp et al., »A new approach to the determination of the Fano factor for semiconductor detectors«, in: *X-Ray Spectrometry* 34.2 (2004), pp. 106–111, DOI: 10.1002/xrs.754.

[96] Mark W Lund et al., »Low noise JFETs for room temperature x-ray detectors«, in: *Nuclear Instruments and Methods in Physics Research Section A: Accelerators, Spectrometers, Detectors and Associated Equipment* 380.1-2 (1996), pp. 318–322, DOI: 10.1016/s0168-9002(96)00473-1.

[97] Antonio LUcchini, »CGERMANIUM DETECTOR READOUT ELECTRONICS FOR LEGEND-200 Germanium Detector Readout Electronics for LEGEND-200«, Master thesis, Milan: University degli Studi di Milano, 2018.

[98] F. Werner et al., »Performance verification of the FlashCam prototype camera for the Cherenkov Telescope Array«, in: *Nuclear Instruments and Methods in Physics Research Section A: Accelerators, Spectrometers, Detectors and Associated Equipment* 876 (2017), pp. 31–34, DOI: 10.1016/j.nima.2016.12.056.

[99] Brookhaven National Laboratory National Nuclear Data Center, *Nudat 2.8*, https://www.nndc.bnl.gov/nudat3/chartNuc.jsp, (Accessed on 01/24/2022), 2022.

[100] M Agostini et al., »GELATIO: a general framework for modular digital analysis of high-purity Ge detector signals«, in: *Journal of Instrumentation* 6.08 (2011), P08013–P08013, DOI: 10.1088/1748-0221/6/08/p08013.

[101] P. Födisch et al., »Digital high-pass filter deconvolution by means of an infinite impulse response filter«, in: *Nuclear Instruments and Methods in Physics Research Section A: Accelerators, Spectrometers, Detectors and Associated Equipment* 830 (2016), pp. 484–496, DOI: 10.1016/j.nima.2016.06.019.

[102] Marius Grundmann, *The Physics of Semiconductors*, Springer International Publishing, 2016, DOI: 10.1007/978-3-319-23880-7.

[103] N. Smale et al., »Development and test results of a readout chip for the GERDA experiment«, in: *12th Workshop on Electronics for LHC and Future Experiments (LECC 2006)*, 2006, pp. 515–519.

[104] David C. Radford, *Drift-Time Correction for A/E*, LEGEND Collaboration Meeting Seatlle, 2019.

[105] S.M. Sze and Kwok K. Ng, *Physics of Semiconductor Devices*, John Wiley & Sons, Inc., 2006, DOI: 10.1002/0470068329.

[106] M.M. Quintas, J.J.G. Dominguez and S.E.P. Cagigas, *Dispositivos electronicos II*, Textos universitarios, SERVICIO DE PUBLICACIONES UNIVERSIDAD DE ALCALA, 2005, ISBN: 9788481386301, URL: https://books.google.de/books?id=3CujPAAACAAJ.

[107] B. Moon et al., »Analytical model for p-channel MOSFETs«, in: *IEEE Transactions on Electron Devices* 38.12 (1991), pp. 2632–2646, DOI: 10.1109/16.158685.

[108] E. Gatti et al., »Digital Penalized LMS method for filter synthesis with arbitrary constraints and noise«, in: *Nuclear Instruments and Methods in Physics Research Section A: Accelerators, Spectrometers, Detectors and Associated Equipment* 523.1-2 (2004), pp. 167–185, DOI: 10.1016/j.nima.2003.12.032.

[109] R. B. Blackman and J. W. Tukey, »The measurement of power spectra from the point of view of communications engineering - Part I«, in: *The Bell System Technical Journal* 37.1 (1958), pp. 185–282, DOI: 10.1002/j.1538-7305.1958.tb03874.x.

[110] A. Pullia and S. Capra, »Design of a resistorless ASIC preamplifier for HPGe detectors with non-linear pole/zero cancellation and controlled fast-reset feature«, in: *2012 IEEE Nuclear Science Symposium and Medical Imaging Conference Record (NSS/MIC)*, IEEE, 2012, DOI: 10.1109/nssmic.2012.6551066.

[111] J.G. Proakis and D.G. Manolakis, *Digital Signal Processing*, Prentice Hall international editions, Pearson Prentice Hall, 2007, ISBN: 9780131873742, URL: https://books.google.at/books?id=H%5C_5SAAAAMAAJ.

Appendix B

Additional figures

B.1 Integration tests

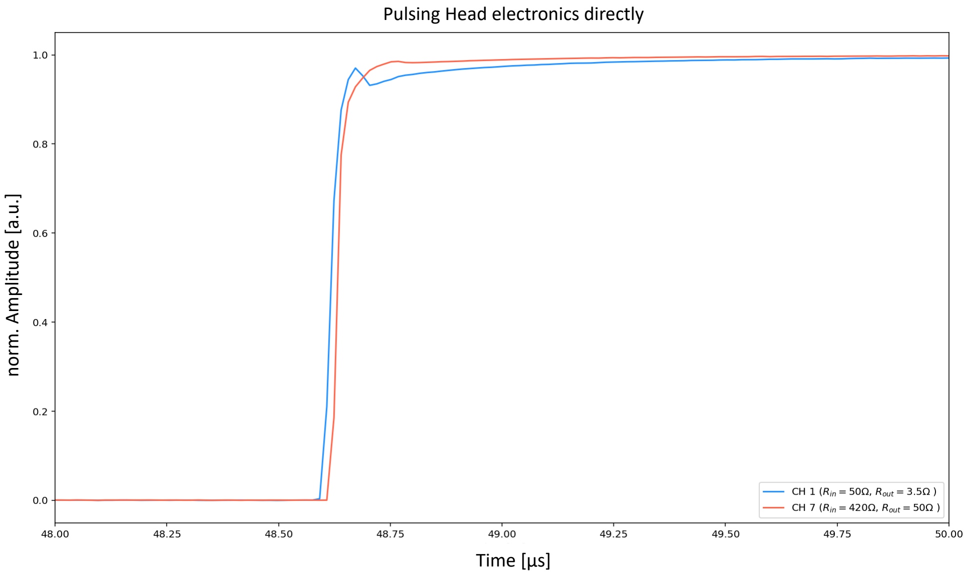

a) Effect of the buffer board configurations

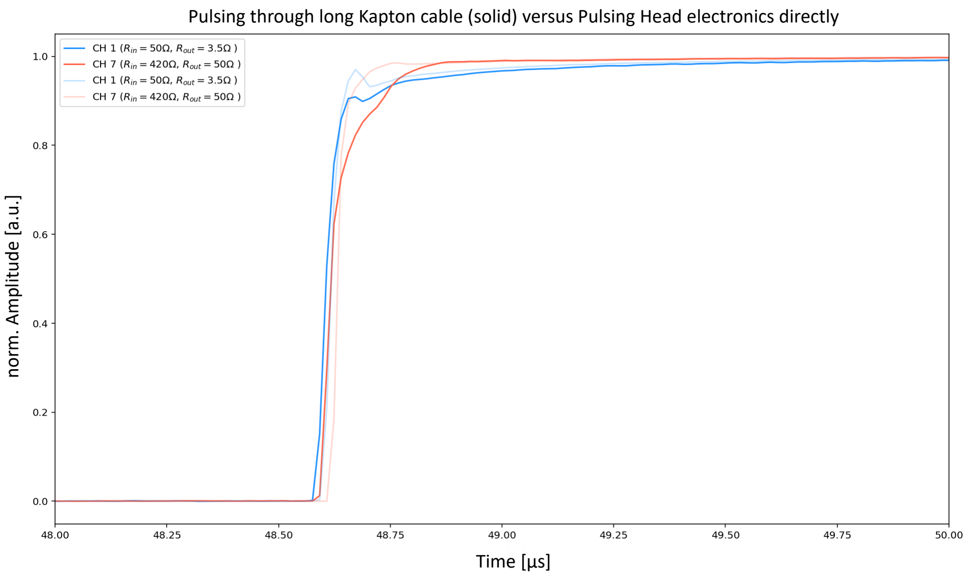

b) Effect of the long Kapton cable (solid)

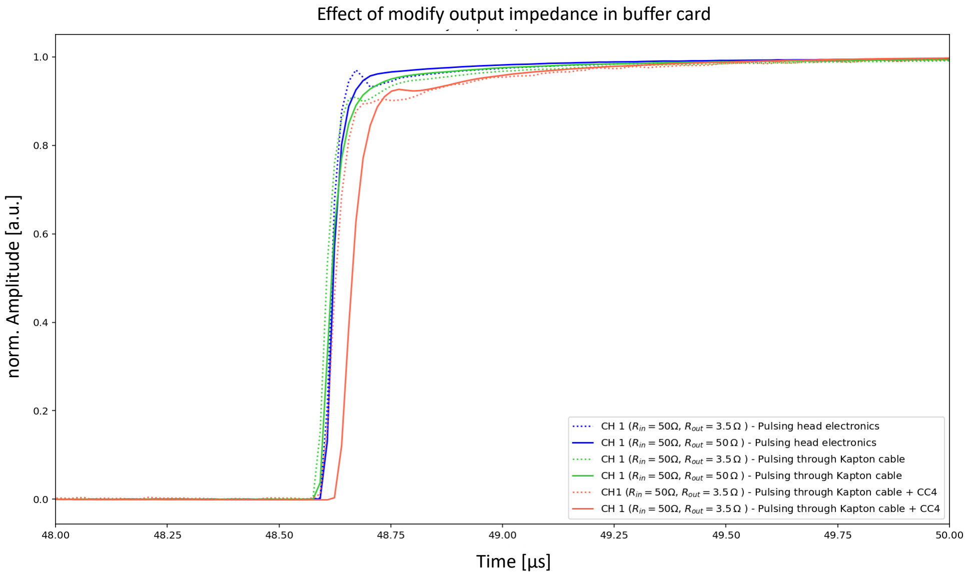

c) Effect of modifying the output impedance in buffer card

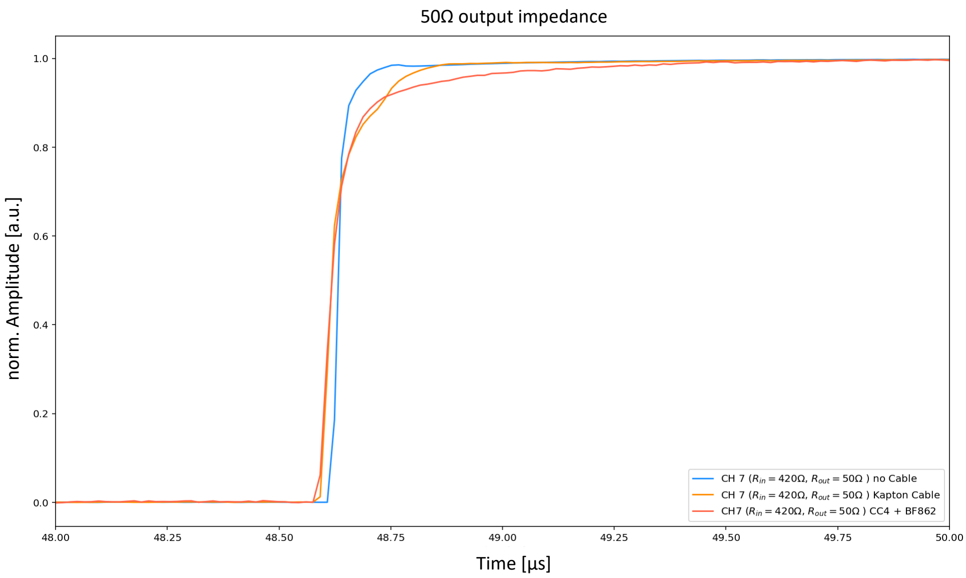

d) Effect of Kapton cable and CC4 with DFE feedback for the 50 Ω output impedance configuration

Figure B.1: Several buffer card tests performed with different configurations where 1000 waveforms were acquired and averaged as well as normalized before plotting: Figure B.1a shows the output pulses of the two buffer card configurations where Figure B.1b compares these with the measurements performed through the long Kapton cable. Figure B.1c shows the effect of modifying the output impedance to 50 Ω for the measurements directly with the head electronics, through the long Kapton cable and trough the Kapton using the pulser input of the head electronics itself injecting pulses to a CC4 and a dummy front-end.

B.2 Commissioning tests

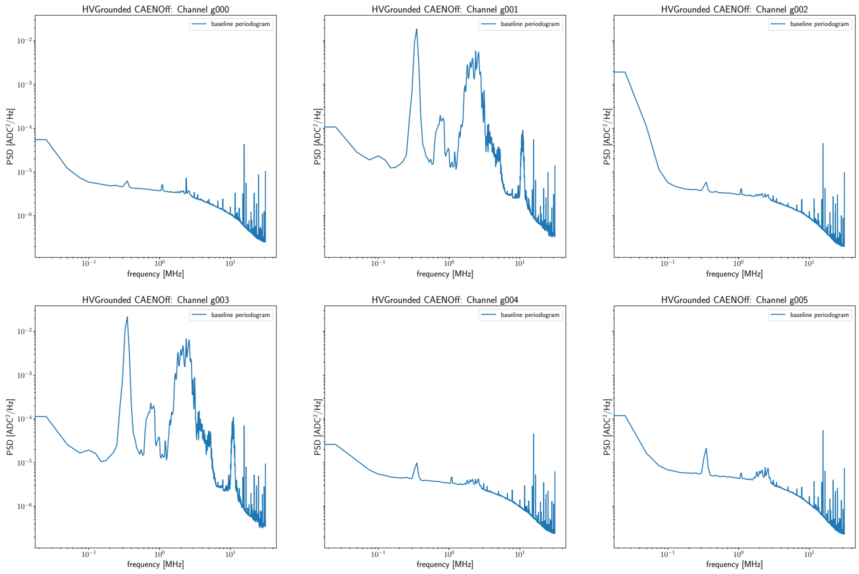

a) HVGrounded_CAENOff

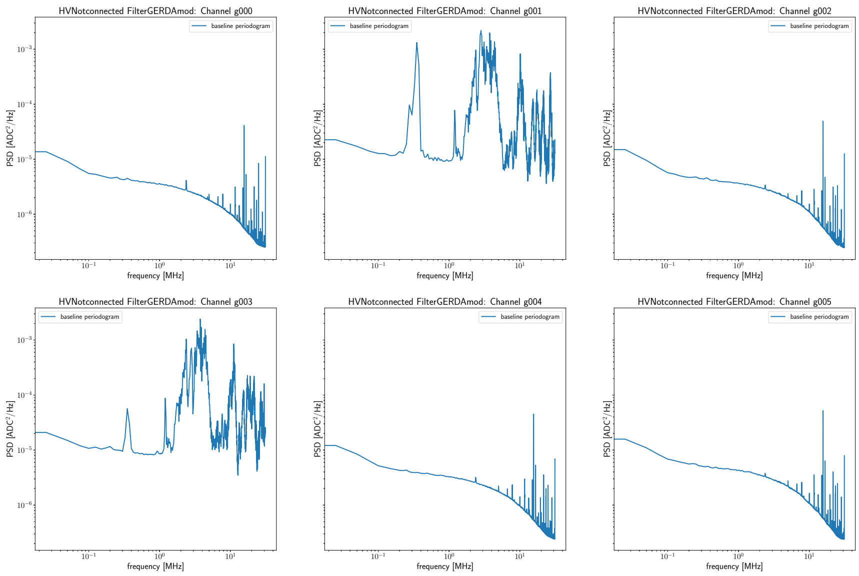

b) HVNotconnected_FilterGERDAmod

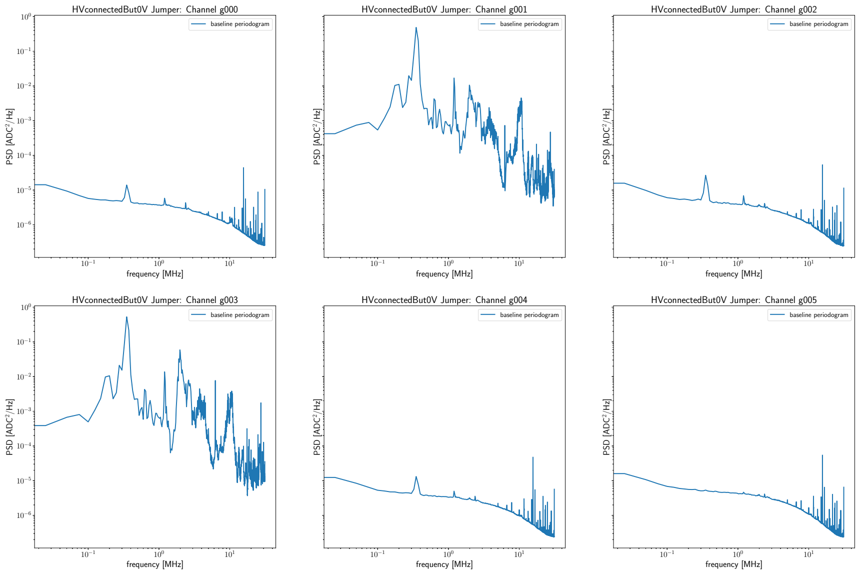

c) HVconnectedBut0V_Jumper

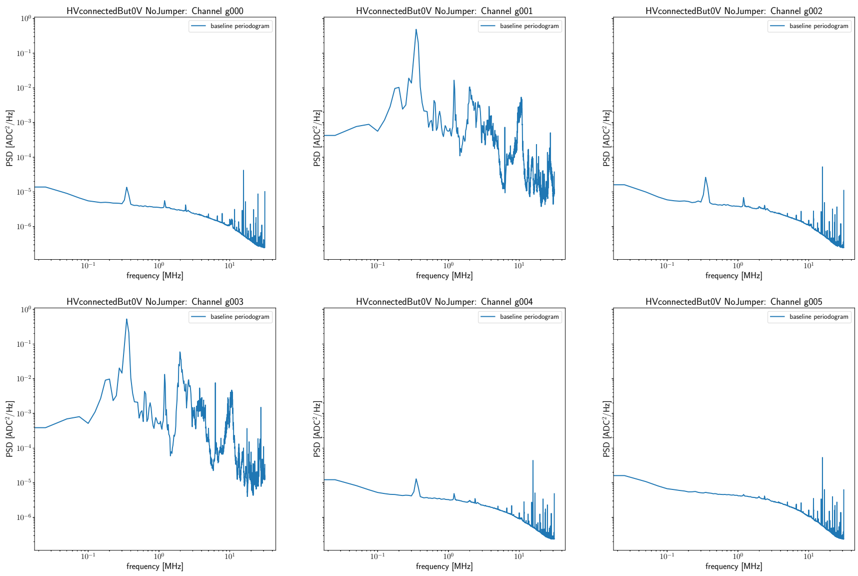

d) HVconnectedBut0V_NoJumper

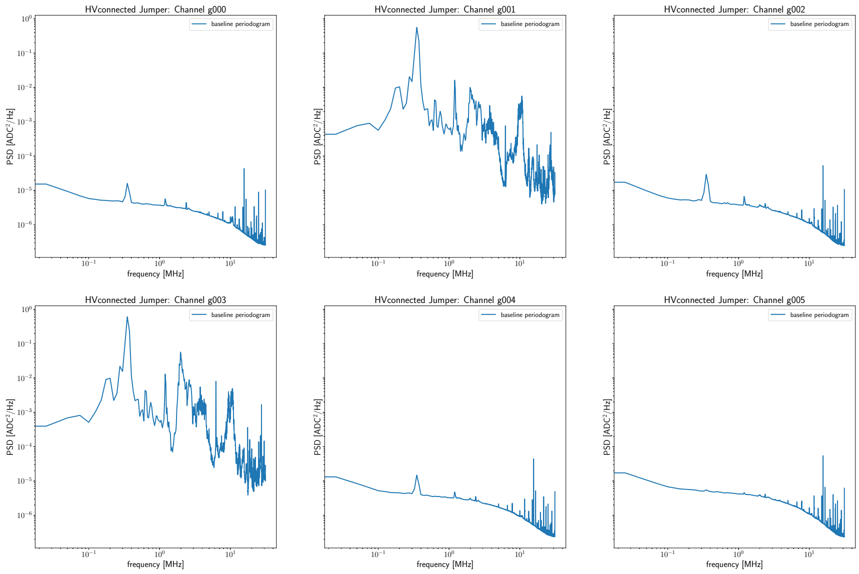

e) HVconnected_Jumper

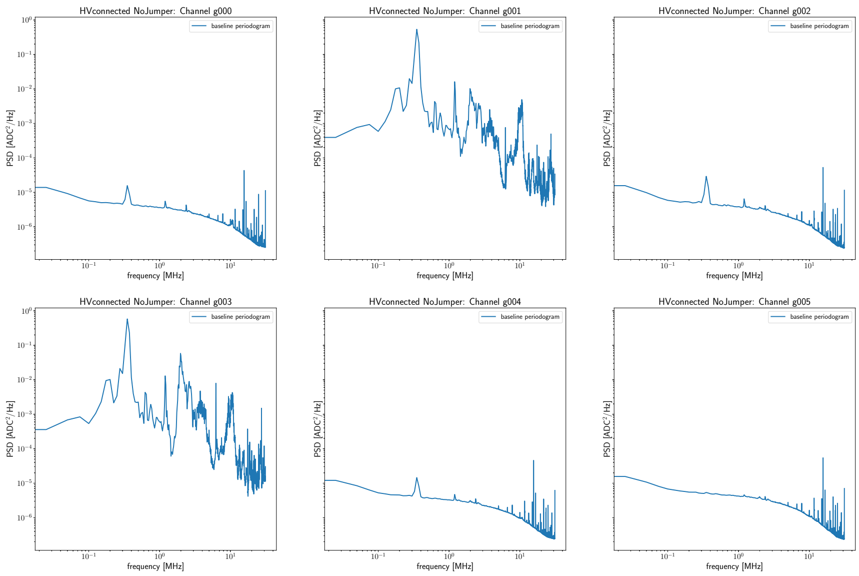

f) HVconnected_NoJumper

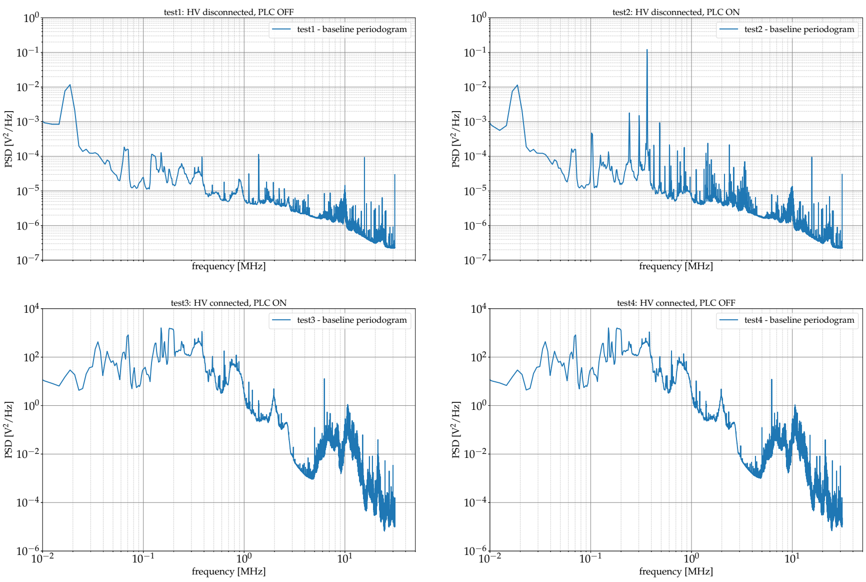

g) PLC tests 1, 2, 3 and 4

Figure B.2: Raw power spectrum density (PoSD) of all HV tests during commissioning tests of LEGEND-200. THe PoSD are generated by a periodogram with Hann window for each waveform and averaged. For the PLC tests in Figure B.2g, only one channel was obtained per measurement compared to all seven channel in the other tests.

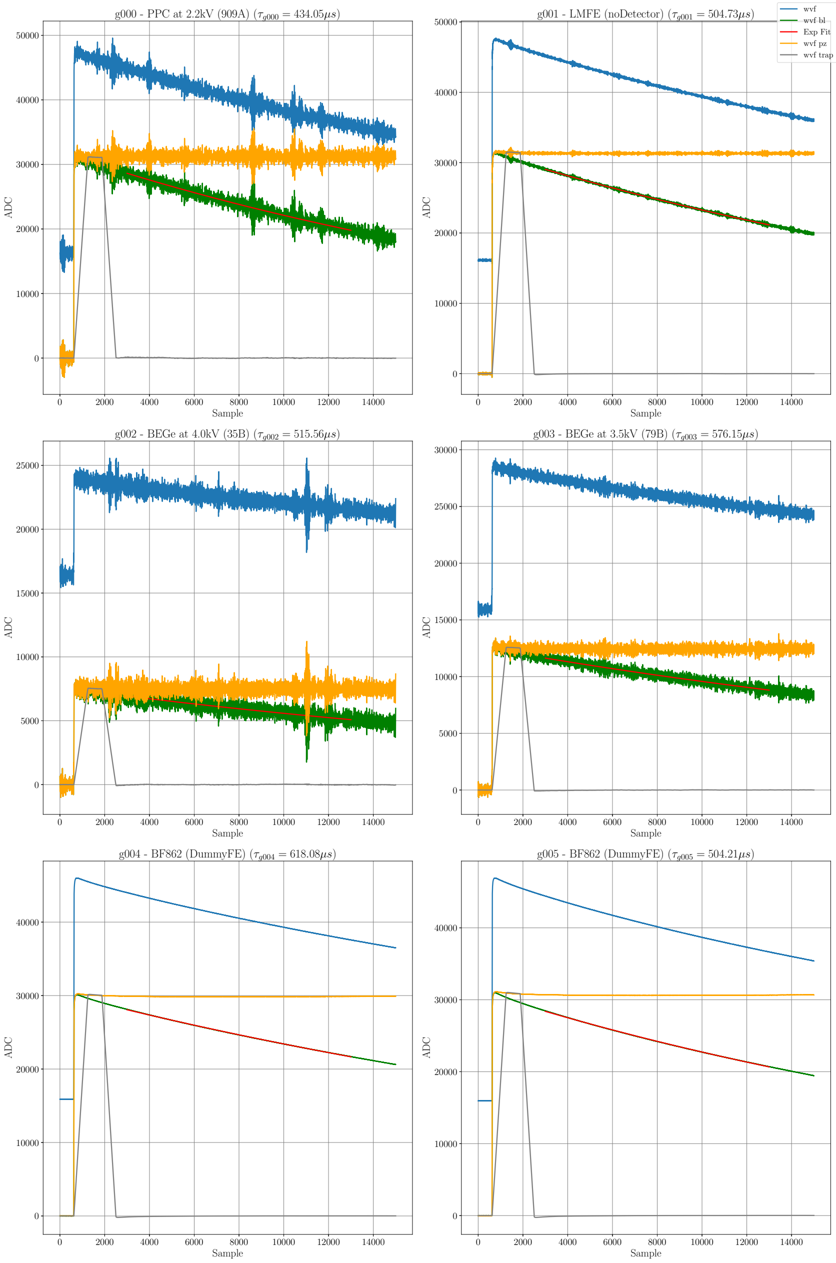

Figure B.3: Waveform example of events in all detectors and dummy front-end (DFE) channels. The blue curve is the unprocessed data, the green one the baseline subtracted where the baseline is calculated by averaging over the first 500 waveform samples. The red fit curve shows an exponential fit in the range from 3000 to 13000, from which the pole-zero corrected waveform (orange) can be calculated by a IIR filter. The energy can then be extracted with a trapezoidal shaper (grey) with a varying rise and flat top time where the energy corresponds to the maximum height of the resulting trapezoidal curve.

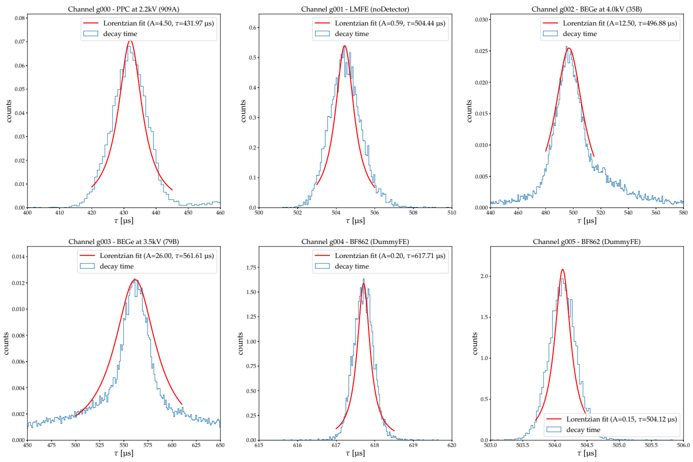

Figure B.4: Decay time distributions for all connected channels in the 4 detector test. The red curve indicate the Lorentzian fir to extract the mean decay time of the distribution.

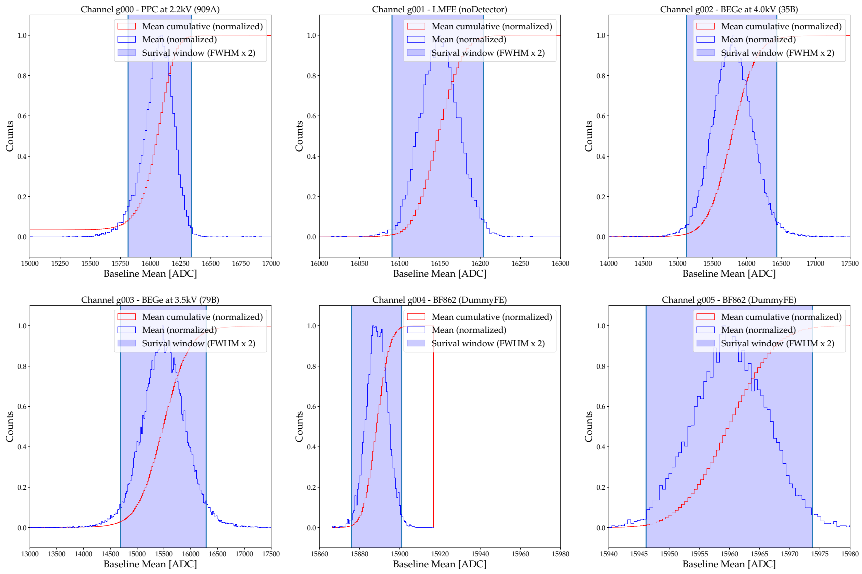

a) Baseline mean

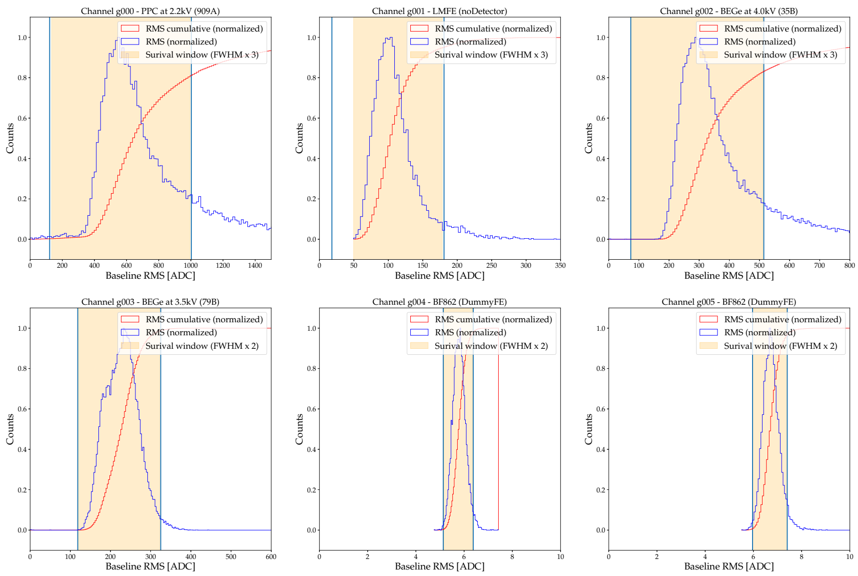

b) Baseline RMS

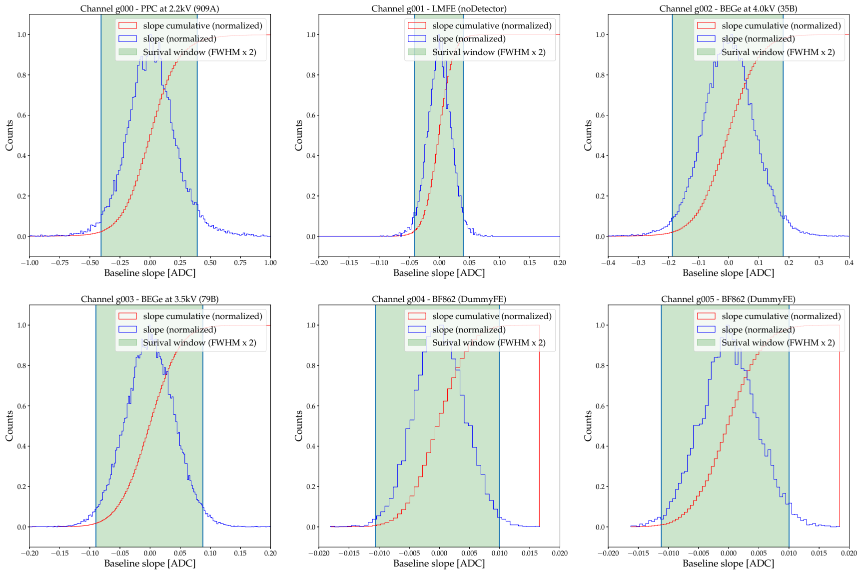

c) Baseline slope

Figure B.5: Baseline mean, RMS and slope distributions of all channels in the 4 detector test. The resulting cut window is shown together with the surrival probability for each cut. The red curves indicated the cumulative values.

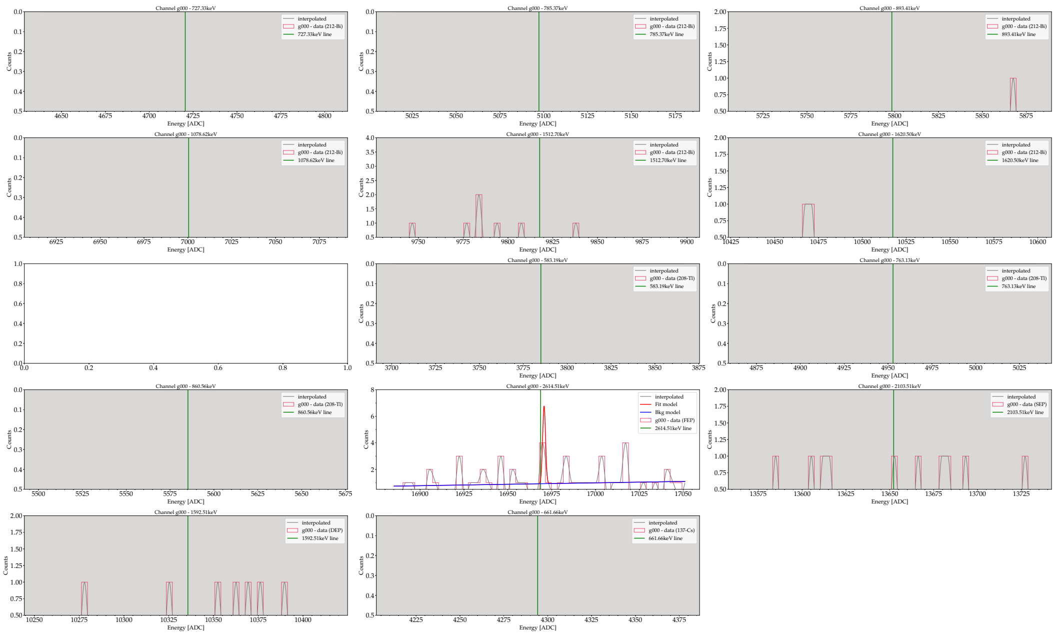

a) Channel 0 - PPC P00909A

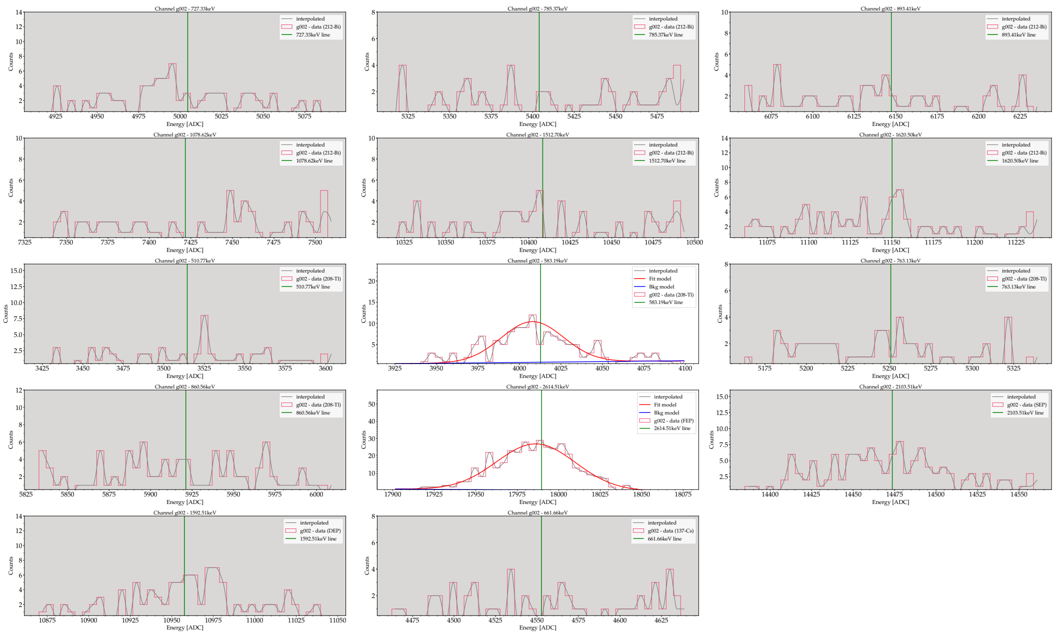

b) Channel 2 - BEGe B00035B

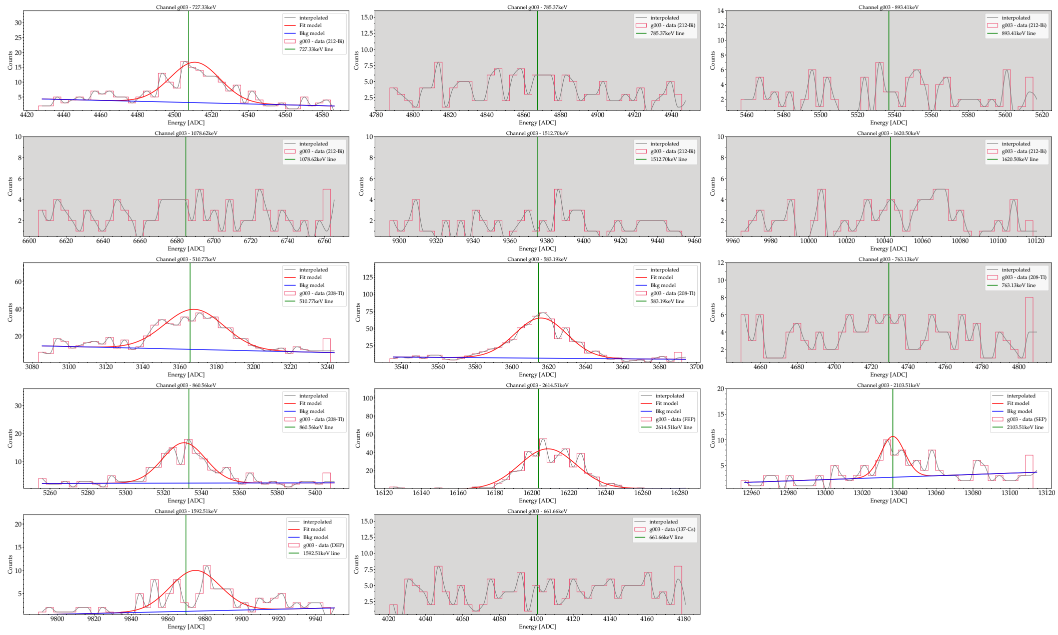

c) Channel 3 - BEGe B00079B

Figure B.6: Calibration windows for all possible peaks of the ^{228}Th calibration run. The peaks and their corresponding windows which are not identified by the peak search are displayed grey while the others are fitted with the calibration function consisting of a Gaussian with a linear background.

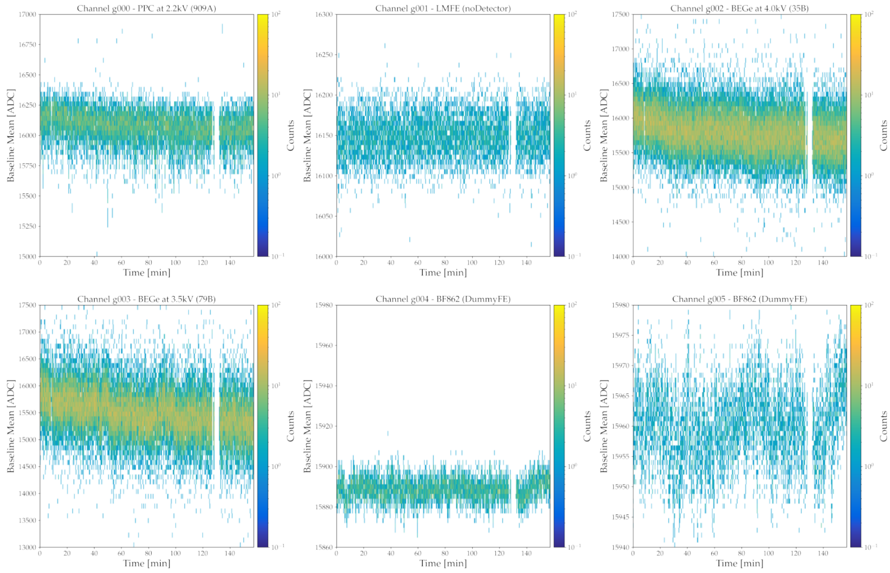

a) Baseline mean vs time

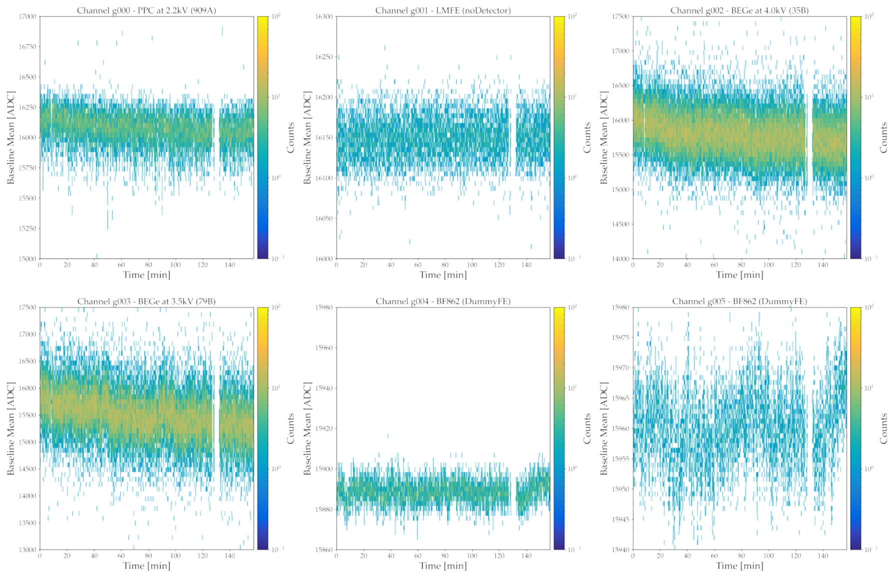

b) Baseline slope vs time

Figure B.7: Scatter plots of the baseline mean and slope versus time for all channels in the 4 detector test. The number of counts is illustrated by the color scale shown at the right side of each subplot.

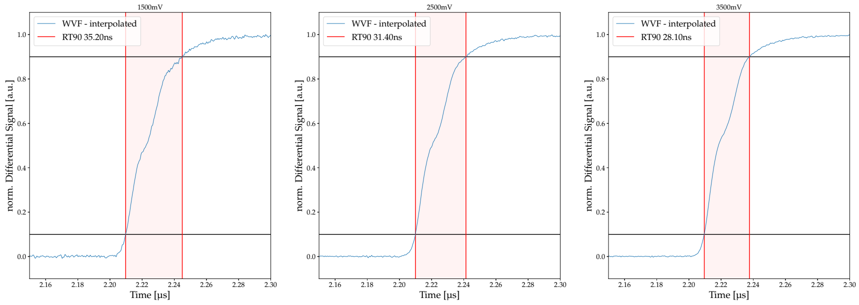

a) Warm

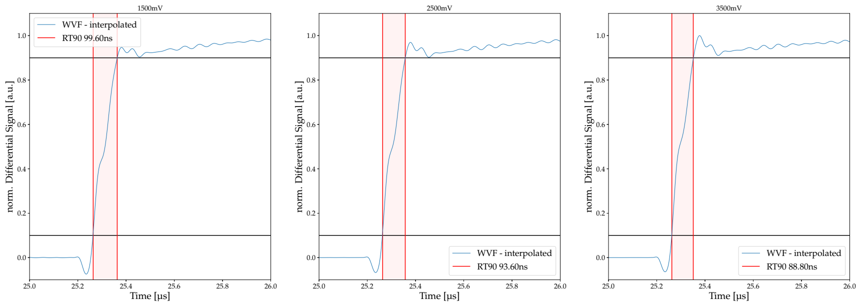

b) Vacuum and cold

Figure B.8: Waveforms example for three waveforms in the setup at room temperature and vacuum and cold. The rise time extraction is shown where the rise time is the time the signals needs to rise from 10% to 90% maximum amplitude which corresponds to the time interval in the red area.

B.3 LBNL ASIC